NASA-CR-193813

Annual Report for NASA Grant: NAG-1-1253 for the period Dec. 1, 1992- Dec. 1, 1993.

Coherent Lidar Design and Performance Verification

Rod Frehlich
Cooperative Institute for Research in the Environmental Sciences (CIRES)
University of Colorado
Boulder, CO 80309 303-492-6776

Results of Current Research

1) The verification of LAWS beam alignment in space can be achieved by a measurement of heterodyne efficiency using the surface return. Due to the statistical nature of the return signal, about 40 shots will be required for a good test. This verification method does not require knowledge of the backscatter coefficient of the surface, the power transmitted, the atmospheric attenuation, or the detector gain. The crucial element is a direct detection signal that can be identified for each surface return. This should be satisfied for LAWS but will not be satisfied for descoped LAWS. These results were presented at the Coherent Laser Radar Meeting in Paris. The behavior of estimates for heterodyne efficiency in the near-field (ground based testing of LAWS) were also determined. For the actual LAWS optical geometry, the required sensitivity is not available. A focused geometry is required to test the space based system.

2) The performance of algorithms for velocity estimation can be described with two basic parameters: the number of coherently detected photo-electrons per estimate and the number of independent signal samples per estimate. For low signal levels, the fraction of bad estimates is required to describe performance. The fraction of bad estimates is mainly a function of the number of effective photo-electrons per estimate and has little dependence on the number of independent samples per estimate; is independent of the estimator used; and has a slight dependence on the velocity space searched.

3) The average error of spectral domain velocity estimation algorithms are bounded by a new periodogram Cramer-Rao Bound. Comparison of the periodogram CRB with the exact CRB indicates a factor of two improvement in velocity accuracy is possible using non-spectral domain estimators. This improvement has been demonstrated with a maximum-likelihood estimator.

4) The comparison of velocity estimation algorithms for 2 and 10 micron coherent lidar was performed by assuming all the system design parameters are fixed (range to target, telescope aperture, detector quantum efficiency, heterodyne efficiency, perfect beam alignment, optical element efficiency, laser pulse energy, atmospheric attenuation, range resolution, observation time per estimate, velocity search space) and the signal statistics are dominated by a 1 m/s rms wind fluctuation over the range gate. Then the quality of the data product is only a function of the wavelength dependence of the backscatter coefficient β. For $\beta \propto \lambda^{-1}$ the number of photons collected per estimate is the same and a 10 micron system has better data quality because the fraction of bad estimates at low signal levels is less than for the 2 micron lidar. For $\beta \propto \lambda^{-2}$ the signal to noise ratio is the same and the 2 micron lidar has better data quality. The two systems have similar data quality when $\beta \propto \lambda^{-1.3}$. These results agree with the GE and TRW reports.

5) The beam alignment requirements for 2 micron are much more severe than for a 10 micron lidar. The effects of the random backscattered field on estimating the alignment error is a major problem for space based lidar operation, especially if the heterodyne efficiency cannot be estimated. This is a sever handicap for 2 micron coherent lidars because the beam alignment must be changed by 5-6 microradians per minute due to variations in orbit height and 6 microradians of misalignment corresponds to more than 20 dB loss in signal power.

6) For LAWS, the biggest science payoff would result from a short transmitted pulse, on the order of 0.5 microseconds instead of 3 microseconds. The advantages are

a) 50-100 meter range resolution in the boundary layer, thus providing data of great interest to atmospheric scientists.

b) More efficient laser design for both CO2 and solid state.

c) QUICK LAWS will only measure the boundary layer. This design is ideal for QUICK LAWS and can be scaled to full LAWS with minimal changes.

d) For conditions of higher backscatter, the 50 m range resolution will permit useful measurements of wind statistics that are essential for optimal design of velocity estimators.

e) A short pulse will permit better velocity estimation algorithms because the statistics of the signal will be determined by the transmitted pulse (which is known) instead of the velocity fluctuations over the sensing volume of the pulse (which are unknown and difficult to estimate).

f) Better measurements near clouds and the surface will be possible.

The disadvantage are:

a) The velocity accuracy in the regions of low backscatter with 1 km height resolution will be about 1.5-2 m/s.

b) A design of a high-energy short pulse CO_2 laser would be difficult to verify with the bread-board laser.

7) The numerically errors for simulation of laser propagation in the atmosphere have been determined as a joint project with the University of California, San Diego. Useful scaling laws were obtained for Kolmogorov atmospheric refractive turbulence and a atmospheric refractive turbulence characterized with an inner scale. This permits verification of the simulation procedure which is essential for the evaluation of the effects of refractive turbulence on coherent Doppler lidar systems.

8) The analysis of 2 micron Doppler lidar data from Coherent Technologies, Inc. (CTI) has demonstrated many of the advantages of doppler lidar measurements of boundary layer winds. The estimation error for a single shot with 50 meter range resolution has been estimated at 0.65 m/s., which is within 40% of the ideal performance of the Cramer-Rao Bound. The effects of wind shear and wind turbulence over the pulse volume are probably the dominant source of the reduced performance.

9) The effects of wind shear and wind turbulence on the statistical description of doppler lidar data has been derived and calculated. This is the first analysis for the single-shot statistics which are required for most Doppler lidar applications. The data is non-stationary and new algorithms are required to take full advantage of real Doppler lidar data. The effects of wind turbulence over the range resolution cell are noticeable for typical LAWS parameters. The effects are more pronounced in the planetary boundary layer. The effects of wind shear and wind turbulence are more pronounced for 2 microns than 10 microns.

Future Work

1) Determine the ability of velocity estimation algorithm's to identify which estimates are good when the signal is low.

2) Include velocity fluctuations and wind shear in velocity estimators for LAWS.

3) Include the estimation of signal parameters like signal power and spectral width in velocity estimators.

4) Characterize the performance of velocity estimators for better OSSIE's.

5) Investigate beam alignment techniques for LAWS including the random nature of the received signals.

6) Collect information about surface return statistics and their effects on beam alignment.

7) Collect information about the wind statistics and their effects on velocity estimation.

Publications and Submitted Papers

"Cramer Rao Bounds for Gaussian random processes and applications to radar processing of atmospheric signals", Rod Frehlich, submitted to IEEE Trans. Geoscience and Remote Sensing.

"Performance of mean-frequency estimators for Doppler radar/lidar", R. G. Frehlich and M. J. Yadlowski, submitted to J. Atmos. Ocean. Tech.

"Heterodyne efficiency as a measure of coherent laser radar performance", Rod Frehlich, submitted to Seventh Conference on Coherent Laser Radar: Applications and Technology Topical Meeting, Paris, July 19-23, 1993.

"Coherent Doppler lidar signal covariance including wind shear and wind turbulence", R. G. Frehlich, submitted to Applied Optics.

"Heterodyne Efficiency for a Coherent Laser Radar with Diffuse or Aerosol Targets", R. G. Frehlich, submitted to Journal of Modern Optics.

"Simulation of Wave Propagation in Three-Dimensional Random Media", Coles, Filice, Frehlich, and Yadlowsky, submitted to Applied Optics

Performance of Mean-Frequency Estimators for Doppler Radar/Lidar

R. G. Frehlich, and M. J. Yadlowsky[1]
Cooperative Institute for Research in the Environmental Sciences (CIRES)
University of Colorado, Boulder, CO 80309

Submitted to J. Atmospheric and Oceanic Technology, May 17, 1993.

Revised September 22, 1993.

Abstract- The performance of mean-frequency estimators for Doppler radar/lidar measurements of winds is presented in terms of two basic parameters: Φ the ratio of the signal energy per estimate to the spectral noise level and Ω which is proportional to the number of independent samples per estimate. For fixed Φ and Ω, the the Cramer-Rao Bound (theoretical best performance) for unbiased estimators of mean-frequency (normalized by the spectral width of the signal), signal power, and spectral width, are essentially independent of the number of data samples M. For large Φ, the estimators of mean-frequency are unbiased and the performance is independent of M. The spectral domain estimators and covariance based estimators are bounded by the approximate periodogram Cramer-Rao Bound. The standard deviation of the Maximum-Likelihood estimator approaches the exact CRB, which can be more than a factor of two better than the performance of the spectral domain estimators or covariance based estimators for typical Ω. For small Φ the estimators are biased due to the effects of the uncorrelated noise (white noise) which results in uniformly distributed "bad" estimates. The fraction of bad estimates is a function of Φ and M with weak dependence on the parameter Ω. Simple empirical models describe the standard deviation of the good estimates and the fraction of bad estimates. For Doppler lidar and for large Φ, better performance is obtained by using many low energy pulses instead of one pulse with the same total energy. For small Φ, the converse is true.

1. Introduction

Measurement of wind fields using Doppler radar have been routinely performed for many years. The design and operation of Doppler radar is reviewed by Doviak and Zrnic (1984, 1993). The optical counterpart to Doppler radar, coherent Doppler lidar, has become more important with the development of efficient CO_2 [Bilbro et al., 1986; Petheram et al., 1989; Post and Cupp, 1990; Pearson and Rye, 1992; Gal-chen et al., 1992] and solid state lidars [Kavaya et al, 1992; Henderson et al., 1992, 1993]. The scatterers for Doppler radar are refractive index fluctuations, hydrometeors, and insects. The scatterers for Dopper lidar are atmospheric aerosol particles. Doppler radar data is generated using a sequence of many pulses, usually separated by 0.5-5 msec. Doppler lidar data is produced with a single pulse which permits many more estimates in a given time. The statistical description of the data is the same (ignoring ground clutter for radar) because both signals are produced by the super-position of many randomly phased scattered fields. Both of these instruments estimate the radial velocity of the scatterers from the Doppler frequency or mean-frequency of the signal by using various estimators.

Most mean-frequency estimators are either spectral domain or covariance estimators, [Levin. 1965; Zrnic, 1979; Mahapatra and Zrnic, 1983; Miller and Rochwarger, 1972; Doviak and Zrnic, 1984, 1993; May and Strauch, 1989; May et al., 1989; Rye and Hardesty, 1993a,b,c; Sirmans, and Bumgarner, 1975], i.e., they estimate the mean-frequency of the weather signal using estimates of the spectrum or estimates of the covariance [see also Kay and Marple, 1981; Marple, 1987].

The ideal performance of an unbiased estimator is given by the Cramer-Rao Bound (CRB) [Helstrom, 1968; Van Trees, 1968; Scharf, 1991; Frehlich, 1993a]. If an unbiased estimator approaches the CRB, it is a Maximum-Likelihood (ML) estimator. Approximate calculations of the CRB have been discussed by Whittle (1953), Levin (1965), Zrnic (1979),Rye and Hardesty, (1993a,b). These approximations are based on the spectrum of the signal, and therefore require a sufficiently long data sequence for

1. Now at BEIP, National Institute of Health, Bethesda, MD, 20892

the spectrum to be well defined [see Marple, (1987) for a discussion of the effects of finite data and discrete sampling]. The calculation of the exact CRB has been discussed by Frehlich (1993a) who introduced an approximate CRB based on the average periodogram instead of the spectrum. We will compare the performance of various mean-frequency estimators to the exact CRB and the periodogram CRB. The CRB and the performance of mean-frequency estimators depend on the parameters of the data. The system parameters are chosen to emphasize the most important physical mechanisms of the problem. This reduces the parameter space to two basic variables: Φ the ratio of the signal energy per estimate to the spectral level of the noise and Ω which is proportional to the number of independent samples per estimate. (For Doppler lidar Φ is also the number of effective photo-electrons coherently detected per estimate). For fixed Φ and Ω, the number of data points M per estimate has little effect on performance, especially for large Φ. This simplifies the design and analysis of Doppler radar/lidar systems.

The performance of mean-frequency estimators has been described by it's standard deviation [Zrnic, 1979; Sirmans, and Bumgarner, 1975; Mahapatra and Zrnic, 1983; Doviak and Zrnic, 1984, 1993; May and Strauch, 1989; May et al., 1989; Rye and Hardesty, 1993a,b] and the number of estimates that fall within a given region [Anderson, 1991; Rye and Hardesty, 1993a]. We describe the performance of mean-frequency estimators using an empirical model for the Probability Density Function (PDF) of the estimates. This will permit a meaningful comparison to the CRB when the estimates are biased due the effects of the uncorrelated noise that produces uniformly distributed "bad" estimates at low signal levels.

For Doppler lidar, Rye and Hardesty, (1993a) considered the question: are many pulses of low energy better than one pulse of the same total energy? This question will be addressed for the unbiased and biased regimes.

2. Basic System Parameters

Doppler radars typically employ a complex receiver (mixers that convert the radio signals to complex data) to measure positive and negative velocities [Doviak and Zrnic, 1984, 1993]. We consider complex data throughout this paper with specific references to the case of real data. Doppler radar or Doppler lidar data is well approximated as a zero-mean complex Gaussian random vector $\mathbf{z}$ with elements z_k which satisfy $<z_k z_l>=0$, where $<.>$ denotes ensemble average [Doviak and Zrnic, 1984, 1993; Helstrom, 1968]. The PDF of the data is Gauusian and defined by the covariance matrix $\underline{\mathbf{R}}$ with elements

$$R_{kl}=<z_k z_l^*> \tag{1}$$

We assume the signal model

$$z_k = s_k \exp(2\pi i k f T_S)+n_k \tag{2}$$

where $f\,[Hz]$ is the mean frequency, $T_S\,[sec]$ is the sampling interval, the random signal s_k is independent of the uncorrelated noise n_k where

$$<n_k n_j>=0, \quad <n_k n_j^*>=N\,\delta_{k-j}\ , \tag{3}$$

$N=<|n|^2>$ is the average noise power, $|n|$ denotes the modulus of the complex variable n, and δ is the Kronecker delta symbol.

For Doppler lidar, the mean frequency f is defined by the radial component of the velocity of the scatterers in the center of the sensing volume of a given range gate [Frehlich, 1993b]. The mean-frequency is well defined for a single shot for any random velocity field and random collection of scatterers. For Doppler radar, the mean-frequency is related to the spectrum of the wind field and sensing volume of the pulse [Doviak and Zrnic, 1984, 1993]. For both Doppler radar and lidar, the signal model of Eq. (2) is valid. An estimate of the mean-frequency is produced with M data samples which defines the total observation time per estimate as $MT_S\,[sec]$.

The average noise power is set to unity to simplify the results. The data is assumed stationary, i.e., $R_{kl}=R_{k-l}$ and the covariance reduces to

$$R_k = SNR\,\rho_k \exp[2\pi i f k T_S]+\delta_k \tag{4}$$

where $SNR=S/N$ is the Signal-to-Noise Ratio, $S=<|s|^2>$ is the average signal power, and ρ_k is the normalized covariance of the signal. The performance of mean frequency estimators will be presented for

the Gaussian covariance model of Zrnic (1979)

$$\rho_k = \exp[-2\pi^2(wkT_S)^2] \tag{5}$$

where $w\,[Hz]$ is the spectral width of the signal. With this model, the data is fully characterized by the system parameters (f, S, w) as well as the experimental parameters M and T_S. For Doppler lidar, this signal model is exact [Frehlich, 1993b] if there are no wind fluctuations over the sensing volume and a Gaussian laser pulse with temporal power profile $P_L(t)[W]$ given by

$$P_L(t)=\exp(-t^2/\sigma^2) \tag{6}$$

is transmitted through a telescope aperture where $\sigma[sec]$ is

$$\sigma=1/(\sqrt{8}\pi w)\,. \tag{7}$$

The Full-Width at Half-Maximum (FWHM) $\Delta t\,[sec]$ of the transmitter pulse is

$$\Delta t=2\sqrt{\ln 2}\sigma\,. \tag{8}$$

The 1/e Full Width of the signal covariance $\Delta\tau[sec]$, which defines the signal correlation time (see Fig. 1), is

$$\Delta\tau=\frac{\sqrt{2}}{\pi w}=4\sigma\,. \tag{9}$$

For a Doppler Lidar operating under ideal conditions (the detector noise is dominated by the local oscillator shot noise, the shot noise is determined by the Poisson statistics of the detected photons, and there is no atmospheric refractive turbulence, Frehlich and Kavaya, 1991) the SNR is given by

$$SNR(t)=\frac{P_D(t)}{h\nu B}\eta_H(t) \tag{10}$$

where $P_D(t)$ is the effective direct detection power measured by the detector, $\eta_H(t)$ is the heterodyne efficiency, $h=6.626\times 10^{-34}[Js]$ is Planck's constant, $\nu[Hz]$ is the optical frequency, and $B\,[Hz]$ is the detector bandwidth. For ideal operation

$$SNR(t)=\frac{\eta_Q}{h\nu B}\int_0^\infty P_L(t-2R/c)[K(R)]^2\beta(R)C(R)dR \tag{11}$$

where $\eta_Q\,[electrons/photon]$ is the detector quantum efficiency, $c\,[m\ s^{-1}]$ is the speed of light in a homogeneous atmosphere, $K(R)$ is the dimensionless one-way irradiance extinction of the atmosphere at range $R\,[m]$, $\beta(R)[m^{-1}sr^{-1}]$ is the atmospheric aerosol backscatter coefficient, $P_L(t)$ is the pulse power profile of the laser, and $C(R)$ is the coherent responsivity of the Doppler lidar (lidar system dependence). The term $P_L(t-2R/c)[K(R)]^2\beta(R)C(R)$ describes the range weighting for the SNR. For many cases of interest, the terms $[K(R)]^2\beta(R)C(R)$ are constant over the range gate and the range weighting function is given by the term $P_L(t-2R/c)$ The FWHM $\Delta r\,[m]$ of the range weighting function for the Gaussian pulse is then

$$\Delta r=c\,\Delta t/2 \tag{12}$$

A simulation of Doppler Lidar data (Appendix A) and the range weighting function $P_L(t-2R/c)$ is shown in Fig. 1 for typical parameters of a 2 micron lidar. At time 2μsec the center of the pulse is located at range $300m$ with a width Δr. At a time 4 μs later the pulse is situated at a range of 900 m. The range resolution $\Delta R\,[m]$ for an observation time MT_S is defined as

$$\Delta R=\Delta r+\Delta p \tag{13}$$

where $\Delta p\,[m]$ is the distance the range weighting function travels during the observation time, i.e.,

$$\Delta p=MT_S c/2\,. \tag{14}$$

The temporal scale of the modulation of the signal corresponds to the time required for the pulse to travel a distance Δr, after which time a new collection of independent atmospheric scatterers are illuminated by the pulse (see Fig. 1).

The periodogram of the data is defined as [Doviak and Zrnic, 1984, 1993; Marple, 1987]

$$\hat{P}(m)=\frac{T_S}{M}\left|\sum_{k=0}^{M-1} z_k \exp(-2\pi ikm/M)\right|^2 \tag{15}$$

and is shown in Fig. 1. This is an estimate for the spectrum at frequencies $f=m\Delta f$ where $\Delta f=1/(MT_S)$ is the frequency resolution. The maximum frequency that can be observed without aliasing is the Nyquist frequency $F_N=M\Delta f=1/T_S$ [for real data $F_N=1/(2T_S)$]. The frequency domain estimation of the mean frequency f involves extracting the location of the spectral feature of the random periodogram coefficients (or any spectral domain estimate) in the presence of random noise. It is reasonable to expect that the performance of a frequency domain estimator depends on the statistics of the signal and noise around the spectral feature. If one would increase the sampling interval T_S by a factor of two and also reduce the noise bandwidth by a factor of two to match the new Nyquist frequency, the performance of the spectral domain mean frequency estimator would be unchanged because the statistics of the periodogram around the spectral feature is unchanged. However, the frequency range that can be searched has been reduced by a factor of two and the SNR has increased by a factor of two. Therefore, the SNR is not a convenient parameter to characterize the signal strength.

A more useful parameter to describe the signal power for mean frequency estimation is the ratio of the total signal energy per estimate $E=SMT_S$ to the spectral noise level $N_0=NT_S$, i.e.,

$$\Phi=E/N_0=SNR\ M \tag{16}$$

(Note that for real data, $N_0=2NT_S$ and $\Phi=SNR\ M/2$). This is the basic parameter used in communication and radar for matched filter estimation of known signals in uncorrelated noise [Helstrom, 1968; Van Trees, 1968]. For Doppler lidar with quantum limited detection (the additive noise is dominated by the local oscillator shot noise), this parameter has a convenient physical interpretation. It is common practice to set the sampling rate $1/T_S$ equal to the noise bandwidth B. The SNR Eq. (10) can then be written as

$$SNR(t)=P_R(t)\eta_H(t)T_S \tag{17}$$

where $P_R(t)=P_D(t)/(h\nu)[photo-electrons/sec]$ is the detection rate of photo-electrons. Therefore

$$\Phi=\eta_H P_R\ M\ T_S. \tag{18}$$

Since $P_R\ M\ T_S$ is the number of photo-electrons generated per observation time MT_S, Φ is the effective number of photo-electrons coherently detected per observation time. For Doppler radar, this interpretation is not valid because quantum limited detection is not achieved. However, the interpretation of Eq. (16) is meaningful for Doppler radar.

The spectral width w is commonly normalized by the Nyquist frequency $F_N=1/T_S$. For fixed range resolution (fixed MT_S), this parameter changes with the sampling interval. A more convenient parameter is the ratio of the spectral width w to the frequency resolution Δf,

$$\Omega=w/\Delta f=wMT_S \tag{19}$$

This parameter can be written as

$$\Omega=\frac{\sqrt{2}}{\pi}M_I=\frac{[\ln(2)/2]^{1/2}}{\pi}\frac{\Delta p}{\Delta r} \tag{20}$$

where

$$M_I=\frac{MT_S}{\Delta\tau} \tag{21}$$

is defined as the number of independent samples of the signal in the observation time MT_S. The parameter Ω is also proportional to $\Delta p/\Delta r$, the number of pulse widths Δr contained in the distance Δp that the pulse travels during the observation time, if there are no velocity fluctuations over the sensing volume of the pulse that would increase the spectral width w. Using the parameters of Figure 1 we have $M_I=4.44$, which is approximately the number of modulated events displayed in the lidar signal. For Doppler Lidar observations of uniform wind fields using a Gaussian pulse, the choice of one independent sample per observation interval ($M_I=1$) produces $\Omega=0.450$ and $\Delta p/\Delta r=2$. Zrnic (1979) investigated the number of

independent samples per estimate in terms of the reduction of the variance of the estimates for signal power. Zrnic's effective number of independent samples is also proportional to Ω. The definition of Eq. (21) is chosen as a visual description of the data and as a simple connection to the covariance function. Since the choice of a definition for the number of independent samples per estimate is arbitrary, the parameter Ω will be used to represent this basic physical quantity.

The covariance of the data [Eqs. (4), (5)] can be written in terms of the new variables Φ and Ω, i.e.,

$$R_k = \frac{\Phi}{M}\exp[-2\pi^2\Omega^2k^2/M^2+2\pi i\frac{f}{w}\Omega k]+\delta_k \ . \tag{22}$$

The best performance of any unbiased estimator of the signal parameters is given by the Cramer-Rao Bound (CRB). For fixed Φ and Ω, the CRB σ_f (Frehlich, 1993a) for estimation of the mean frequency normalized by the spectral width w as a function of M are shown in Fig. 2. [The normalized variable σ_f/w is suggested by the functional form of Eq. (22)]. For sufficiently large M, the CRB for the normalized mean frequency is independent of M for all the parameters Ω. For larger Ω, the CRB becomes independent of M when the extent of the signal spectrum is less than the Nyquist frequency, i.e., when $wT_S<1/6$ or $M>6\Omega$. This condition is satisfied for any realistic problem. Since σ_f/w is independent of M, the CRB for mean frequency σ_f is independent of M for fixed w. This implies that the total observation time per estimate MT_S and range resolution is also fixed because $\Omega=wMT_S$ is fixed. The CRB for mean frequency σ_f is independent of M for fixed observation time MT_S (fixed range resolution) and fixed w. This result was also obtained by Rye and Hardesty, (1993a) using approximate empirical models for Levin's approximate CRB. The exact CRB verifies the accuracy of this statement. The CRB for estimation of the average signal power S and the CRB for the estimation of the spectral width w are also shown in Fig. 2. For both cases, the CRB is independent of M, provided that the spectral width is less than the Nyquist frequency. Similar results are produced for other values of Φ. This result is excellent motivation for the choice of Φ and Ω as the basic system parameters. Accurate calculations of the CRB's of the signal parameters for very large M can be made using the more efficient calculation at smaller M. For fixed MT_S (fixed range resolution), the frequency resolution Δf for the periodogram is also fixed. For fixed Φ, Ω, and MT_S, the satistics of the periodogram around the spectral peak will be unchanged because the shape of the signal peak compared to the frequency resolution Δf is unchanged. This provides an intuitive explanation for the invariance of the CRB's for the estimation of the normalized signal parameters. The low SNR analytic approximation to the CRB for mean frequency can be written as $\sigma_f^2/w^2 = 4\sqrt{\pi}\Omega/\Phi^2$ [Zrnic, 1979, Eq. (A29)], which is independent of M. However, the high SNR analytic approximation to the CRB becomes $\sigma_f^2/w^2 = 12\Omega^2/M^3$ [Zrnic, 1979, Eq. (A28)], which is not independent of M. It has been shown that the high SNR approximation to the CRB is not valid [Frehlich, 1993a].

The radial component $v[m/s]$ of the velocity of the atmospheric scatterers is related to the mean-frequency f by $v=\lambda f/2$ and the velocity estimation error $\sigma_v[m/s]=\lambda\sigma_f/2$, where $\lambda[m]$ is the operating wavelength. The velocity error is proportional to λ if σ_f is independent of λ, i.e., if Φ and Ω are independent of λ and MT_S (range resolution) is fixed. For Doppler Lidar Φ is independent of λ for fixed laser power P_L if the backscatter coefficient $\beta\propto\lambda^{-1}\propto v$ [Eqs. (11), (16)]. Ω is independent of λ if w is independent of λ, i.e., there are negligible velocity fluctuations over the sensing volume of the pulse and w is determined by the transmitted pulse shape [Frehlich, 1993b]. Velocity error is then proportional to wavelength for fixed MT_S (fixed range resolution), fixed w, fixed power transmitted, and $\beta\propto\lambda^{-1}$. This is a convenient benchmark for system design and for some atmospheric conditions $\beta\propto\lambda^{-1}$ [Srivastava et al. 1992]. Rye and Hardesty (1993a) found that Levin's approximate CRB for mean frequency estimation is proportional to $\lambda^{1/2}$ for fixed range resolution, fixed signal power, fixed maximum velocity, and fixed wT_S (the spectral width is determined by the velocity fluctuations over the sensing volume of the pulse).

3. Mean Frequency Estimators

For Doppler lidar with short pulses, the spectral width of the signal w will be determined by the pulse and therefore known a priori [Frehlich, 1993b]. If a long pulse is transmitted, the effects of wind shear and wind turbulence produce non-stationary data [Frehlich, 1993b]. For non-stationary data, spectral domain and covariance based estimators are not rigorously defined and the Maximum Likelihood estimators will produce the best performance. For a typical experiment, many pulses will be transmitted

and the SNR will also be known if the atmosphere is stationary over the total observation time. The mean-frequency estimators considered here will assume knowledge of the SNR and the spectral width w. For typical Doppler radar operation, the spectral width is determined by the wind fluctuations in the sensing volume, and must also be estimated. The pulse-pair algorithm does not require a priori knowledge. All the other algorithms discussed in this section require knowledge of the SNR and spectral width w.

Pulse-Pair (PP)

A numerically efficient algorithm for mean frequency estimation is the Pulse-Pair (PP) estimator given by [Miller and Rochwarger, 1972; Zmic, 1979]

$$\hat{f} = \frac{1}{2\pi T_S} arg[\hat{R}_1] \tag{23}$$

where

$$\hat{R}_k = \frac{1}{M-k} \sum_{i=0}^{M-1-k} z_{i+k} z_i^* \tag{24}$$

is an unbiased estimate for R_k, the covariance at lag kT_S with a fixed length of data.

Maximum Likelihood Estimator (ML)

The Maximum Likelihood (ML) estimator is the value of the unknown parameters that maximizes the log-likelihood function [Helstrom, 1968, Van Trees, 1968], given by

$$L(f,S,w) = = -\mathbf{z}^{*T} \underline{\mathbf{R}}^{-1}(f,S,w)\,\mathbf{z} - \ln[|\underline{\mathbf{R}}(f,S,w)|] - M\ln(\pi) \tag{25}$$

where $|\underline{\mathbf{R}}|$ denotes the determinant of the matrix $\underline{\mathbf{R}}$. For the signal model considered here $|\underline{\mathbf{R}}(f,S,w)|$ is independent of f. The simplest ML estimator for mean frequency f assumes knowledge of the signal power S and the spectral width w. For the covariance model of Eq. (4) [Zmic, 1979],

$$R_{kl}^{-1}(f,S,w) = D_{kl}(S,w)\exp[2\pi i f T_S(k-l)] \tag{26}$$

where $\underline{\mathbf{D}}(S,w) = \underline{\mathbf{R}}^{-1}(f=0,S,w)$. In this case, the ML estimator for f is the value $\hat{f}$ that maximizes

$$L_1 = \sum_{m=0}^{M-1} d_m \cos(2\pi T_S m \hat{f}) \tag{27}$$

where

$$d_m = \sum_{k=0}^{M-m-1} z_k^* z_{k+n} D_{k,k+n}(S,w) \tag{28}$$

The ML estimator can be efficiently calculated using the Fast Fourier Transform (FFT) algorithm of length $M_S >= M$ at discrete frequencies $f = k_f T_S / M_S$. Note that the ML estimator is not given in terms of an estimate for the covariance.

Periodogram Maximum Likelihood Estimator (PML)

In the limit of large M, the DFT and periodogram coefficients $\hat{P}(m)$ become mutually uncorrelated and the Maximum Likelihood estimator for the mean frequency is the value of f that maximizes the log-likelihood function

$$L(f,S,w) = -\sum_{m=0}^{M-1} \frac{\hat{P}(m)}{P(m,f,S,w)} \tag{29}$$

where [Doviak and Zmic, 1984, 1993, Chap. 5]

$$P(m) = <\hat{P}(m)> = T_S \sum_{l=-(M-1)}^{M-1} R_l \exp(-2\pi i T_S m l / M)\,. \tag{30}$$

[Levin (1965) and Rye and Hardesty (1993a,b) used this algorithm with the spectrum substituted for $P(m,f,S,w)$. For small Ω and large Φ, this approximation results in poorer performance, e.g., for Ω=0.5

and $\Phi>100$ the velocity error is 15% larger than the PML estimator]. The PML estimator is numerically more efficient when computed in the time domain. If the DFT coefficients are mutually uncorrelated and statistically independent, then the inverse of the covariance matrix $\underline{\mathbf{R}}$ is Toeplitz and has the form of Eq. (26) where

$$D_{kl}(S,w)=\frac{1}{M}\sum_{m=0}^{M-1}\frac{\exp[2\pi im(k-l)/M]}{P(m\,f=0,S,w)} \tag{31}$$

Substituting this result in Eq. (28) produces the periodogram ML estimator (PML), which is also equivalent to implementing Eq. (29) using the DFT algorithm. This estimator can be written in terms of estimates for the covariance $\hat{R}_k$ because the matrix $\underline{\mathbf{R}}^{-1}$ is Toeplitz [See Eq. (28)].

Time Series Model Estimators (MVYW)

Many spectral domain estimators have been proposed using models for the time series. These algorithms are discussed by Marple (1987) and computer programs provided. The regressive spectral estimator is given by

$$P_{AR}(p\,f)=\frac{T_S\rho_w}{|1+\sum_{k=1}^{p}a_k\exp(-2\pi ifkT_S)|^2} \tag{32}$$

where the coefficients a_k and ρ_w are determined from the estimates of the covariance of the data. The order p is an input parameter that must be selected.

Another time series algorithm introduced by Capon (1969) has been advocated by Anderson (1991) for Doppler lidar parameter estimation. Marple (1987) calls this algorithm a Minimum Variance (MV) estimator which can be written as

$$\frac{1}{P_{MV}(p\,f)}=\sum_{k=1}^{p}\frac{1}{P_{AR}(k\,f)} \tag{33}$$

For the spectral domain estimators, the mean-frequency $\hat{f}$ is determined by the maximum value of the spectral estimator. We have investigated the performance of the AR spectral estimator and the MV spectral estimator using the Yule-Walker and Burg method for estimating the regressive coefficients and using the order p that produced the best performance [smallest standard deviation of the good estimates (see Section 4)] for fixed (Φ,Ω,M). For large Φ, the best order for the AR and MV estimators was $p=1$, which corresponds to the PP estimator [Rye and Hardesty, 1993b]. The MV estimator with the Yule-Walker method (MVYW) produced the best overall performance.

4. Performance of Mean Frequency Estimators

The most useful description of the performance of an estimator is it's Probability Density Function (PDF). For fixed T_S and in the limit of large M, if the ML estimator is unbiased, it approaches the ideal performance of the CRB and t's PDF approaches a Gaussian distribution. The periodogram (or any spectral estimator) of the random signal is random. For small Φ or SNR, there will be realizations where the spectral feature of the signal is buried in the noise. Then, the spectral domain estimators for mean frequency will choose the largest noise feature that mimics the signal. This behavior was first recognized and analyzed by Shirakawa and Zrnic, (1983) and Hardesty, (1986). This qualitative description of a clump of localized good estimates around the true mean frequency sitting on a pedestal of uniformly distributed "bad" estimates has been observed in many other cases [Mahapatra and Zrnic, 1983; May and Strauch, 1989; Anderson, 1991; Rye and Hardesty, 1993a]. The PDF of the mean frequency estimators $\hat{f}$ is therefore modeled as a Gaussian PDF centered on the true mean frequency f and a uniformly distributed component of bad estimates over the frequency range $(0,F_N=1/T_S)$, which is written as

$$PDF(\hat{f})=bT_S+\frac{(1-b)T_S}{\sqrt{2\pi}g}\exp[-(\hat{f}-f)^2/(2g^2)] \tag{34}$$

where b is the fraction of bad estimates and g is the standard deviation of the good estimates (see also Rye and Hardesty, 1993c). The PDF of the mean-frequency estimators is estimated by it's histogram with

bin size Δf. The parameters of the model PDF (b,g) are determined by minimizing the mean-square-difference between the histogram and the predicted histogram based on the model PDF. An example of the histograms for 10000 estimates of the ML estimator and the PP estimator, the predicted histogram of the best fit model parameters, and the model PDF are shown in Fig. 3. The ML estimator produces good agreement with the model PDF. The PP estimator is a poorer fit to the model PDF when $\Phi<100$. This is due to the nonlinear interaction of the signal and noise.

The comparison of estimator performance with the CRB is complicated by the presence of the uniform distribution of bad estimates. If the model PDF is a good approximation then it provides a complete statistical description of an estimator. For example, the ensemble average of the mean frequency estimator $\hat{f}$ is

$$<\hat{f}> = \int_0^{1/T_s} \hat{f} PDF(\hat{f}) d\hat{f} = \frac{b}{2T_S} + (1-b)f \tag{35}$$

which indicates a bias from the true mean-frequency f. The mean-square-error of the estimator is defined as

$$<(\hat{f}-f)^2> = \sigma_e^2 = \int_0^{1/T_s} (\hat{f}-f)^2 PDF(\hat{f}) d\hat{f} = \frac{b}{3T_S^2}(1-3fT_S+3f^2T_S^2) + (1-b)g^2 \tag{36}$$

which has a minimum for $fT_S=0.5$. The CRB for a biased estimator is given by [Helstrom, 1968]

$$<(\hat{f}-f)^2> \geq \sigma_B^2 = (\frac{\partial <\hat{f}>}{\partial f})^2 \sigma_f^2 = (1-b)^2 \sigma_f^2 \tag{37}$$

where σ_f^2 is the CRB for an unbiased estimate of f. The CRB for a biased estimate depends on the fraction of bad estimates b which in turn depends on the estimator $\hat{f}$. A comparison of different estimators that includes the bias can be related to the CRB for unbiased estimates by dividing Eqs. (36) and (37) by $(1-b)^2$. From the modified Eq. (36), the adjusted standard deviation of the estimator error becomes

$$\sigma_C = \sigma_e/(1-b) \tag{38}$$

which is to be compared with the CRB σ_f for unbiased estimators.

An empirical model for the fraction of bad estimates b as a function of Φ for fixed Ω and M is

$$b(\Phi) = [1+(\Phi/b_0)^{\alpha}]^{-\gamma}. \tag{39}$$

In the previous section, it was shown that the CRB for estimation of the mean frequency f normalized by the spectral width w was independent of the number of observation points M for fixed Φ and Ω. This suggests the use of the parameter $g_N=g/w$. An empirical functional form for this parameter is

$$g_N(\Phi) = \chi[1+(\Phi/g_0)^{\varepsilon}]^{-\delta}+\mu \tag{40}$$

The simulation results shown in the following Figures were generated by averaging 10 simulations of 2000 realizations each for large Φ. As the number of good estimates declined at small Φ, the number of realizations were increased to maintain the number of good estimates at approximately 2000. The standard deviation of the 10 estimates for b and $g_N=g/w$ were used to obtain the chi-squared best fit [Press et al., 1986] for the parameters of the empirical models Eqs. (39) and (40).

The performance of the Maximum Likelihood estimator is shown in Fig. 4 for $\Omega=0.5$. The simulation results agree well with the best fit models Eqs. (39) and (40). For large Φ, the bias of the estimator is small and the standard deviation of the good estimates g approaches the CRB. For small Φ, the comparison of the standard deviation σ_C of the biased estimate to the CRB that includes the effect of the bias is poor. This is a typical result for all the estimators we investigated. The CRB with the bias included [Eq. (37)] is a poor indicator of estimator performance. The standard deviation of the good estimates g and the fraction of the bad estimates b provide a complete description of the performance of mean-frequency estimators when the model PDF defined by Eq. (34) is valid. For small Φ, the standard deviation of the good estimates g is less than the CRB. This does not contradict the meaning of the CRB because in this regime the estimates are biased and are not bounded by the CRB for unbiased estimates.

The performance of the periodogram maximum likelihood (PML) estimator is shown in Fig. 5 for Ω=0.5. The simulation results agree well with the best fit models Eqs. (39) and (40). When the estimates are unbiased (Φ>~100), the performance is bounded by the periodogram CRB.

The performance of all the mean-frequency estimators considered here are shown in Fig. 6 for Ω=0.5 (typical Doppler lidar case) and in Fig. 7 for Ω=2.0 (typical Doppler radar case). The parameters of the empirical models Eqs (39) and (40) are given in Table 1. All the spectral domain and covariance based estimators are bounded by the periodogram CRB for Φ>~100 (unbiased estimates). For the best estimators (ML,PML,AR,MV), the standard deviation of the good estimates g approaches w for small Φ and approaches a fraction of w ($\approx$1/10) for large Φ. This general feature produces a useful description of mean-frequency accuracy in terms of the basic parameters Φ and Ω. The dependence of b with Φ is similar for the best estimators. The PDF of the PP estimator is a poor fit to the empirical model Eq. (34) for Φ<~100 (see Fig. 3) and results in deviation from the other estimators. For Ω=0.5 and large Φ, more than a factor of two improvement in mean-frequency accuracy is realized with the Maximum-Likelihood estimator compared with the best spectral-domain and covariance based estimators.

The performance of the Maximum Likelihood estimator for M=32,64,128 is shown in Fig. 8 for Ω=0.5 and in Fig. 9 for Ω=2. The standard deviation of the good estimates has little dependence on the total number of data points M for Φ>10, i.e., the mean-frequency error is independent of the maximum observable frequency F_N for fixed range resolution and fixed signal energy per estimate. For fixed Φ, and increasing M, the fraction of bad estimates b increases because there are more noise spikes that may be larger than the true mean-frequency signal peak of the log-likelihood function.

5. Tradeoff Between Pulse Energy and Number of Pulses

Rye and Hardesty (1993b) posed an important question: is it better to use many pulses with low energy or one pulse with the same total energy? For constant laser power and for the case where accumulated data from many pulses approaches Levin's CRB, they showed that many low energy pulses were better than one high energy pulse for narrow spectral width. This regime corresponds to large Φ where there are no bad estimates. The performance of mean-frequency estimators for K pulses per estimate can be compared to the single pulse case for fixed Φ. The data for each pulse is assumed statistically independent. This is a good assumption for Doppler Lidar because the signal correlation time is of the order of 1μs and the interval between pulses is larger than $10msec$.

The Likelihood Function L_K for K statistically independent data vectors $\mathbf{z}_n$ and fixed range resolution (fixed MT_S) is [Scharf, 1991]

$$L_K(f, S_K, w) = -K\ln[|\underline{\mathbf{R}}(f, S_K, w)|] - KM\ln(\pi) - \sum_{n=1}^{K} \mathbf{z}_n^{*T}\, \underline{\mathbf{R}}^{-1}(f, S_K, w)\, \mathbf{z}_n \tag{41}$$

where $\mathbf{z}^T$ denotes the transpose of $\mathbf{z}$ and S_K=S/K is the signal power for each pulse. The CRB for this data set of K pulses is

$$\sigma_{fK}^2 = \sigma_f{}^2(S_K)/K \tag{42}$$

where $\sigma_f{}^2(S_K)$ is the CRB for one pulse with signal power S_K. The CRB for the mean-frequency as a function of the total number of pulses but with fixed total energy Φ is shown in Fig. 10. Multiple pulses are better for Φ>~10 and smaller Ω. The performance of the ML estimator [the value of f that maximizes Eq. (41)] for different K as a function of Φ is shown in Fig. 11 for Ω=0.5 and in Fig. 12 for Ω=2. For small Φ, the best performance is obtained by using one pulse. For large Φ, performance is improved by dividing the total laser energy among many pulses. The effects are most pronounced for small Ω. For small Φ, concentrating all the energy into one pulse produces the optimal signal for identifying the good estimates. For large Φ, there is no difficult identifying the good estimates and more pulses result in a decrease in the mean-frequency error because each pulse produces a statistically independent estimate and the error scales as $K^{-1/2}\sigma_f(S_K)$. Since $\sigma_f(S_K)$ changes slowly compared to $K^{-1/2}$, performance improves with more pulses. The CRB (see Fig. 10) provides an effective prediction of the behavior of the standard deviation of the good estimates g for all Φ.

6. Summary

For the signal model of Eqs. (2), (4), and (5), the performance of mean-frequency estimators is conveniently presented in terms of two basic parameters: Φ the ratio of the signal energy per estimate to the spectral noise level and Ω which is proportional to the number of independent samples per estimate. For Doppler lidar, Φ is the number of coherently detected photo-electrons per estimate. For fixed Φ and Ω, the CRB's for unbiased estimates of the signal parameters are independent of the number of samples per estimate M (Fig. 2). The PDF of a mean-frequency estimator is the best description of performance. For the better estimators, the PDF can be accurately modeled as a Gaussian distribution function around the true mean frequency and a uniformly distributed component of bad estimates (Fig. 3). This model requires two parameters: the standard deviation of the good estimates g and the fraction of the estimates b that are bad. The empirical functions Eqs. (39) and (40) provide a good approximation for g and b as a function of Φ for fixed Ω and M. The parameters of these empirical models are listed in Table 1 for some common mean-frequency estimators. The fraction of bad estimates can be reduced by neglecting the estimates that have low signal power (Rye and Hardesty, 1993c). Adaptive mean-frequency estimators have also been proposed to reduce the detrimental effects of the fades in signal power [Dabas et al., 1993].

For large Φ: the estimates are unbiased, the standard deviation of the spectral domain and covariance based estimates are bounded by the periodogram CRB (Figs. 6,7), and the standard deviation of the ML estimator approaches the exact CRB (Fig. 4). For smaller Ω, the ML estimator has more than a factor of two improvement in performance compared to previous estimators (Fig. 7). For $\Phi<\sim100$, all the estimators are biased due to the uniformly distributed bad estimates. For fixed M, the behavior of the fraction of bad estimates b is almost a universal function of Φ with a weak dependence on Ω (Figs. 6-9), i.e., the better estimators (ML,PML,AR,MV) perform equally well in identifying the cases where the random signal is not buried in the random noise. For fixed Φ and Ω, as M increases (Figs. 8,9), the fraction of bad estimates increases because the random spectral feature of the signal must be identified among more noise spikes. For $\Phi>100$ and fixed Ω, the standard deviation of the good estimates normalized by w is essentially independent of M and for fixed range resolution and fixed signal energy, the standard deviation of the mean frequency estimators are independent of the maximum observable frequency F_N. For fixed range resolution, fixed spectral width, fixed transmitted pulse energy, and a backscatter coefficient $\beta \propto \lambda^{-1}$, the velocity error is proportional to the operating wavelength λ. The spectral width of the signal is constant with operating wavelength when the wind fluctuations are negligible over the sensing volume of the pulse. This is true for Doppler lidar with short pulse lengths and typical atmospheric conditions. For typical Doppler radar conditions, the spectral width of the signal is determined by the wind fluctuations over the sensing volume of the pulse. Then, the velocity error is approximately proportional to $\lambda^{1/2}$ for fixed range resolution and fixed signal energy (Rye and Hardesty, 1993a).

For Doppler lidar and for large Φ, it is better to transmit many low energy pulses instead of one pulse with the same total energy, if the parameters of the process do not change during the measurement interval. For small Φ, the converse is true (Figs. 11,12).

The behavior of the performance of mean-frequency estimators as a function of the two basic parameters Φ and Ω simplify Doppler Lidar design. In many cases, the range resolution of the measurement is determined by the application. Assuming one independent velocity measurement per observation time and small fluctuations of the wind field over the sensing volume of the pulse (w is determined by the transmitted pulse profile and Ω=0.45) fixes the pulse length and observation time per estimate MT_S. The maximum search velocity $v_{max}=\lambda/(2T_S)$ determines T_S and M. The velocity accuracy $\sigma_v=\lambda\sigma_f/2$ and the fraction of bad estimates b is then a function of one parameter Φ. To produce estimates with a small number of bad estimates, $\Phi>100$, which determines the required pulse energy for a specified backscatter coefficient.

Acknowledgement. The authors acknowledges useful discussions with M. J. Kavaya, D. S. Zrnic, and B. J. Rye. This work was supported by the National Science Foundation and the National Aeronautics and Space Administration.

APPENDIX A: Simulation of Doppler Radar/Lidar Data

Complex Doppler radar/lidar data with a specified covariance can be generated with a simple computer algorithm. The complex Gaussian data vector **z** is produced by

$$z_k = \sum_{n=0}^{M_s-1} y_n \exp(2\pi i n k / M_S) \tag{A1}$$

where y_n are zero mean complex Gaussian random variables with

$$\langle y_n y_m^* \rangle = Y_n \delta_{n-m} \tag{A2}$$

and

$$Y_n = \frac{1}{M_S} \sum_{k=0}^{M_s-1} R_k \exp(-2\pi i n k / M_S) \tag{A3}$$

where R_k is the desired covariance of the stationary data. The random vector **z** then has the properties

$$\langle z_k z_l^* \rangle = R_{k-l} = \langle z_k z_{M_s-l}^* \rangle \tag{A4}$$

and the first points of the simulated data are correlated with the end points. Therefore, a simulation of length $M_S=2M$ is required to generate an independent realization of length M. The length M_S must be long enough to ensure that all Y_n are positive [see Eq. (A3)]. Zmic (1975) and Sirmans, and Bumgarner, (1975) used this algorithm with Y_n chosen to produce exact sampling of the spectrum instead of an exact sampling of the covariance. For Doppler lidar, the covariance of the data is specified by the transmitted pulse and lidar system parameters [Frehlich, 1993b].

REFERENCES

Anderson, J. R., 1991: High performance velocity estimators for coherent laser radars. *Sixth Topical Meeting on Coherent Laser Radar: Technology and Applications*, (Snowmass-at-Aspen, CO), OSA, 216-218.

Bilbro, J. W., C. DiMarzio, D. Fitzjarrald, S. Johnson, and W. Jones, 1986: Airborne Doppler lidar measurements. *Appl. Opt.*, **25**, 2952-2960.

Capon, J., 1969: High resolution frequency-wavenumber spectrum analysis. *Proc. IEEE*, **57**, 1408-1418.

Dabas, A., Ph. Salamitou, D. Oh, M. Georges, J. L. Zarader, and P. H. Flamant, 1993: Lidar signal simulation and processing. *Seventh Topical Meeting on Coherent Laser Radar Applications and Technology*, 221-228.

Doviak, R. J., and D. S. Zrnic, 1984: second edition 1993: *Doppler radar and weather observations*, Academic Press

Frehlich, R. G. and M. J. Kavaya, 1991: Coherent laser radar performance for general atmospheric refractive turbulence. *Appl. Opt.*, **30** 5325-5352.

Frehlich, R. G., 1993a: Cramer-Rao Bound for Gaussian random processes and applications to radar processing of atmospheric signals. *IEEE Trans. Geo. Sci. Remote Sensing*, (in press).

Frehlich, R. G., 1993b: Coherent Doppler lidar signal covariance including wind shear and wind turbulence. *Applied Optics*, (submitted).

Gal-chen, T., M. Xu, and W. L. Eberhard, 1992: Estimations of atmospheric boundary layer fluxes and other turbulence parameters from Doppler lidar data. *J. Geophys. Res.*, **97**, 409-418.

Hardesty, R. M., 1986: Performance of a discrete spectral peak frequency estimator for Doppler wind velocity measurements. *IEEE Trans. Geosci. Remote Sensing,, GE–24, 777-783.*

Helstrom, C. W., 1968: Statistical theory of signal detection, Pergamon Press.

Henderson, S. W., C. P. Hale, J. R. Magee, M. J. Kavaya, and A. V. Huffaker, 1991: Eye-safe coherent laser radar system at 2.1 μm using Tm,Ho:YAG lasers. *Opt. Lett.*, **16**, 773-775.

Henderson, S. W., P. J. M. Suni, C. P. Hale, S. M. Hannon, J. R. Magee, D. L. Bruns, and E. H. Yuen, 1993: Coherent laser radar at 2 μm using solid-state lasers. *IEEE Trans. Geo. Remote Sensing*, **31**, 4-15.

Kavaya, M. J., S. W. Henderson, J. R. Magee, C. P. Hale, and R. M. Huffaker, 1992: Remote wind profiling with a solid-state nd:yag coherent lidar system. *Opt. Let.*, **14**, 776-778.

Kay, S. M., and S. L. Marple, Jr., 1981: Spectrum analysis- A modern perspective. *Proc. IEEE*, **69**, 1380-1419.

Levin, J. M., 1965: Power spectrum parameter estimation. *IEEE Trans. Information Theory, IT–11*, 100-107.

Mahapatra, P. R., and D. S. Zrnic, 1983: Practical algorithms for mean velocity estimation in pulse Doppler weather radars using a small number of samples. *IEEE Trans. Geosci. Electronics, GE–21*, 491-501.

Marple, S. L. Jr., 1987: *Digital Spectral Analysis with Applications*, Prentice-Hall, Inc.

May, P. T., and R. G. Strauch, 1989: An examination of Wind Profiler signal processing algorithms. *L. Atmos. Oceanic Tech.*, **6**, 731-735.

May, P. T., T. Sato, M. Yamamoto, S. Kato, T. Tsuda, and S. Fukao, 1989: Errors in the determination of wind speed by Doppler radar. *L. Atmos. Oceanic Tech.*, **6**, 235-242.

Miller, K.S., and M.M. Rochwarger, 1972: A covariance approach to spectral moment estimation. *IEEE Trans. Information Theory, IT*–**18**, 588-596.

Pearson, G. N. and B. J. Rye, 1992: Frequency fidelity of a compact CO_2 Doppler lidar transmitter. *Appl. Opt.*, **31**, 6475-6484.

Petheram, J. C., G. Frohbeiter, and A. Rosenberg, 1989: Carbon dioxide Doppler lidar wind sensor on a space station polar platform. *Appl. Opt.*, **28**, 834-839.

Post, M. J. and R. E. Cupp, 1990: Optimizing a pulsed Doppler lidar. *Appl. Opt.* , **29**, 4145-4158.

Press, W. H., B. P. Flannery, S. A. Teukolsky, W. T. Vetterling, 1986: *Numerical Recipes, The art of scientific computing*, Cambridge University Press.

Rye, B. J., and R. M. Hardesty, 1993a: Discrete spectral peak estimation in incoherent backscatter heterodyne lidar. I. Spectral accumulation and the Cramer-Rao lower bound. *IEEE Trans. Geo. Sci. Remote Sensing*, **31**, 16-27.

Rye, B. J., and R. M. Hardesty, 1993b: Discrete spectral peak estimation in incoherent backscatter heterodyne lidar. II. Correlogram accumulation. *IEEE Trans. Geo. Sci. Remote Sensing*, **31**, 28-35.

Rye, B. J., and R. M. Hardesty, 1993c: Cramer-Rao lower bound-limited Doppler estimation using discrimination, *Seventh Topical Meeting on Coherent Laser Radar Applications and Technology*, 217-220.

Scharf, L. L., 1991: *Statistical signal processing*, Addison-Wesley.

Shirakawa, M. and D. S. Zmic, 1983: The probability density of a maximum likelihood mean frequency estimator. *IEEE Trans. Acoust., Speech, Signal Processing, ASSP*–**31**, *1197-1202.*

Sirmans, D. and B. Bumgarner, 1975: Numerical comparison of five mean frequency estimators, *J. Appl. Meteor.*, **14**, 991-1003.

Srivastava, V., M. A. Jarzembski, and D. A. Bowdle, 1992: Comparison of calculated aerosol backscatter at 9.1- and 2.1 μm wavelengths. *Appl. Opt.*, **31**, *1904-1906.*

Van Trees, H. L., 1968: *Detection, Estimation, and Modulation Theory, Part I*, John Wiley and Sons, Inc.

Whittle, P., 1953: The analysis of multiple stationary time series. *J. Roy. Statist. Soc.*, **15**, 125-139.

Zmic, D. S., 1975: Simulation of weatherlike Doppler spectra and signals. *J. Appl. Meteor.*, **14**, 619-620.

Zmic, D. S., 1979: Estimation of spectral moments of weather echoes. *IEEE Trans. Geosci. Electronics, GE*–**17**, 113-128.

Figure Captions

Fig.1 Simulation of Doppler lidar data for a 2 μm lidar [Henderson et al, 1993], with N=1.0, SNR=10, f=5MHz, w=0.2MHz, T_S=20$nsec$. The range weighting function $P_L(t-2R/c)$ is shown for the signal at 2μs and 6μs. The FWHM Δr of the pulse sensing volume, the distance Δp that the pulse moves in 4μs, the signal correlation time $\Delta\tau$, and the periodogram Eq. (15) are also shown.

Fig.2 The normalized CRB's σ_f for estimation of mean frequency f, σ_S for estimating signal power S, and σ_w for estimating spectral width w as a function of M for Φ=10 and Ω = 0.2 (___), 0.5 (....), 1.0 (- - -), 2.0 (. - . -), and 5.0 (. . - . . -).

Fig.3 The histograms (+) from 10000 ML and PP estimates of mean frequency $\hat{f}=k_f\Delta f$ where k_f is the mean-frequency index, Φ=10, Ω=0.5, and M=32. The best fit empirical model Eq. (34) for the PDF is indicated by (___) and the histogram determined from the best fit PDF is indicated (O).

Fig.4 The standard-deviation g of the "good" ML estimates for mean-frequency and the fraction b of "bad" estimates as a function of Φ for Ω=0.5 and M=32. The results of the simulation are indicated by (O) and the best fit empirical models Eqs. (39) and (40) are indicated by (____). The exact CRB is (....) and the empirical model corrected for bias by Eq. (38) is indicated by (- - -).

Fig.5 The standard-deviation g of the "good" PML estimates for mean-frequency and the fraction b of "bad" estimates as a function of Φ for Ω=0.5 and M=32. The results of the simulation are indicated by (O) and the best fit empirical models Eqs. (39) and (40) are indicated by (____). The exact CRB is (....) and the periodogram CRB is indicated by (- - -) [Frehlich, 1993a].

Fig.6 The standard-deviation g of the "good" estimates for mean-frequency and the fraction b of "bad" estimates as a function of Φ for Ω=0.5 and M=32. The results of the simulation are given by the best fit empirical models Eqs. (39) and (40) for the ML (____), PML (....), MVYW, (- - -), and PP (. - . -).

Fig.7 The standard-deviation g of the "good" estimates for mean-frequency and the fraction b of "bad" estimates as a function of Φ for Ω=2.0 and M=32. The results of the simulation are given by the best fit empirical models Eqs. (39) and (40) for the ML (____), PML (....), MVYW, (- - -), and PP (. - . -).

Fig.8 The standard-deviation g of the "good" ML estimates for mean-frequency and the fraction b of "bad" estimates as a function of Φ for Ω=0.5. The results of the simulation are given by the best fit empirical models Eqs. (39) and (40) for M = 32 (___), 64 (....), and 128 (- - -).

Fig.9 The standard-deviation g of the "good" ML estimates for mean-frequency and the fraction b of "bad" estimates as a function of Φ for Ω=2.0. The results of the simulation are given by the best fit empirical models Eqs. (39) and (40) for M = 32 (___), 64 (....), and 128 (- - -).

Fig.10 The CRB for estimation of mean frequency for multiple pulses with fixed total energy (fixed Φ) and Ω= 0.2 (___), 0.5 (....), 1.0 (- - -), 2.0 (. - . -), and 5.0 (.. - .. -).

Fig.11 The standard-deviation g of the "good" ML estimates for mean-frequency for Doppler lidar and the fraction b of "bad" estimates as a function of Φ for different number of pulses per estimate with the total signal energy per estimate fixed and Ω=0.5. The results of the simulation are given by the best fit empirical models Eqs. (39) and (40) for 1 pulse (____), 5 pulses (....), and 10 pulses (- - -).

Fig.12 The standard-deviation g of the "good" ML estimates for mean-frequency for Doppler lidar and the fraction b of "bad" estimates as a function of Φ for different number of pulses per estimate with the total signal energy per estimate fixed and Ω=2.0. The results of the simulation are given by the best fit empirical models Eqs. (39) and (40) for 1 pulse (____), 5 pulses (....), and 10 pulses (- - -).

Fig.1 Simulation of Doppler lidar data for a 2 μm lidar [Henderson et al, 1993], with $N=1.0$, $SNR=10$, $f=5MHz$, $w=0.2MHz$, $T_S=20nsec$. The range weighting function $P_L(t-2R/c)$ is shown for the signal at $2\mu s$ and $6\mu s$. The FWHM Δr of the pulse sensing volume, the distance Δp that the pulse moves in $4\mu s$, the signal correlation time $\Delta\tau$, and the periodogram Eq. (15) are also shown.

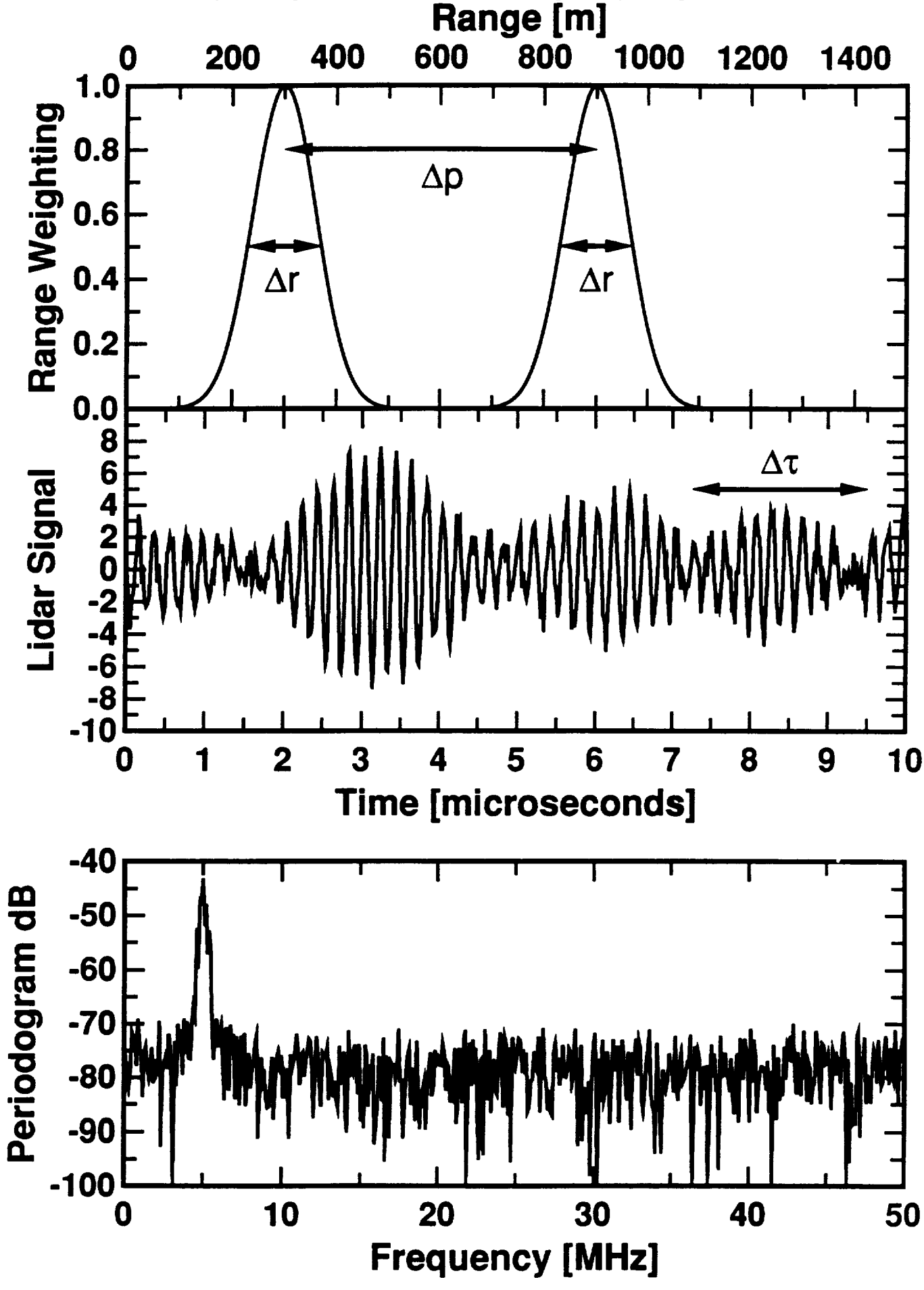

Figure 2 Frehlich JTech No. 93052002

Fig.2 The normalized CRB's σ_f for estimation of mean frequency f, σ_S for estimating signal power S, and σ_w for estimating spectral width w as a function of M for Φ=10 and Ω = 0.2 (___), 0.5 (....), 1.0 (- - -), 2.0 (. - . -), and 5.0 (. . - . . -).

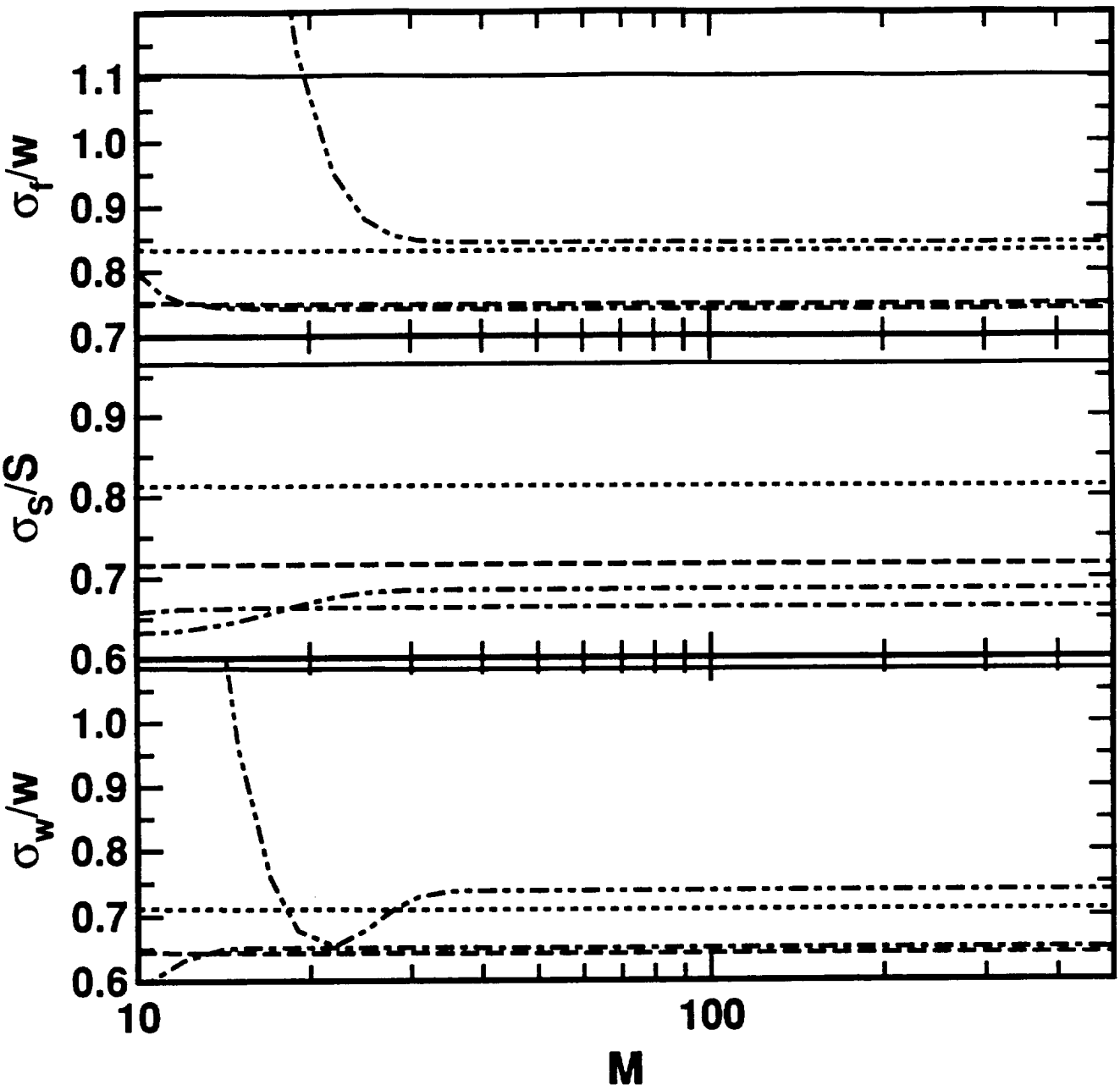

Figure 3 Frehlich JTech No. 93052002

Fig.3 The histograms (+) from 10000 ML and PP estimates of mean frequency $\hat{f}=k_f \Delta f$ where k_f is the mean-frequency index, Φ=10, Ω=0.5, and M=32. The best fit empirical model Eq. (34) for the PDF is indicated by (___) and the histogram determined from the best fit PDF is indicated (O).

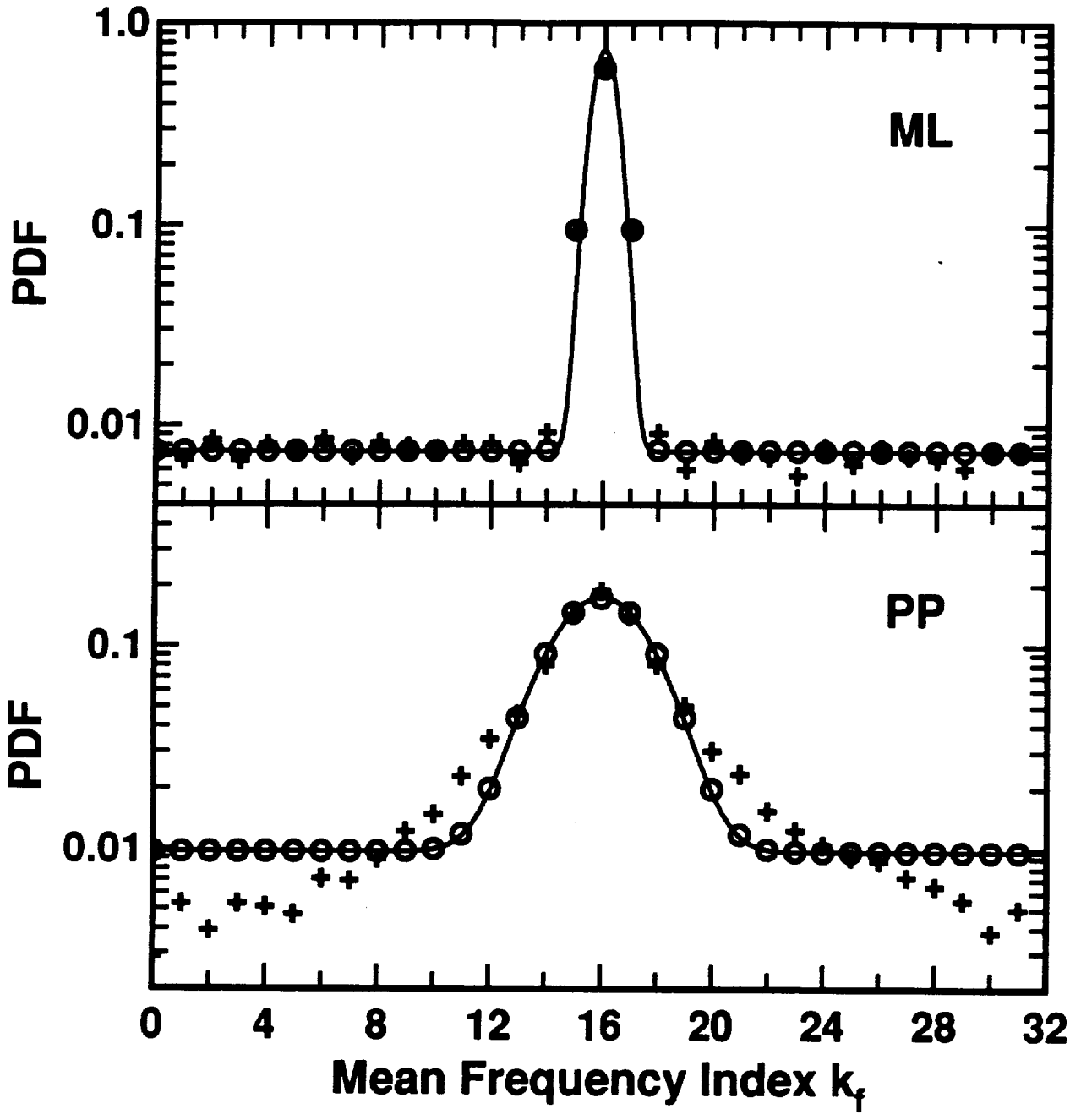

Figure 4 Frehlich JTech No. 93052002

Fig.4 The standard-deviation g of the "good" ML estimates for mean-frequency and the fraction b of "bad" estimates as a function of Φ for Ω=0.5 and M=32. The results of the simulation are indicated by (O) and the best fit empirical models Eqs. (39) and (40) are indicated by (____). The exact CRB is (....) and the empirical model corrected for bias by Eq. (38) is indicated by (- - -).

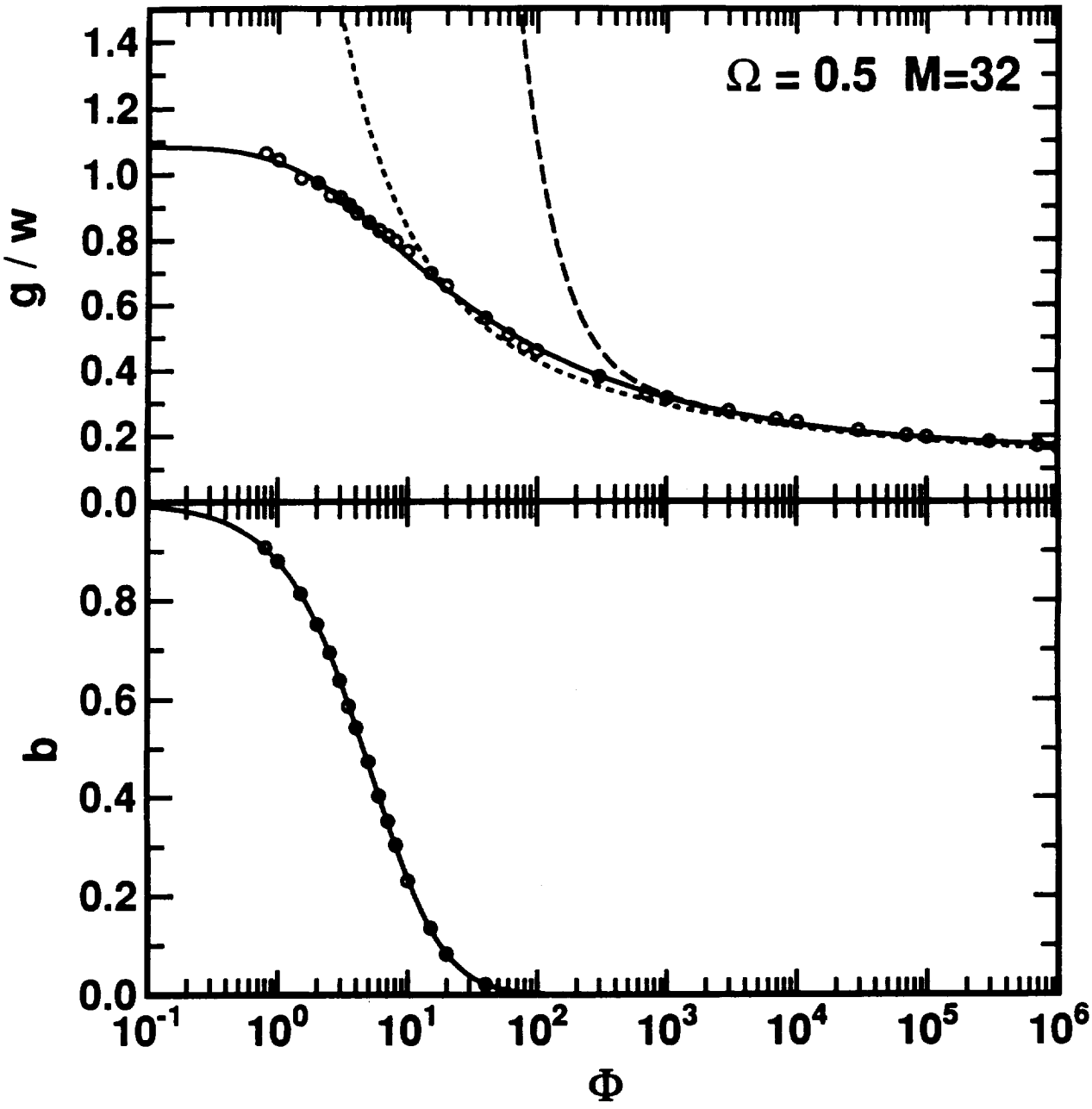

Figure 5 Frehlich JTech No. 93052002

Fig.5 The standard-deviation g of the "good" PML estimates for mean-frequency and the fraction b of "bad" estimates as a function of Φ for Ω=0.5 and M=32. The results of the simulation are indicated by (O) and the best fit empirical models Eqs. (39) and (40) are indicated by (____). The exact CRB is (....) and the periodogram CRB is indicated by (- - -) [Frehlich, 1993a].

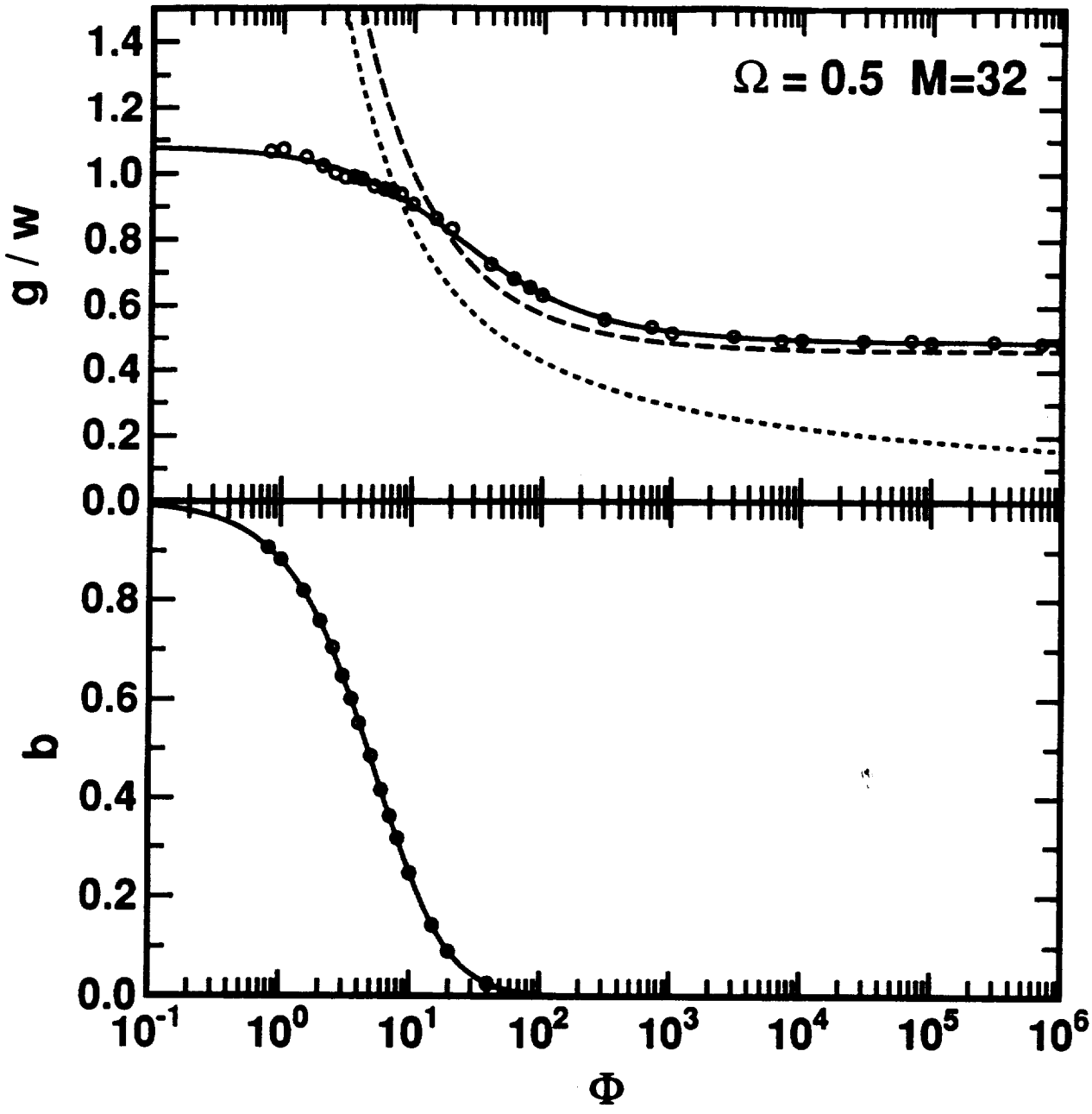

Figure 6 Frehlich JTech No. 93052002

Fig.6 The standard-deviation g of the "good" estimates for mean-frequency and the fraction b of "bad" estimates as a function of Φ for Ω=0.5 and M=32. The results of the simulation are given by the best fit empirical models Eqs. (39) and (40) for the ML (____), PML (....), MVYW, (- - -), and PP (. - . -).

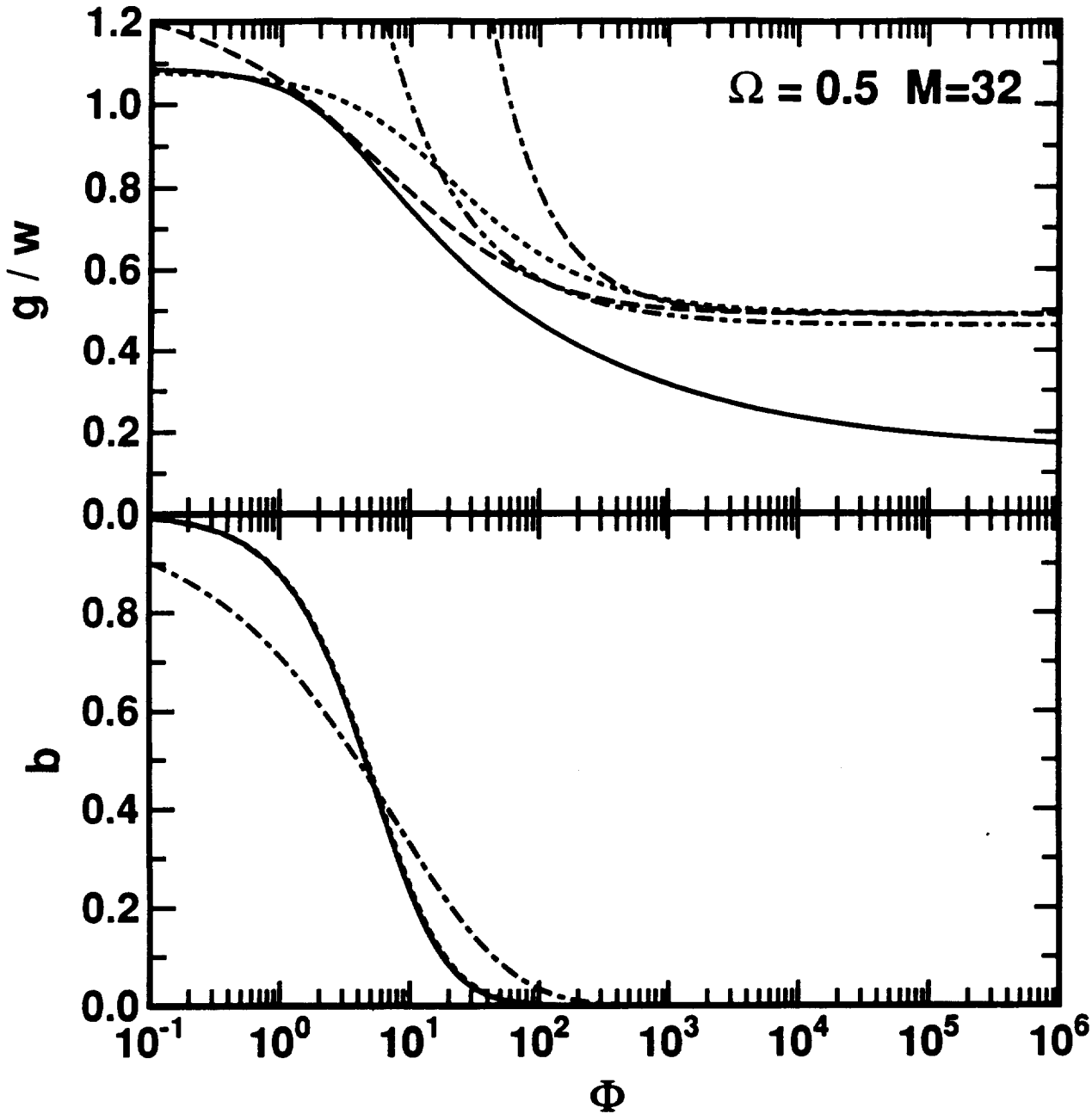

Figure 7 Frehlich JTech No. 93052002

Fig.7 The standard-deviation g of the "good" estimates for mean-frequency and the fraction b of "bad" estimates as a function of Φ for Ω=2.0 and M=32. The results of the simulation are given by the best fit empirical models Eqs. (39) and (40) for the ML (____), PML (....), MVYW, (- - -), and PP (. - . -).

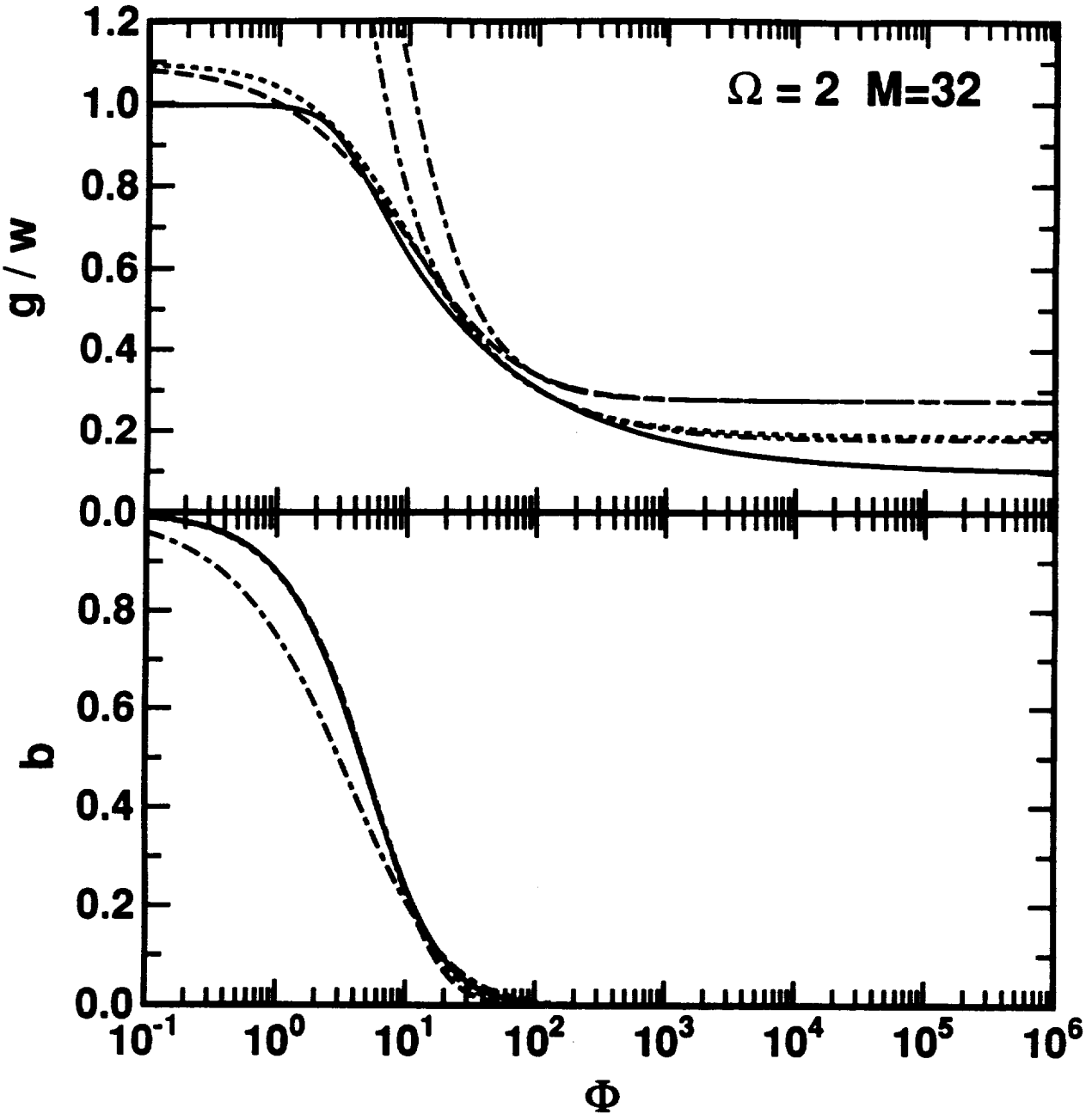

Figure 8 Frehlich JTech No. 93052002

Fig.8 The standard-deviation g of the "good" ML estimates for mean-frequency and the fraction b of "bad" estimates as a function of Φ for Ω=0.5. The results of the simulation are given by the best fit empirical models Eqs. (39) and (40) for M = 32 (___), 64 (....), and 128 (- - -).

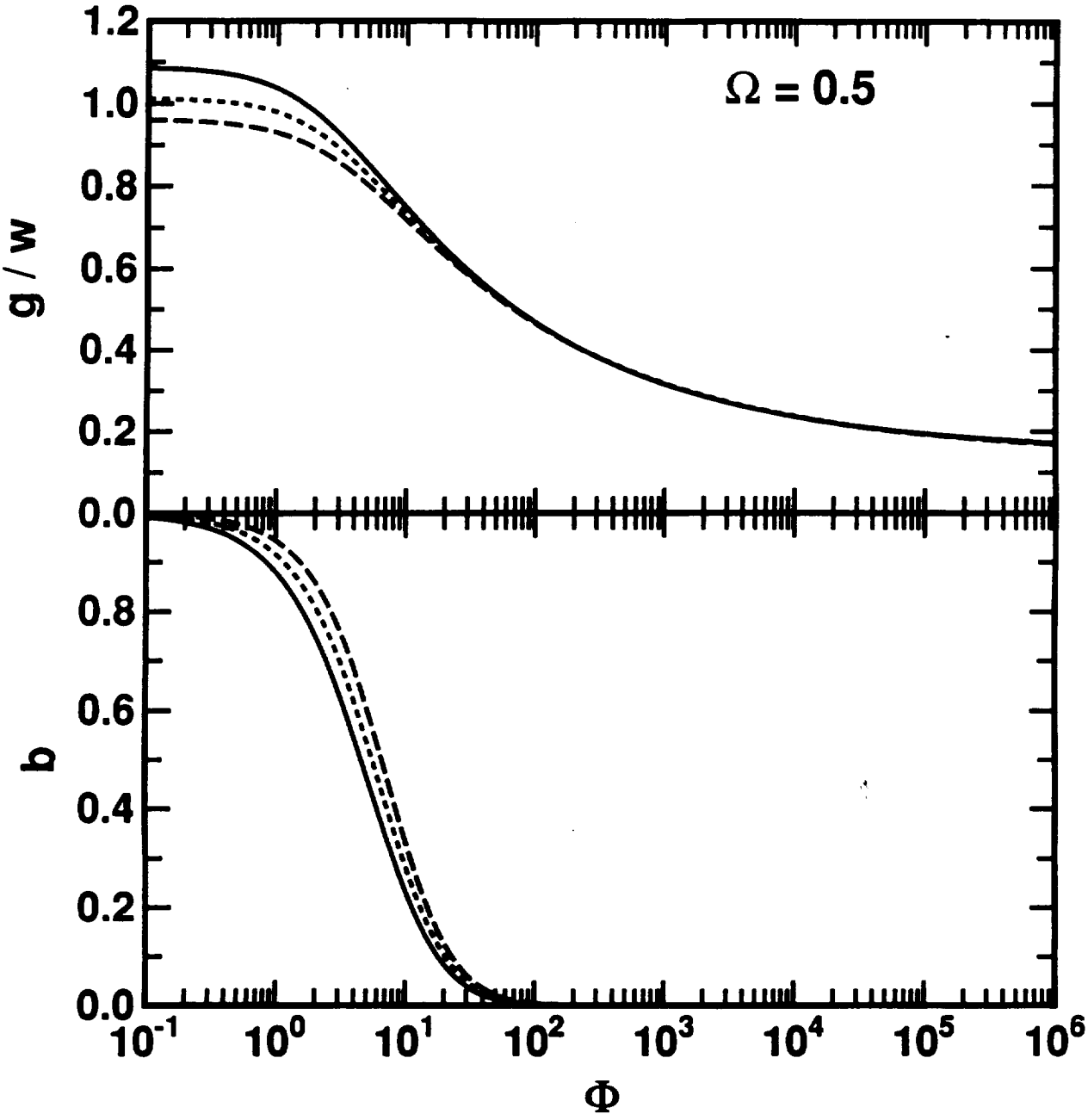

Figure 9 Frehlich JTech No. 93052002

Fig.9 The standard-deviation g of the "good" ML estimates for mean-frequency and the fraction b of "bad" estimates as a function of Φ for Ω=2.0. The results of the simulation are given by the best fit empirical models Eqs. (39) and (40) for M = 32 (___), 64 (....), and 128 (- - -).

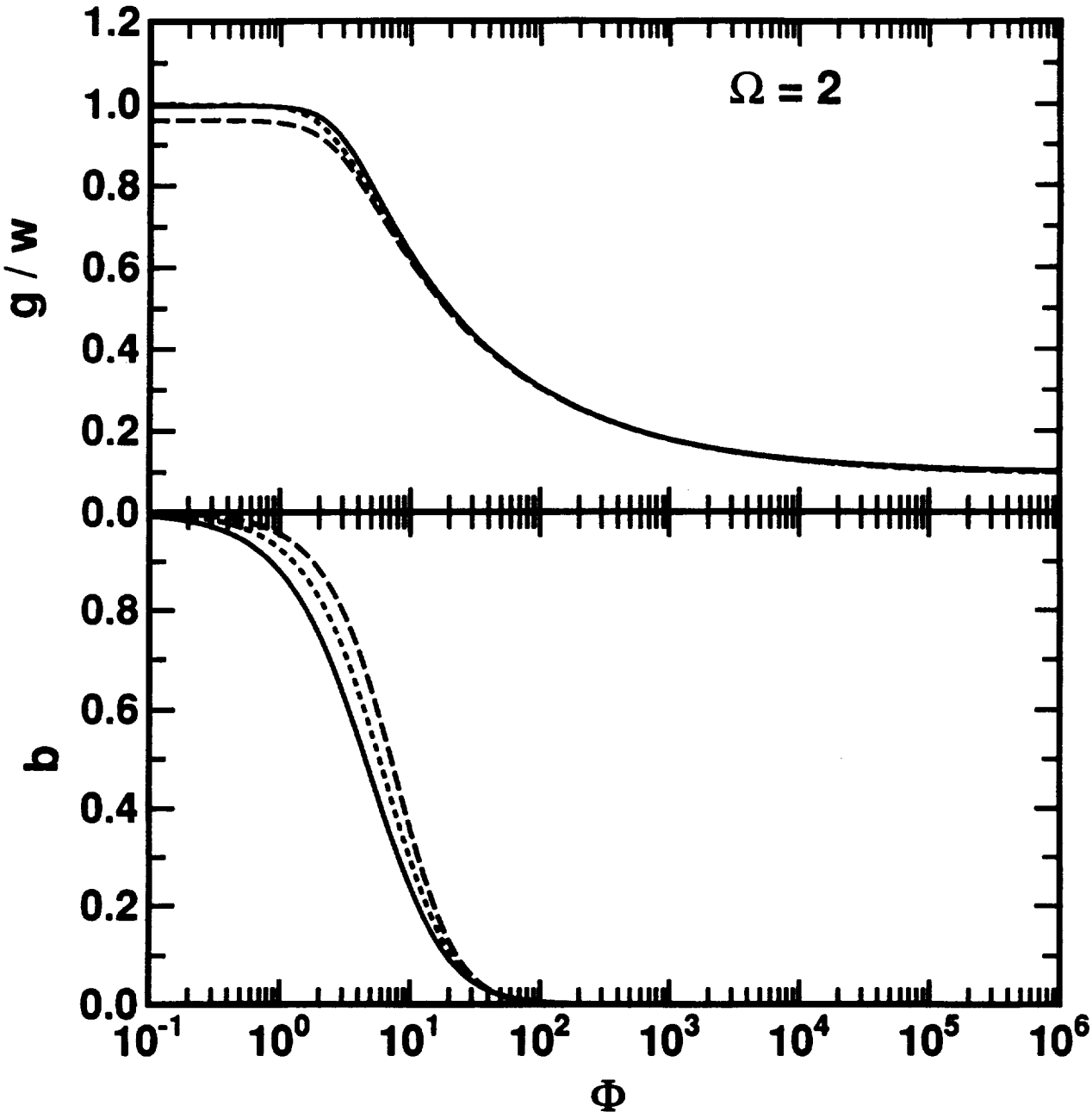

Figure 10 Frehlich JTech No. 93052002

Fig.10 The CRB for estimation of mean frequency for multiple pulses with fixed total energy (fixed Φ) and Ω= 0.2 (___), 0.5 (....), 1.0 (- - -), 2.0 (. - . -), and 5.0 (.. - .. -).

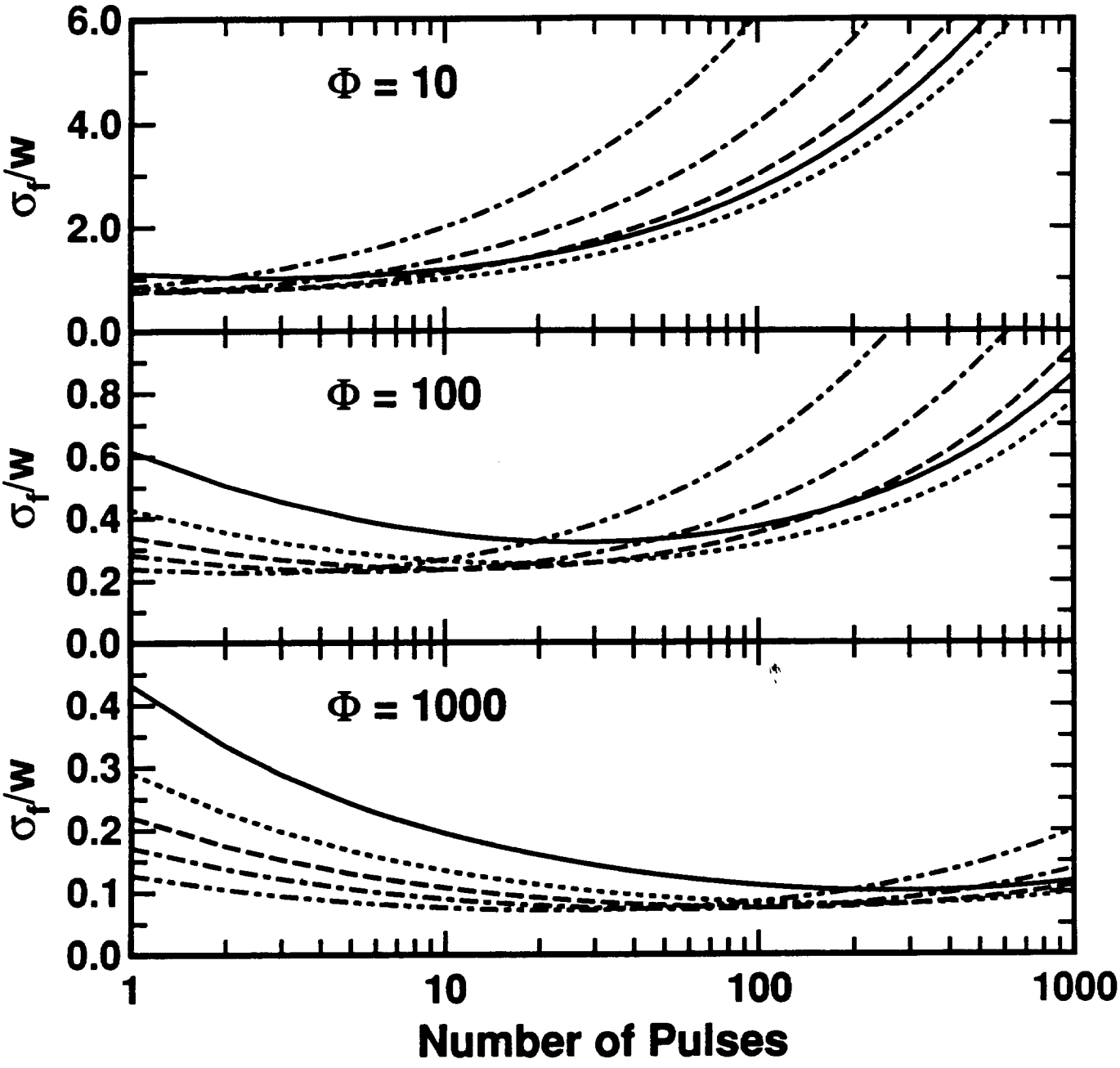

Figure 11 Frehlich JTech No. 93052002

Fig.11 The standard-deviation g of the "good" ML estimates for mean-frequency for Doppler lidar and the fraction b of "bad" estimates as a function of Φ for different number of pulses per estimate with the total signal energy per estimate fixed and Ω=0.5. The results of the simulation are given by the best fit empirical models Eqs. (39) and (40) for 1 pulse (____), 5 pulses (....), and 10 pulses (- - -).

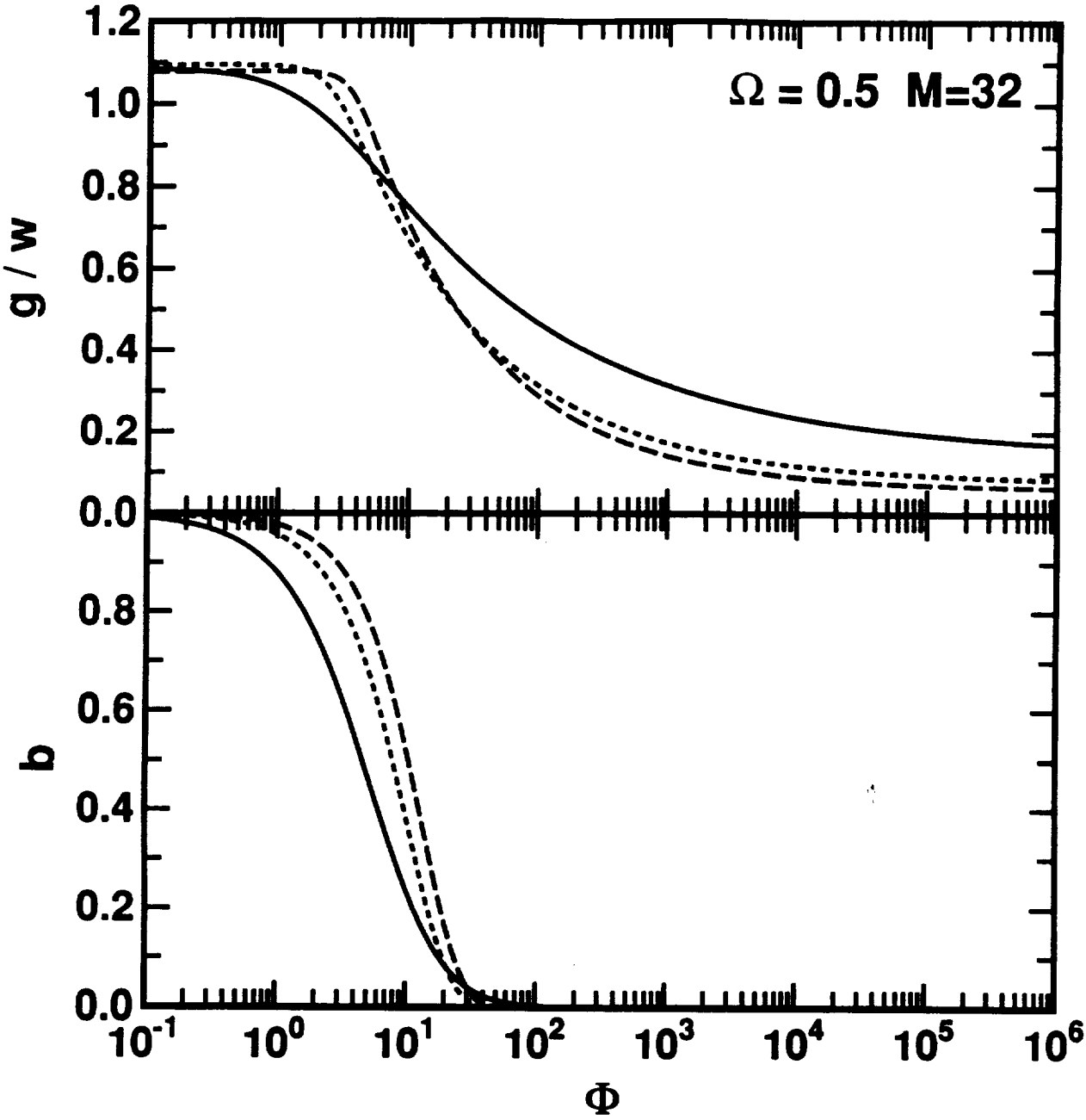

Figure 12 Frehlich JTech No. 93052002

Fig.12 The standard-deviation g of the "good" ML estimates for mean-frequency for Doppler lidar and the fraction b of "bad" estimates as a function of Φ for different number of pulses per estimate with the total signal energy per estimate fixed and Ω=2.0. The results of the simulation are given by the best fit empirical models Eqs. (39) and (40) for 1 pulse (____), 5 pulses (....), and 10 pulses (- - -).

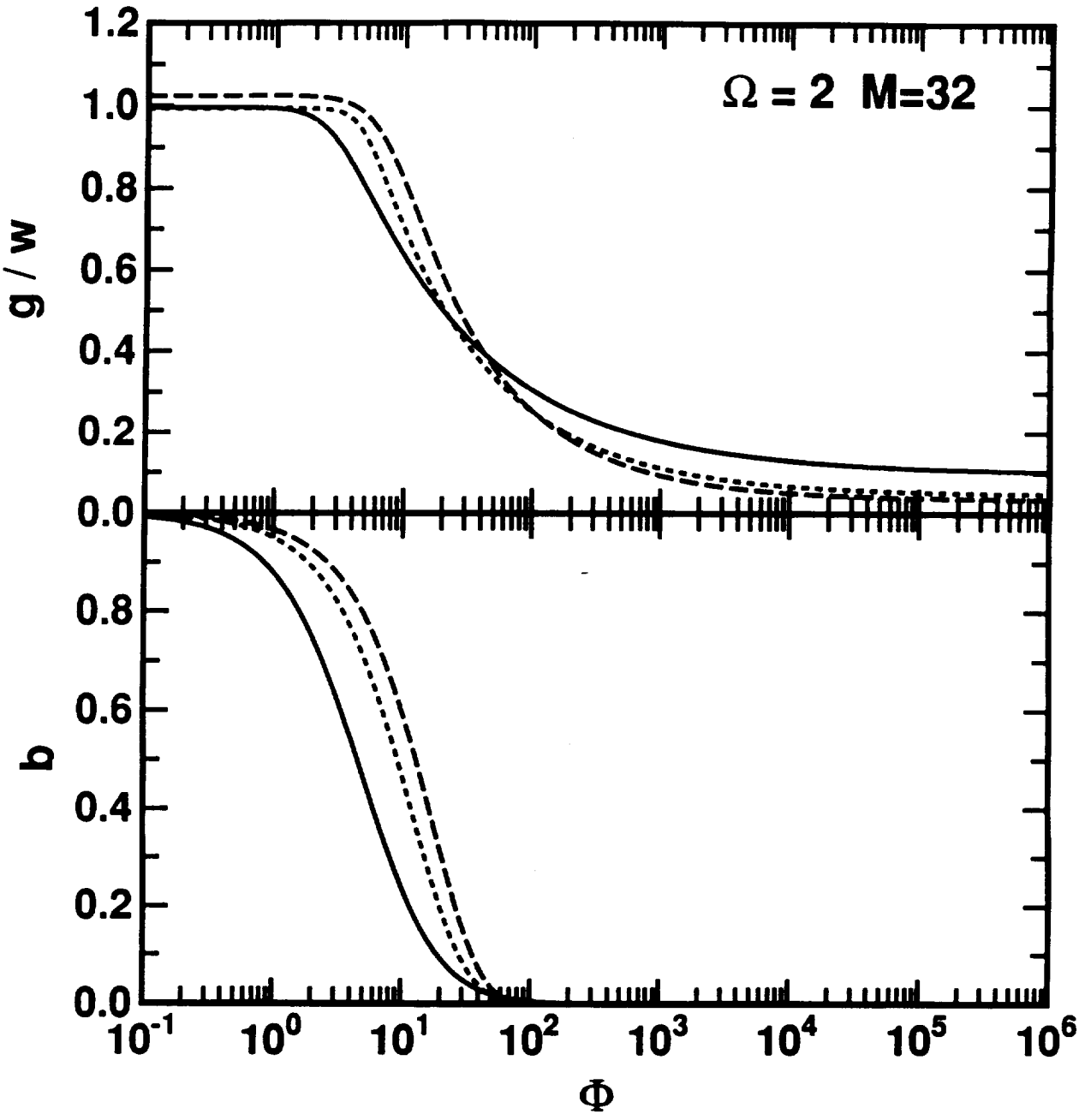

Cramer-Rao Bound for Gaussian Random Processes and Applications to Radar Processing of Atmospheric Signals

Rod Frehlich
National Aeronautics and Space Administration
Marshall Space Flight Center
Optical Systems Branch EB23
Huntsville, Alabama 35812

Submitted to IEEE Transactions on Acoustics, Speech, and Signal Processing, December 20, 1991.

Transferred to IEEE Transactions on Geosience and Remote Sensing, June 1, 1992.

ABSTRACT Calculations of the exact Cramer-Rao Bound (CRB) for unbiased estimates of the mean frequency, signal power, and spectral width of Doppler radar/lidar signals (a Gaussian random process) are presented. Approximate CRB's are derived using the Discrete Fourier Transform (DFT). These approximate results are equal to the exact CRB when the DFT coefficients are mutually uncorrelated. Previous high SNR limits for CRB's are shown to be inaccurate because the discrete summations cannot be approximated with integration. The performance of an approximate maximum likelihood estimator for mean frequency approaches the exact CRB for moderate signal to noise ratio and moderate spectral width.

EDICS - 2.1, 4.1, 4.9.1, 5.1, 5.2, 6.3.2

I. INTRODUCTION

The estimation of the mean frequency, signal power, or spectral width of radar, sonar, lidar, and Synthetic-Aperture-Radar (SAR) returns [1-28] is important for remote sensing. Many estimation algorithms have been investigated, including pulse pair [11,24,26], peak frequency[4], spectral domain [1,3-13,17,18], maximum entropy [8,9,17,18], and maximum likelihood [1,3,7,17,18]. The use of accumulated periodograms or correlograms for mean frequency estimation has been investigated by Rye and Hardesty [17,18]. Many spectral domain algorithms have been reviewed by Kay and Marple [7].

Doppler radar data from atmospheric returns is sampled from the output of a complex receiver [29,30]. For Doppler radar the scattering targets are atmospheric refractive index irregularities, rain, snow, or insects. For Doppler Lidar the scattering targets are atmospheric aerosols. In both cases, the received signal is well represented as a Gaussian random process because the total backscattered field is the superposition of many randomly phased scattered fields. For Doppler radar, the time series is generated by transmitting a series of pulses. For Doppler lidar, the time series is the return signal from a single transmitted pulse. The spectral width of a Doppler lidar signal is usually smaller than the spectral width of a Doppler radar signal for the same range resolution because the effects of velocity fluctuations over the sensing volume of the lidar pulse is smaller than for the radar case. The mean frequency of the return signal provides an estimate of the radial component of the velocity field averaged over the sensing volume of the pulse [2].

The ideal performance of an estimator of the signal parameters is given by the Cramer-Rao Bound (CRB) [16,30,31]. The exact CRB has been determined for the cases of a sine wave with random amplitude and phase in white noise [26], and for an autoregressive signal model [16]. The exact CRB for parameter estimation of a Gaussian random process have been derived but not applied to the Doppler radar/lidar problem. A new, more efficient expression for the exact CRB for estimates of the mean frequency of a complex Gaussian signal added to complex Gaussian uncorrelated noise is derived. For this data model, it is shown that the exact CRB's of all the signal parameters are independent of the mean frequency. Approximate calculations of CRB have been discussed by Whittle [21], Zrnic [26], and Levin

---

Most of this work was performed while the author was a National Research Council Senior Research Fellow at NASA. Current address is Cooperative Institute for Research in the Environmental Sciences (CIRES) University of Colorado, Boulder, CO 80309 (303)-492-6776

[10]. These approximations are essentially large sample approximations. Approximate CRB's are developed by demonstrating that the CRB of a complex Gaussian process is unchanged by the Discrete Fourier Transform (DFT), a unitary transformation. Approximate CRB's for the signal parameters are derived using the periodogram (squared modulus of the DFT) of the data. These periodogram CRB's are equal to the exact CRB when the periodogram elements are mutually uncorrelated. The maximum correlation coefficient can be calculated thus providing an efficient test for the validity of the approximate CRB. The periodogram CRB's and Levin's approximate CRB's are compared with the exact CRB's for a complex Gaussian signal in complex Gaussian uncorrelated noise with a Gaussian covariance function for the signal. The performance of an approximate maximum likelihood estimator (ML) for the mean frequency f is compared to the CRB. The validity of previous analytic approximations for the CRB for mean frequency are determined. A summary concludes the paper.

II. THEORETICAL DEVELOPMENT

A. Exact Cramer-Rao Bounds

Doppler radar signals are well represented as a zero-mean complex Gaussian random process [29,30] z_k where $\mathbf{z}$ is a column vector of M samples,

$$E[z_k z_l] = 0 \tag{1}$$

and $E[\cdot]$ denotes ensemble average. The statistics of $\mathbf{z}$ are completely determined by the covariance matrix [31,33]

$$\underline{\mathbf{R}}(\boldsymbol{\theta}) = E[\mathbf{z}.\mathbf{z}^{*T}] \quad R_{kl}(\boldsymbol{\theta}) = E[z_k z_l^*] \tag{2}$$

where $\boldsymbol{\theta}$ is the vector of parameters of the process, the row vector $\mathbf{z}^T$ is the transpose of $\mathbf{z}$, * denotes complex conjugation, and R_{kl} denotes the elements of the covariance matrix $\underline{\mathbf{R}}$.

The variance of an unbiased estimate $\hat{\theta}_i$ of the parameter θ_i has a lower bound called the Cramer-Rao bound (CRB) which is given by [18,31]

$$VAR[\hat{\theta}_i] = E[(\hat{\theta}_i - \theta_i)^2] \geq J^{ii}(\boldsymbol{\theta}) \tag{3}$$

where J^{ii} is the i^{th} element of the diagonal of the inverse of the Fisher information matrix $\underline{\mathbf{J}}$, with elements given by [18,31]

$$J_{kl} = \frac{\partial^2 \ln[|\underline{\mathbf{R}}(\boldsymbol{\theta})|]}{\partial\theta_k \partial\theta_l} + E\left[\mathbf{z}^{*T} \frac{\partial^2 \underline{\mathbf{R}}^{-1}(\boldsymbol{\theta})}{\partial\theta_k \partial\theta_l} \mathbf{z}\right] = \frac{\partial^2 \ln[|\underline{\mathbf{R}}(\boldsymbol{\theta})|]}{\partial\theta_k \partial\theta_l} + tr\left\{\underline{\mathbf{R}} \frac{\partial^2 \underline{\mathbf{R}}^{-1}(\boldsymbol{\theta})}{\partial\theta_k \partial\theta_l}\right\} \tag{4}$$

where $|\underline{\mathbf{R}}|$ denotes the determinant of the matrix $\underline{\mathbf{R}}$ and $tr\{\underline{\mathbf{R}}\}$ denotes the trace of matrix $\underline{\mathbf{R}}$. This result is difficult to evaluate because the inverse of the matrix $\underline{\mathbf{R}}$ is required before the derivatives are computed. However, for a zero mean complex Gaussian process [17,15]

$$J_{kl} = tr\left\{\underline{\mathbf{R}}^{-1}(\boldsymbol{\theta}) \frac{\partial \underline{\mathbf{R}}(\boldsymbol{\theta})}{\partial\theta_k} \underline{\mathbf{R}}^{-1}(\boldsymbol{\theta}) \frac{\partial \underline{\mathbf{R}}(\boldsymbol{\theta})}{\partial\theta_l}\right\}. \tag{5}$$

Exact calculations of the CRB simplify for the common model of Doppler radar or Doppler lidar atmospheric signals given by

$$z_k = s_k \exp(2\pi i f k T_S) + n_k \tag{6}$$

where s_k and n_k are complex Gaussian random processes, $f[Hz]$ is the mean frequency of the signal, $T_S[sec]$ is the sampling interval, the noise samples n_k are statistically independent of the signal s_k,

$$E[n_k n_l] = 0 \quad E[n_k n_l^*] = N\delta_{k-l}\ , \tag{7}$$

N is the average noise power per sample and δ_k is the Kronecker delta symbol. The statistics of s_k are assumed to be independent of the mean frequency f. The covariance matrix $\underline{\mathbf{R}}$ then becomes [26]

$$\underline{\mathbf{R}}(\boldsymbol{\theta}) = \underline{\mathbf{D}}\,\underline{\mathbf{Q}}(\boldsymbol{\phi})\,\underline{\mathbf{D}}^{*} \tag{8}$$

or

$$R_{kl}(\boldsymbol{\theta}) = Q_{kl}(\boldsymbol{\phi})\exp[2\pi i f T_S(k-l)] \tag{9}$$

where $\underline{\mathbf{D}}$ is a diagonal matrix with elements

$$D_{kk} = \exp(2\pi i f k T_S)\,, \tag{10}$$

Q_{kl} are the elements of the covariance matrix $\underline{\mathbf{Q}}$, the covariance of s_k+n_k, and the system parameters are $\boldsymbol{\theta} = (f, \boldsymbol{\phi})$. The matrix $\underline{\mathbf{D}}$ is a unitary matrix [$\underline{\mathbf{D}}\,\underline{\mathbf{D}}^{*} = \underline{\mathbf{I}}$ where $\underline{\mathbf{I}}$ is the identity matrix]. The determinant of $\underline{\mathbf{R}}$ is equal to the determinant of $\underline{\mathbf{Q}}$ and is independent of the mean frequency f.

The Fisher information matrix for elements involving the parameters $\boldsymbol{\phi}$ are given by

$$J_{kl} = tr\left\{\underline{\mathbf{D}}\,\underline{\mathbf{Q}}^{-1}(\boldsymbol{\phi})\frac{\partial \underline{\mathbf{Q}}(\boldsymbol{\phi})}{\partial \phi_k}\underline{\mathbf{Q}}^{-1}(\boldsymbol{\phi})\frac{\partial \underline{\mathbf{Q}}(\boldsymbol{\phi})}{\partial \phi_l}\underline{\mathbf{D}}^{-1}\right\} = tr\left\{\underline{\mathbf{Q}}^{-1}(\boldsymbol{\phi})\frac{\partial \underline{\mathbf{Q}}(\boldsymbol{\phi})}{\partial \phi_k}\underline{\mathbf{Q}}^{-1}(\boldsymbol{\phi})\frac{\partial \underline{\mathbf{Q}}(\boldsymbol{\phi})}{\partial \phi_l}\right\} \tag{11}$$

since

$$tr\left\{\underline{\mathbf{D}}\,\underline{\mathbf{Q}}\,\underline{\mathbf{D}}^{-1}\right\} = tr\left\{\underline{\mathbf{Q}}\right\} \tag{12}$$

for any matrices $\underline{\mathbf{D}}$ and $\underline{\mathbf{Q}}$. These Fisher information matrix elements are independent of the mean frequency f. The same argument proves that the Fisher information matrix elements involving the mean frequency are also independent of the mean frequency. Therefore, the Fisher information matrix and the CRB's are independent of the mean frequency f for the signal model of Eqs. (6) and (7).

A numerically more efficient expression for the exact CRB of estimators for the mean frequency is produced by writing the inverse of the covariance matrix as

$$\underline{\mathbf{R}}^{-1}(\boldsymbol{\theta}) = \underline{\mathbf{D}}\,\underline{\mathbf{Q}}^{-1}(\boldsymbol{\phi})\,\underline{\mathbf{D}}^{-1} \tag{13}$$

or

$$(\underline{\mathbf{R}}^{-1})_{kl}(\boldsymbol{\theta}) = (\underline{\mathbf{Q}}^{-1})_{kl}(\boldsymbol{\phi})\exp[2\pi i f T_S(k-l)] \tag{14}$$

where $(\underline{\mathbf{R}}^{-1})_{kl}$ denotes the kl element of the matrix $\underline{\mathbf{R}}^{-1}$. The Fisher information matrix element J_{11} for the mean frequency f becomes [substitute Eqs. (9) and (14) into Eq. (4)]

$$J_{11} = -4\pi^2 T_S{}^2 \sum_{k=0}^{M-1}\sum_{l=0}^{M-1}(l-k)^2 Q_{kl}(\underline{\mathbf{Q}}^{-1})_{lk} \tag{15}$$

This result can also be obtained from Eq. (5) by expanding the matrix operations and using the matrix identity $\underline{\mathbf{Q}}\underline{\mathbf{Q}}^{-1}=\underline{\mathbf{I}}$. Eq. (5) has approximately $3M^3+2M^2+M$ floating point operations while Eq. (15) has approximately $2M^2+M$ floating point operations. If the mean frequency f is the only unknown parameter or if the off diagonal elements of $\underline{\mathbf{J}}$ are zero, the CRB for estimation of the mean frequency f is given by

$$\sigma_f^2 \geq 1/J_{11}\,. \tag{16}$$

B. Approximate Cramer-Rao Bounds

The calculation of the CRB is numerically intensive, especially for large M. Asymptotic expressions valid for large M have been derived by Whittle [21], Levin [10], and Zrnic [26]. The region of validity of these results is difficult to determine [10,15] and depends on the parameters of the process as well as M. A new approximate CRB and a criteria for testing the validity of the approximation will be presented here, based on the past work of Levin and Whittle. The approximate CRB's of Whittle, Levin, and Zrnic can be derived from this approximate CRB, however, further approximations are required.

The Discrete Fourier Transform (DFT) of the data vector $\mathbf{z}$ is given by

$$\mathbf{u} = \underline{\mathbf{U}}\,\mathbf{z} \tag{17}$$

where the elements of the unitary matrix $\underline{\mathbf{U}}$ are

$$U_{kl} = M^{-1/2}\exp(-2\pi ikl/M) \tag{18}$$

and

$$u_k = M^{-1/2}\sum_{l=0}^{M-1} z_l \exp(-2\pi ikl/M)\,. \tag{19}$$

Because this is a linear transformation, the vector $\mathbf{u}$ has a joint complex Gaussian probability density function which is a function of the covariance matrix $\underline{\mathbf{R}}'$

$$\underline{\mathbf{R}}' = E[\mathbf{u}\,\mathbf{u}^{*T}] = E[\underline{\mathbf{U}}\,\mathbf{z}\,\mathbf{z}^{*T}\,\underline{\mathbf{U}}^{-1}] = \underline{\mathbf{U}}\,\underline{\mathbf{R}}\,\underline{\mathbf{U}}^{-1}\,. \tag{20}$$

The determinant of the matrix $\underline{\mathbf{R}}'$ is equal to the determinant of the matrix $\underline{\mathbf{R}}$. The Fisher information matrix for the parameters $\boldsymbol{\theta}$ in terms of the statistics of the new vector $\mathbf{u}$ is denoted as $\underline{\mathbf{J}}'$ and given by [see Eq. (4) and (12)]

$$J'_{kl} = \frac{\partial^2 \ln[\,|\underline{\mathbf{R}}(\boldsymbol{\theta})|\,]}{\partial\theta_k\partial\theta_l} + tr\left\{\underline{\mathbf{U}}\,\underline{\mathbf{R}}\frac{\partial^2\underline{\mathbf{R}}^{-1}(\boldsymbol{\theta})}{\partial\theta_k\partial\theta_l}\,\underline{\mathbf{U}}^{-1}\right\} = J_{kl} \tag{21}$$

The Fisher information matrix using the random vector $\mathbf{u}$ is equal to the Fisher information matrix using $\mathbf{z}$. Therefore, the CRB's are identical.

The vector of DFT coefficients $\mathbf{u}$ contain the same information as the original time series $\mathbf{z}$. Assume the random variables u_k are mutually uncorrelated and statistically independent [10]. Then $\underline{\mathbf{R}}'$ is a diagonal matrix with elements

$$R'_{kl} = E[u_k\,u_l^*] = P(k,\boldsymbol{\theta})\delta_{k-l}\,. \tag{22}$$

The function $P(k,\boldsymbol{\theta})$ is the ensemble average of the periodogram

$$\hat{P}(k) = u_k\,u_k^* \tag{23}$$

and can be written as [28]

$$P(k,\boldsymbol{\theta}) = \sum_{n=-(M-1)}^{M-1} R_n(\boldsymbol{\theta})\left(1 - \frac{|n|}{M}\right)\exp(-2\pi ikn/M) \tag{24}$$

and $R_{kl}(\boldsymbol{\theta}) = R_{k-l}(\boldsymbol{\theta})$. The inverse covariance matrix $\underline{\mathbf{R}}'^{-1}$ is a diagonal matrix with elements

$$(\underline{\mathbf{R}}'^{-1})_{kl} = P^{-1}(k,\boldsymbol{\theta})\delta_{k-l}\,. \tag{25}$$

Then, the Fisher information matrix is given by [substitute Eqs. (22) and (25) into Eq. (5)]

$$J'_{kl} = J_{kl} = \sum_{m=0}^{M-1}\frac{d(m,\theta_k)d(m,\theta_l)}{P^2(m,\boldsymbol{\theta})} \tag{26}$$

where

$$d(m,\theta_k) = \frac{\partial P(m,\boldsymbol{\theta})}{\partial\theta_k}\,. \tag{27}$$

For finite M, the accuracy of this approximation for the CRB is determined by the correlation coefficient $\rho(k,l)$ of the periodogram elements which can be written as [28]

$$\rho(k,l) = \frac{1}{P(k,\boldsymbol{\theta})P(l,\boldsymbol{\theta})M^2}\left|\sum_{n=-(M-1)}^{M-1} R_n(\boldsymbol{\theta})\frac{\sin[\pi|n|(k-l)/M]}{\sin[\pi(l-k)/M]}\exp[-2\pi i(k+l)n/M]\right|^2. \tag{28}$$

The results of Whittle and Levin can be obtained from Eq. (26) by assuming the average periodogram can be approximated by the continuous spectrum and approximating the summation as an integral. Zrnic [26] produced an approximate time-domain CRB for the estimation of the mean frequency f and the signal model Eqs. (6) and (7), by assuming $\underline{\mathbf{R}}^{-1}$, the inverse of the covariance matrix $\underline{\mathbf{R}}$, is asymptotically Toeplitz (see ref. [26], Eqs. (A.21), (A.26)). This result can be derived from the approximate periodogram CRB [34].

III. CALCULATIONS

A. Numerical Calculations

The CRB is calculated for the signal model of Eqs. (6) and (7), assuming stationarity of the data $[R_{kl}(\boldsymbol{\theta})=R_{k-l}(\boldsymbol{\theta})]$ and the Gaussian covariance model of Zrnic [26], i.e.,

$$R_k = S\,\exp[-2\pi^2(wkT_S)^2+2\pi i f k T_S]+N\,\delta_k \tag{29}$$

or

$$Q_k = S\,\exp[-2\pi^2(wkT_S)^2]+N\,\delta_k \tag{30}$$

where S is the signal power, f is the mean frequency or Doppler frequency, w the spectral width, N is the noise power, and S/N is the Signal-to-Noise Ratio (SNR). The system parameters are $(\theta_1,\theta_2,\theta_3)=(f,S,w)$. Then

$$P(m,\boldsymbol{\theta}) = N + S\sum_{n=-(M-1)}^{M-1}(1-\frac{|n|}{M})\exp[-2\pi^2w^2T_S{}^2n^2]\exp[-\frac{2\pi in}{M}(m-fMT_S)]\,. \tag{31}$$

The calculations of the approximate CRB simplify if we write the mean frequency f as

$$f = (m_F+\varepsilon)\Delta f \tag{32}$$

where

$$\Delta f = \frac{1}{MT_S} \tag{33}$$

is the frequency resolution of the periodogram, m_F is the mean frequency index, and $-1/2<\varepsilon<1/2$. Then

$$P(m,\boldsymbol{\theta}) = N + S\sum_{n=-(M-1)}^{M-1}(1-\frac{|n|}{M})\exp[-2\pi^2w^2T_S{}^2n^2]\exp[-\frac{2\pi in}{M}(m-m_F-\varepsilon)]\,. \tag{34}$$

The integer m_F is the index of the maximum of the average periodogram and ε is the offset in units of Δf of the true mean frequency from the frequency $m_F\Delta f$. The elements of the Fisher information matrix for the approximate CRB can be written as a DFT. The function $d(m,\theta_2)$ is the coefficient of S in Eq. (34). The other two functions can be written as [see Eq. (31)]

$$d(m,\theta_1) = \frac{\partial P(m,\boldsymbol{\theta})}{\partial f} = 2\pi iST_S\sum_{n=-(M-1)}^{M-1}(1-\frac{|n|}{M})n$$
$$\exp[-2\pi^2w^2T_S{}^2n^2]\exp[-\frac{2\pi in}{M}(m-m_F-\varepsilon)] \tag{35}$$

and

$$d(m,\theta_3) = \frac{\partial P(k,\boldsymbol{\theta})}{\partial w} = -4\pi^2SwT_S{}^2\sum_{n=-(M-1)}^{M-1}(1-\frac{|n|}{M})n^2$$
$$\exp[-2\pi^2w^2T_S{}^2n^2]\exp[-\frac{2\pi in}{M}(m-m_F-\varepsilon)]\,. \tag{36}$$

The approximate CRB is a function of the frequency offset parameter ε. For spectral width $wMT_S>0.5$, there is little dependence on ε [34]. The mean frequency f is an unknown parameter which is usually random. Then ε will be uniformly distributed on the interval $(-1/2,1/2)$. To remove the dependence of ε, the approximate CRB's are calculated using Eqs. (4), (16), (26), (34), (35), (36) and the result averaged over the uniform distribution of ε. We will call this approximate CRB the periodogram CRB.

The correlation coefficient $\rho(k,l)$ is also a function of ε. The average over ε of the maximum correlation coefficient for all k and l is denoted by ρ_{max}. If ρ_{max} is small, the periodogram elements are approximately mutually uncorrelated and the periodogram CRB's are a good approximation for the exact CRB's of unbiased estimates of the parameters of the complex Gaussian random processes **u** and **z**. For all periodogram CRB calculations, the index m_F is set to zero since the summation over index m in Eq.

(26) is independent of m_F. The numerical calculations of the periodogram CRB are performed using the Fast Fourier Transform (FFT) algorithm for the DFT. For the exact CRB, the inverse of the Toeplitz matrix $\underline{Q}$ is calculated using Trench's technique with Durbin's algorithm [35].

Zrnic [26] produced analytic expressions for high SNR

$$\sigma_{\hat{f}}^2 \geq \frac{1}{T_S{}^2 M} \frac{12(wT_S)^4}{[1-12(wTS)^2]} \tag{37}$$

and low SNR

$$\sigma_{\hat{f}}^2 \geq \frac{1}{T_S{}^2} \frac{4\sqrt{\pi}(wT_S)^3}{M} \frac{N^2}{S^2} \tag{38}$$

B. Cramer-Rao Bound for Mean Frequency Estimation

Many different estimators for mean-frequency have been suggested and analyzed. In the limit as $M \rightarrow \infty$ the performance of the maximum likelihood (ML) estimate approaches the CRB [10,20,31,32] and the estimates have a Gaussian distribution. However, the ML estimate is a numerically intensive algorithm. The performance of an approximate ML estimator will be compared to the exact and approximate CRB's. To reduce the computational effort, the spectral width w is assumed known and the signal power S is estimated by

$$\hat{S} = \left| \frac{1}{M} \sum_{m=0}^{M-1} [\hat{P}(m) - N] \right| \tag{39}$$

and $|\cdot|$ denotes absolute value. An approximate maximum likelihood estimate for the mean frequency that assumes knowldege of the spectral width w (this is true when the velocity fluctuations over the sensing volume of the pulse are negligible and the spectral width is determined by the transmitter pulse) is the value $\hat{f}$ [10] that maximizes the log likelihood function L assuming the periodogram elements are mutually uncorrelated, i.e.,

$$L = -\sum_{m=0}^{M-1} \frac{\hat{P}(m)}{P(m, \hat{S}, \hat{f})} . \tag{40}$$

Note that the average periodogram $P(m)$ is used instead of the continuous spectrum [10,17]. This improves performance for narrow spectral width and high SNR. A version of Levin's ML estimator that uses accumulated periodograms has been investigated by Rye and Hardesty [17,18]. To produce a numerically efficient estimator, L is calculated for $\hat{f} = k_f \Delta f, k_f = 1,2,..M$. The performance of this approximate ML estimator was determined from 10000 simulations of random data [3] with $M=128$ using the covariance model Eq. (29) with a mean frequency $f = 0.5/T_S$, i.e., f is located in the center of the periodogram bin $k = M/2$. The Probability Density Function (PDF) of the mean frequency index k_f of these approximate ML estimates is shown in Fig. 1 for $SNR = 0.1$. The PDF's are characterized by a uniform distribution of "bad" estimates and a clump of "good" estimates about the true mean frequency [3,4,11,12,17]. Because the signal power for each estimate is random, there will be realizations where the signal will be hidden in the additive noise and a random noise spike will be chosen as the mean frequency. The "bad" estimates produce a bias which creates a problem for comparison with the CRB calculated for unbiased estimates. One solution is to calculate the CRB for a biased estimator [20,31], but the bias depends on the estimator. This comparison is presented in [3]. We will compare the CRB to the standard deviation of the good estimates around the true mean frequency. A theoretical PDF is calculated assuming two components: a uniform distribution for the "bad" estimates and a Gaussian distribution for the "good" estimates. The standard deviation of the good estimates and the fraction of bad estimates are determined by minimizing the mean square error between the theoretical PDF and the simulated PDF. For the parameters of Fig. 1. and a normalized spectral width $wT_S = 0.01$, 25.1% of the estimates are bad estimates; for $wT_S = 0.1$, 28.8% of the estimates are bad estimates.

A comparison of exact and approximate CRB's for the estimation of the mean frequency is shown in Fig. 2 for $M=128$ data points, as a function of the normalized spectral width wT_S for various SNR.

When the maximum correlation ρ_{max} is small ($\rho_{max}<0.01$), the periodogram CRB is a good approximation to the exact CRB. When the spectral width w is less than the periodogram resolution Δf, the periodogram CRB is larger than the exact CRB and ρ_{max} approaches unity. This is the explanation for the failure of the periodogram CRB and all it's analytic approximations (Whittle's, Levin's, Zrnic's) to agree with the exact CRB in the limit of spectral width approaching zero, (a sine wave with random amplitude and phase) (see Ref [26] Eq. (A.18)). Levin's approximate CRB is slightly lower than the exact CRB for narrow spectral width and much lower at large spectral width.

The performance of the approximate ML estimator is complicated at low SNR by the bias introduced by the bad estimates (see Fig. 1). For SNR=0.1, the standard deviation of the good estimates is below the exact CRB for large spectral width. However, the standard deviation using all the estimates is above the exact CRB. For higher SNR, there is little bias because most of the estimates are distributed around the true mean frequency and the standard deviation of the approximate ML estimates approach the exact CRB for moderate to large spectral width (see also Ref. [1]). For very narrow spectral width all the signal power is located in one periodogram element if $\varepsilon=0$. If the true mean frequency is not centered on a periodogram element ($\varepsilon\neq0$), then the signal power is distributed over more than one periodogram element [2, Chap. 5] and the approximate ML estimate should include the dependence on ε. This regime is rarely encountered in Doppler radar but is important for Doppler Lidar measurements when the wind fields over constant the sensing volume of the pulse. Then the exact maximum likelihood estimator is preferred [3].

A comparison of the exact and approximate CRB's for the estimation of the mean frequency f are shown in Fig. 3 versus SNR for $M=128$ data points and various spectral widths. Again, the approximate periodogram CRB agrees with the exact CRB when the maximum correlation $\rho_{max}<0.01$. Levin's approximate CRB is a good approximation to the exact CRB for this parameter regime. Zrnic's low-SNR analytic expressions for CRB (a) are accurate for only very low SNR. The high-SNR analytic approximation of Zrnic (b) [Eq. (37)] does not agree with the exact CRB due to the poor representation of the summation by integration (see Fig. 4). The standard deviation of the approximate ML estimates is in excellent agreement with the periodogram CRB. This result appears to be general [3], i.e., the standard deviation of mean frequency estimates based on the periodogram or based on estimates of the covariance are bounded by the periodogram CRB if there is no bias from the bad estimates (higher SNR). This class of mean frequency estimators includes the periodogram estimators, auto-regressive estimator (AR), auto-regressive moving average (ARMA), and Minimum Variance or Capon spectral estimator [7].

The source of the error in the high SNR analytic expressions for CRB and Levin's approximation are revealed in Fig. 4 for a very high SNR of 1000. The terms of the Fisher information matrix element J'_{11} with $\varepsilon=0$ [see Eqs. (16), (26), (34), (35)] are compared with Levin's approximation (see Eq. (A.36) of Ref. [26]) and the high-SNR approximation of Zrnic [26]. The high SNR approximation for the integrand is dominated by the largest values of the periodogram index m, i.e., the periodogram coefficients farthest removed from the spectral peak of $P(m)$. This region is the most difficult to represent with analytic approximations to the discrete summation, especially for small spectral width. This error is not reduced as SNR approaches infinity. Levin's approximation to Eq. (26) is also higher and this produces a CRB that is lower than the periodogram CRB but this error results in a good approximation to the exact CRB for much of the parameter space of interest.

C. Cramer-Rao Bound for Signal Power and Spectral Width

Estimators for the signal power and spectral width have been discussed previously ([2], [9], [10], [13], [26], [27]). The exact CRB for estimation of the signal power when spectral width is also estimated is given by

$$\sigma_S^2 \geq \frac{J_{33}}{J_{22}J_{33} - J_{23}^2} \tag{41}$$

The CRB's for estimation of S is shown in Fig. 5 versus normalized spectral width for various SNR. The periodogram CRB is approximately equal to the exact CRB when the maximum periodogram correlation ρ_{max} is small. Levin's approximate CRB is poor for small and large spectral width. For low SNR, the CRB is close to the value unity which is expected for one independent sample of the signal per estimate. For high SNR, the signal power can be more accurately estimated when the spectral width is large. This

reflects the larger number of independent samples available per estimate.

The CRB's are shown in Fig. 6 versus SNR for small and moderate spectral width. The exact CRB decreases with increasing SNR. The periodogram CRB is a poor approximation for the exact CRB for narrow spectral width and high SNR. This is reflected in the high correlation ρ_{max}. The approximate analytic calculations agree at low SNR (a) but not at high SNR (b).

The exact CRB for estimates of the spectral width when signal power is also estimated is given by

$$\sigma_w^2 \geq \frac{J_{11}}{J_{11}J_{33} - J_{13}^2} \tag{42}$$

The CRB's for estimates of spectral width w are shown in Fig. 7 versus normalized spectral width wT_S for various SNR. The ability to estimate spectral width using the periodogram degrades when the spectral width is smaller than the frequency resolution Δf ($wMT_S < 1$). The periodogram CRB agrees with the exact CRB when the maximum correlation ρ_{max} is small. Levin's approximate CRB is less than the exact CRB for small spectral width.

The CRB's for estimates of w are shown in Fig. 8 versus SNR for small and moderate spectral width. The exact CRB decreases with increasing SNR. Again, Zrnic's low SNR limit (a) agrees with the exact CRB at low SNR but Zrnic's high SNR limit (b) is incorrect. The source of the error at high SNR is the failure of the integral approximation for the discrete summation (see Fig. 4). The approximate CRB's for signal power and spectral width are a good approximation to the exact CRB's when $\rho max < 0.01$ for all cases considered.

IV. SUMMARY

Previous results for the exact CRB of the parameters of a complex Gaussian random process are applied to Doppler radar/lidar parameter estimation. A new expression Eq. (15) for the exact CRB for estimation of mean frequency was derived for a complex Gaussian signal in uncorrelated noise. For this model, the CRB's for all the signal parameters are independent of the mean frequency. Approximate CRB's were derived by taking advantage of the fact that the DFT of the data has the same CRB and therefore contains the same information as the original time series. When the DFT coefficients are mutually uncorrelated then so are the periodogram coefficients, and the periodogram CRB is equal to the exact CRB. For this case, the periodogram (or equivalently, the estimates of the covariance) contain the same information as the original time series. The periodogram CRB and Levin's approximate CRB were compared to the exact CRB for estimation of mean frequency, signal power, and spectral width for a signal with a Gaussian covariance function. Levin's approximate CRB is lower than the exact CRB for narrow spectral width. For moderate spectral width and moderate SNR, all the CRB's show good agreement. The performance of an approximate maximum likehood estimate for mean frequency f Eq. (40) using the periodogram and assuming knowledge of the spectral width approaches the exact CRB for moderate SNR and moderate spectral width. The role of the CRB for low SNR is complicated because all estimates for mean frequency are biased due to the uniformly distributed "bad" estimates (See Fig. 1 and Ref. [3]). The periodogram CRB appears to be a lower bound for the unbiased spectral domain estimates of the mean frequency [3] (periodogram, maximum entropy, auto-regressive, auto-regressive moving average, minimum variance spectral estimator (Capon) [7]). For narrow spectral width and high SNR, more than a factor of two improvement in mean-frequency accuracy is indicated by the CRB [see Fig. 2]. This improvement can be realized with the Maximum Likelihood estimator [3]. The calculation of the periodogram CRB and the maximum correlation coefficient ρ_{max} can be efficiently performed using the FFT algorithm. Previous analytic high SNR limits for exact CRB's were shown to be inaccurate because the discrete summations cannot be accurately approximated by integration (see Fig. 4).

ACKNOWLEDGEMENT

The author acknowledges useful discussions with M. J. Kavaya, D. S. Zrnic, and B. J. Rye. This work was supported by the National Research Council, the National Science Foundation, and the National Aeronautics and Space Administration. The suggestions of anonymous reviewers are also acknowledged.

REFERENCES

1 R. Bamler, "Doppler frequency estimation and the Cramer-Rao bound," *IEEE Trans. Geo. Remote Sensing*, vol. 29, pp. 385-390, 1991.

2 R. J. Doviak, and D. S. Zrnic, *Doppler radar and weather observations*, Academic Press, 1984.; second edition 1993.

3 R. G. Frehlich, and M. J. Yadlowsky, "Performance of mean frequency estimators for Doppler Radar/Lidar," submitted to J. Atm. Ocean. Tech., (1993).

4 R. M. Hardesty, "Performance of a discrete spectral peak frequency estimator for Doppler wind velocity measurements," *IEEE Trans. Geosci. Remote Sensing, ,* vol. GE-24, pp. 777-783, 1986.

5 W. K. Hocking, "On the extraction of atmospheric turbulence parameters from radar backscatter Doppler spectra- I. Theory," *J. Atmos. Terr. Phys., 45, pp. 89-102, 1983.*

6 Y. M. Jin, "Optimal Doppler centroid estimation for SAR data from a quasi-homogeneous source," *IEEE Trans. Geo. Sci. Remote Sensing*, vol. GE-24, pp. 1022-1025, 1986.

7 S. M. Kay and S. L. Marple, Jr., "Spectrum analysis- A modern perspective," *Proc. IEEE*, vol. 69, pp. 1380-1419, 1981.

8 J. Klostermeyer, "Experiments with maximum entropy and maximum likelihood spectra of VHF radar signals" Radio Science, vol. 21, pp. 731-736, 1986.

9 J. Klostermeyer, "Maximum entropy estimation of Doppler shift and spectral width of VHF radar signals" Radio Science, vol. 24, pp. 47-63, 1989.

10 J. M. Levin, "Power spectrum parameter estimation," *IEEE Trans. Information Theory*, vol. IT-11, pp. 100-107, 1965.

11 P. R. Mahapatra, and D. S. Zrnic, "Practical algorithms for mean velocity estimation in pulse Doppler weather radars using a small number of samples," *IEEE Trans. Geosci. Electronics*, vol. GE-21, pp. 491-501, 1983.

12 P. T. May and R. G. Strauch, "An examination of Wind Profiler signal processing algorithms," *L. Atmos. Oceanic Tech.*, vol. 6, pp. 731-735, 1989.

13 P. T. May, T. Sato, M. Yamamoto, S. Kato, T. Tsuda, and S. Fukao, "Errors in the determination of wind speed by Doppler radar," *L. Atmos. Oceanic Tech.*, vol. 6, pp. 235-242, 1989.

14 R. D. Palmer, J. R. Cruz, and D. S. Zrnic, "Enhanced autoregressive moving average spectral estimation applied to the measurement of Doppler spectral width," *IEEE Trans. Geosci. Electronics*, vol. GE-29, pp. 358-368, 1991.

15 B. Porat, and B. Friedlander, "Computation of the exact information matrix of Gaussian time series with stationary random components," *IEEE Trans. Acoust. Speech Signal Processing*, vol. ASsp-34, pp. 118-130, 1986.

16 B. Porat, and B. Friedlander, "The exact Cramer-Rao bound for Gaussian autoregressive processes," *IEEE Trans. Aero. Electr. Sys.*, vol. AES-23, pp. 537-541, 1987.

17 B. J. Rye and R. M. Hardesty, "Discrete spectral peak estimation in incoherent backscatter heterodyne lidar. I. Spectral accumulation and the Cramer-Rao lower bound," *IEEE Trans. Geo. Sci. Remote Sensing*, vol.31, pp.16-27, 1993.

18 B. J. Rye and R. M. Hardesty, "Discrete spectral peak estimation in incoherent backscatter heterodyne lidar. II. Correlogram accumulation," *IEEE Trans. Geo. Sci. Remote Sensing*, vol.31, pp.28-35, 1993.

19 P. M. Schultheiss, E. Ashok, and J. P. Ianniello, "Optimum and sub-optimum source localization with sensors subject to random motion," *J. Acoust. Soc. Am.*, vol. 74, pp. 131-142, 1983.

20 H. L. Van Trees, *Detection, Estimation, and Modulation Theory, Part I*, John Wiley and Sons, Inc., 1968.

21 P. Whittle, "The analysis of multiple stationary time series," *J. Roy. Statist. Soc.*, vol. 15, pp. 125-139, 1953.

22 R. F. Woodman, "Spectral moment estimation in MST radars," *Radio Sci.*, vol. 20, pp. 1185-1195, 1985.

23 D. S. Zrnic, "Simulation of weatherlike Doppler spectra and signals," *J. Appl. Meteor.*, vol. 14, pp. 619-620, 1975.

24 D. S. Zrnic, "Spectral moment estimates from correlated pulse pairs" IEEE Trans. Ant. Prop., vol. AP-23, pp. 344-354, 1975.

25 D. S. Zrnic, and R. J. Doviak, "Matched filter criteria and range weighting for weather radar," *IEEE Trans. AES*, vol. AES-14, pp. 925-930, 1978.

26 D. S. Zrnic, "Estimation of spectral moments of weather echoes," *IEEE Trans. Geosci. Electronics*, vol. GE-17, pp. 113-128, 1979.

27 D. S. Zrnic, "Spectral width estimates of weather echoes," *IEEE Trans. AES*, vol. AES-15, pp. 613-619, 1979.

28 D. S. Zrnic, "Spectral statistics for complex colored discrete-time sequences," *IEEE Trans. ASSP*, vol. 28, pp. 596-599, 1980.

29 D. W. Rice, and K. H. Wu, "Quadrature sampling with high dynamic range," *IEEE Trans. Aer. Electr. Sys.*, vol. AES-18, pp. 736-739, 1982.

30 C. M. Rader, "A simple method for sampling in-phase and quadrature components," *IEEE Trans. Aer. Electron. Sys.*, vol. AES-20, pp. 821-824, 1984.

31 C. W. Helstrom, *Statistical theory of signal detection*, Pergamon Press, 1968.

32 L. L. Scharf, *Statistical signal processing*, Addison-Wesley, 1991.

33 N. R. Goodman, "Statistical analysis based on a certain multivariate complex Gaussian distribution (an introduction)," *Ann. Math. Stat.*, vol. 34, pp. 152-177, 1964.

34 R. G. Frehlich, "Cramer Rao Bound for Doppler Lidar parameter estimation," NASA Memo.

35 G. H. Golub and C. F. Van Loan *Matrix computations*, John Hopkins University Press, 1989, p. 189.

FIGURE CAPTIONS

Fig. 1 Probability Density Functions (PDF) (•) from 10000 approximate Maximum Likelihood estimates of mean frequency f Eq. (40) for a SNR=0.1 and two different spectral widths. The best fit theoretical model is indicated by (___).

Fig. 2 CRB for mean frequency f vs normalized spectral width for SNR of 0.1,1, and 10 and M=128 data points. Exact CRB [Eqs. (16), (11), and (30)] (____), periodogram CRB (....), Levin's CRB (- - -), and maximum periodogram correlation ρ_{max} (. _ . _). The performance of the approximate maximum likelihood estimator Eq. (40) is indicated by O.

Fig. 3 CRB for mean frequency f vs SNR for normalized spectral widths of 0.01 and 0.05 and M=128 data points. Exact CRB [Eqs. (16), (11), and (30)] (____), periodogram CRB (....), Levin's CRB (- - -), Zrnic's low SNR limit Eq. (38) a, Zrnic's high SNR limit Eq. (37) b, and maximum periodogram correlation ρ_{max} (. _ . _). The performance of the approximate maximum likelihood estimator Eq. (40) is indicated by O.

Fig. 4 Integrand for approximate CRB's for mean frequency f vs periodogram index m for an SNR=1000, M=128 data points, and normalized spectral widths of 0.1 and 0.05. The elements of the discrete summation for the Fisher information matrix element J'_{11} Eq. (26) with Eqs. (34), (35), and m_F=0 are indicated by (____), Zrnic's analytic approximation for Levin's CRB [Ref. [26], Eq. (A.36) is (....), Zrnic's high SNR approximation [26] is (_ _ _), and the average periodogram Eq. (34) is marked as $P(m)$.

Fig. 5 The exact CRB for signal power [Eqs. (41), (11), and (30)] (____), the periodogram CRB (....), Levin's CRB (- - -), and the maximum periodogram correlation ρ_{max} (. _ . _) vs normalized spectral width wT_S.

Fig. 6 The exact CRB for signal power [Eqs. (41), (11), and (30)] (____), the periodogram CRB (....), and Levin's CRB (- - -), vs SNR for normalized spectral widths of 0.01 and 0.05 and M=128 data points. Zrnic's [Ref. [26], Eq. (A.40)] low SNR limit a, and Zrnic's [Ref. [26], Eq. (A.38)] high SNR limit b. The maximum periodogram correlation ρ_{max} is (. _ . _).

Fig. 7 The exact CRB for spectral width [Eqs. (42), (11), and (30)] (____), the periodogram CRB (....), Levin's CRB (- - -), and the maximum periodogram correlation ρ_{max} (. _ . _) vs normalized spectral width wT_S for various SNR and M=128 data points.

Fig. 8 The exact CRB for spectral width [Eqs. (42), (11), and (30)] (____), he periodogram CRB (....), Levin's CRB (- - -), and the maximum periodogram correlation ρ_{max} (. _ . _) vs SNR for normalized spectral widths of 0.01 and 0.05 and M=128 data points. Zrnic's [Ref. [26], Eq. (A.41)] low SNR limit a, and Zrnic's [Ref. [26], Eq. (A.39)] high SNR limit b.

Figure 1 MS 92-154 Frehlich

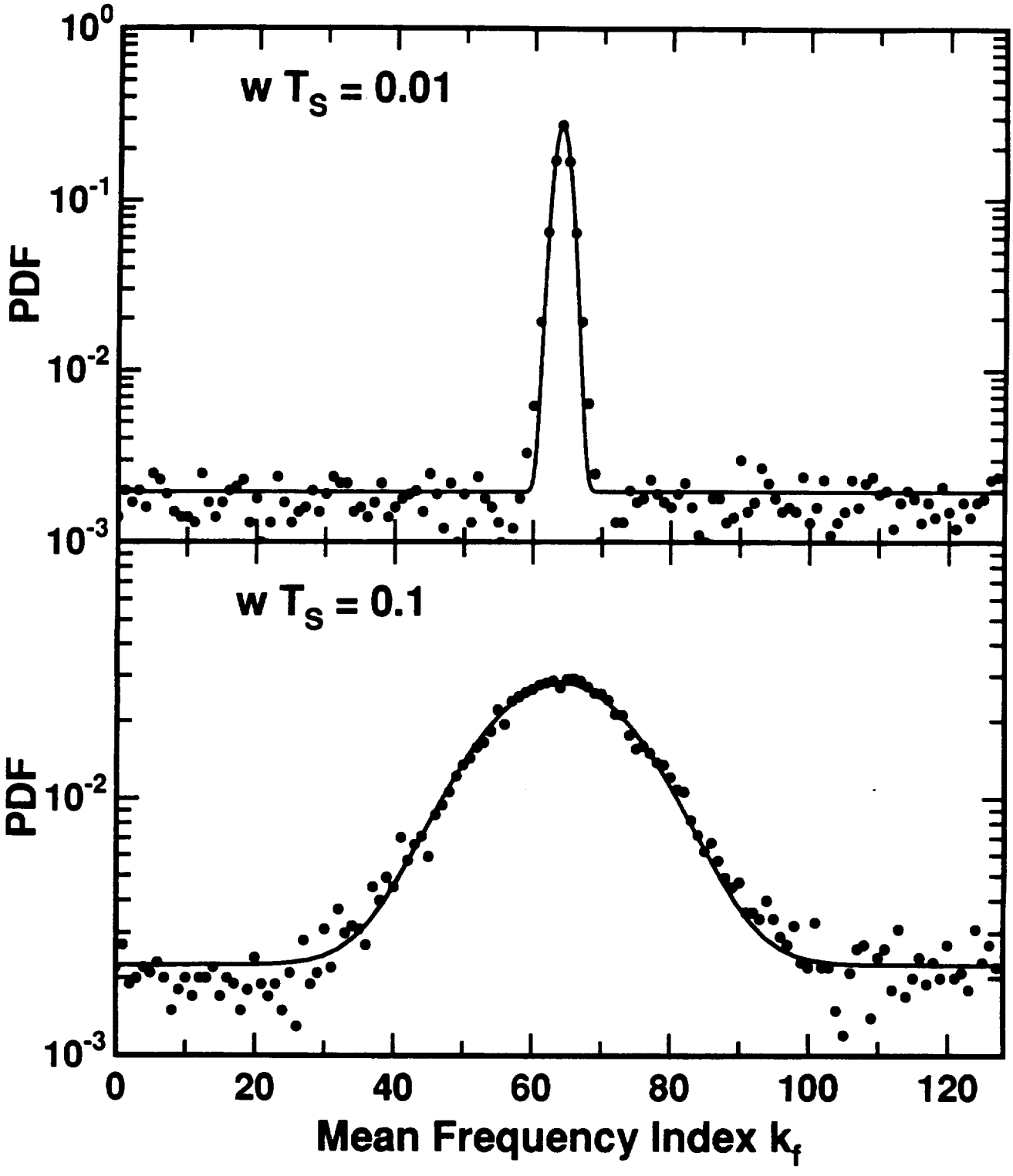

Figure 2 MS 92-154 Frehlich

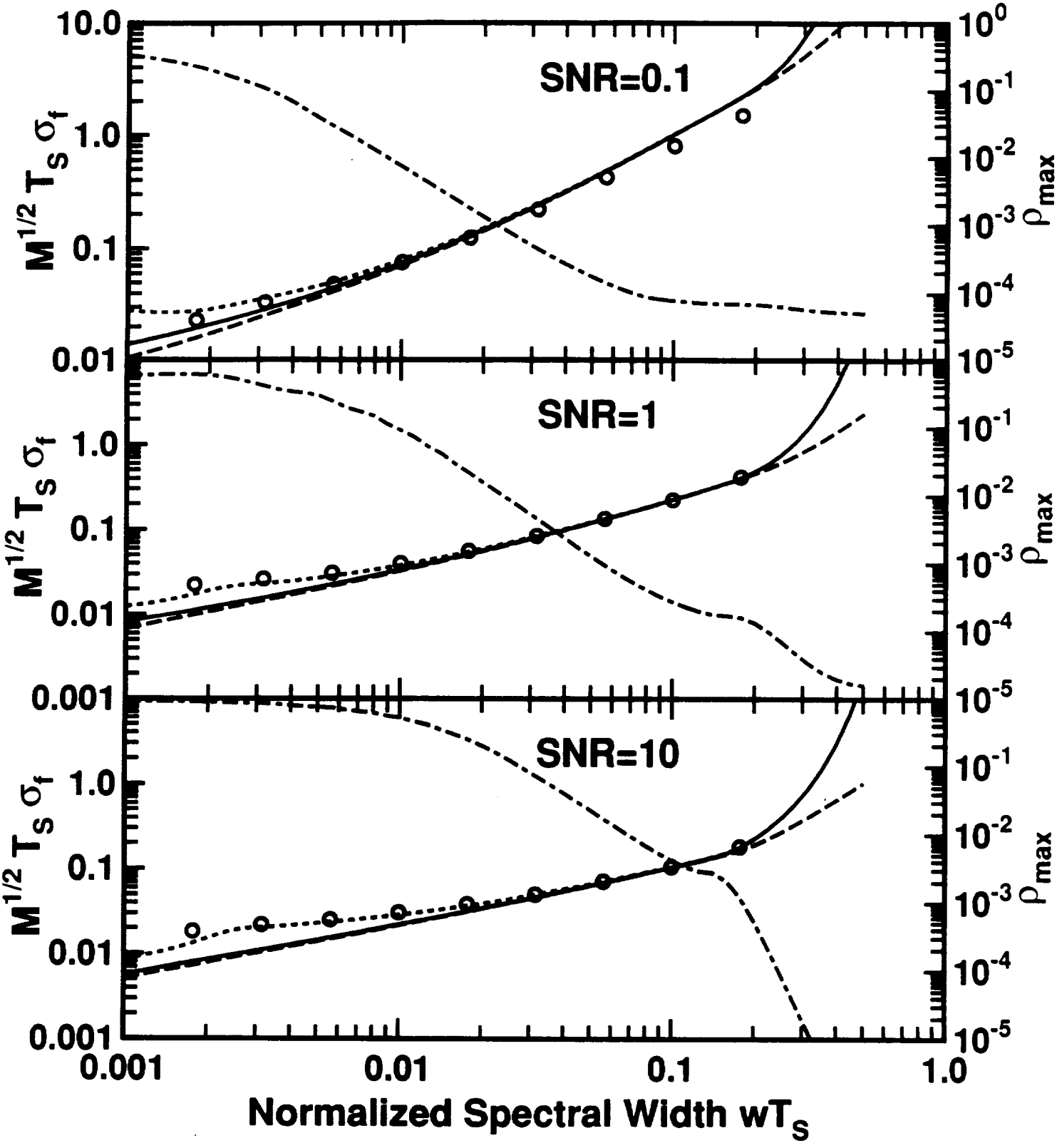

Figure 3 MS 92-154 Frehlich

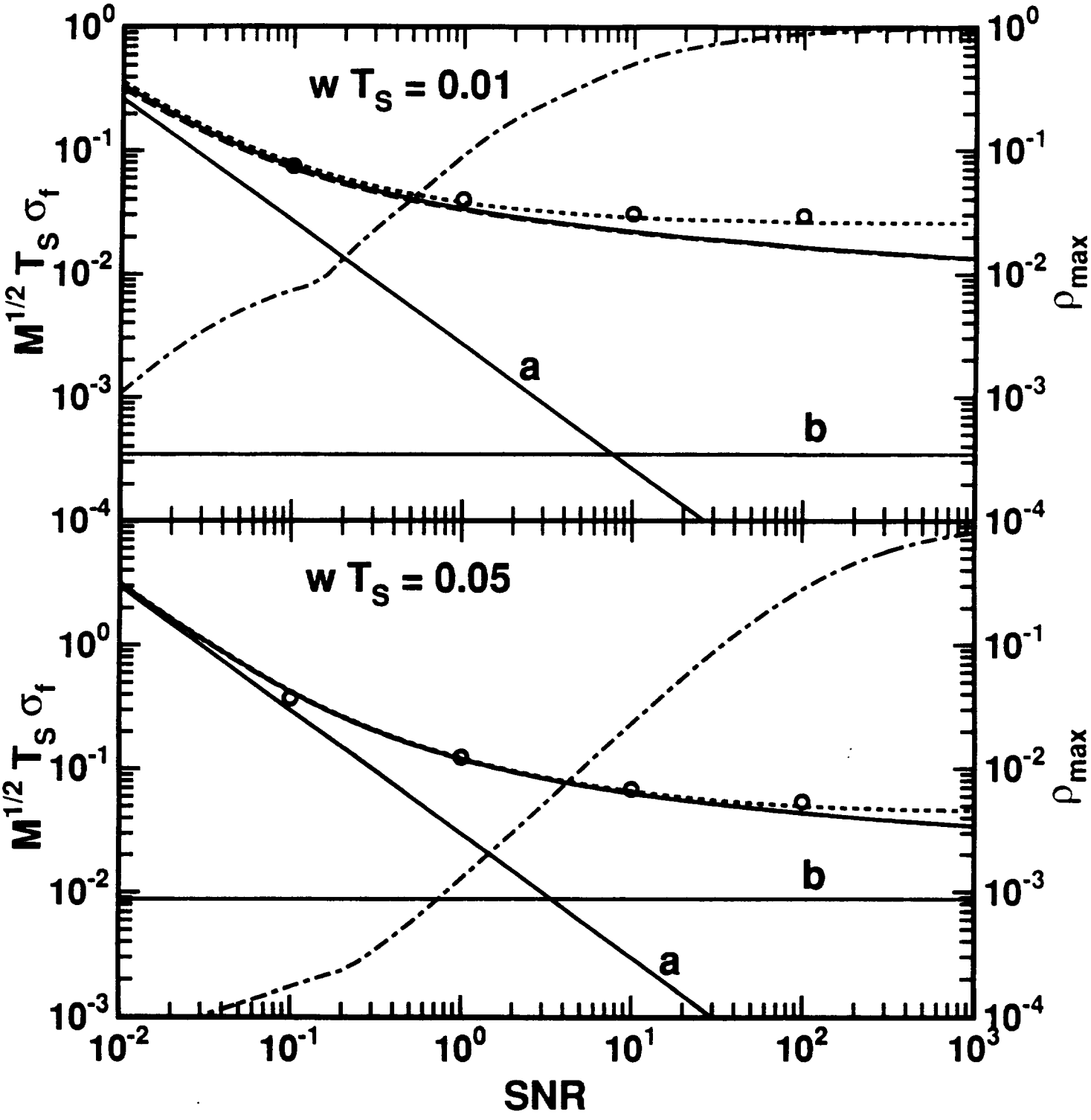

Figure 4 MS 92-154 Frehlich

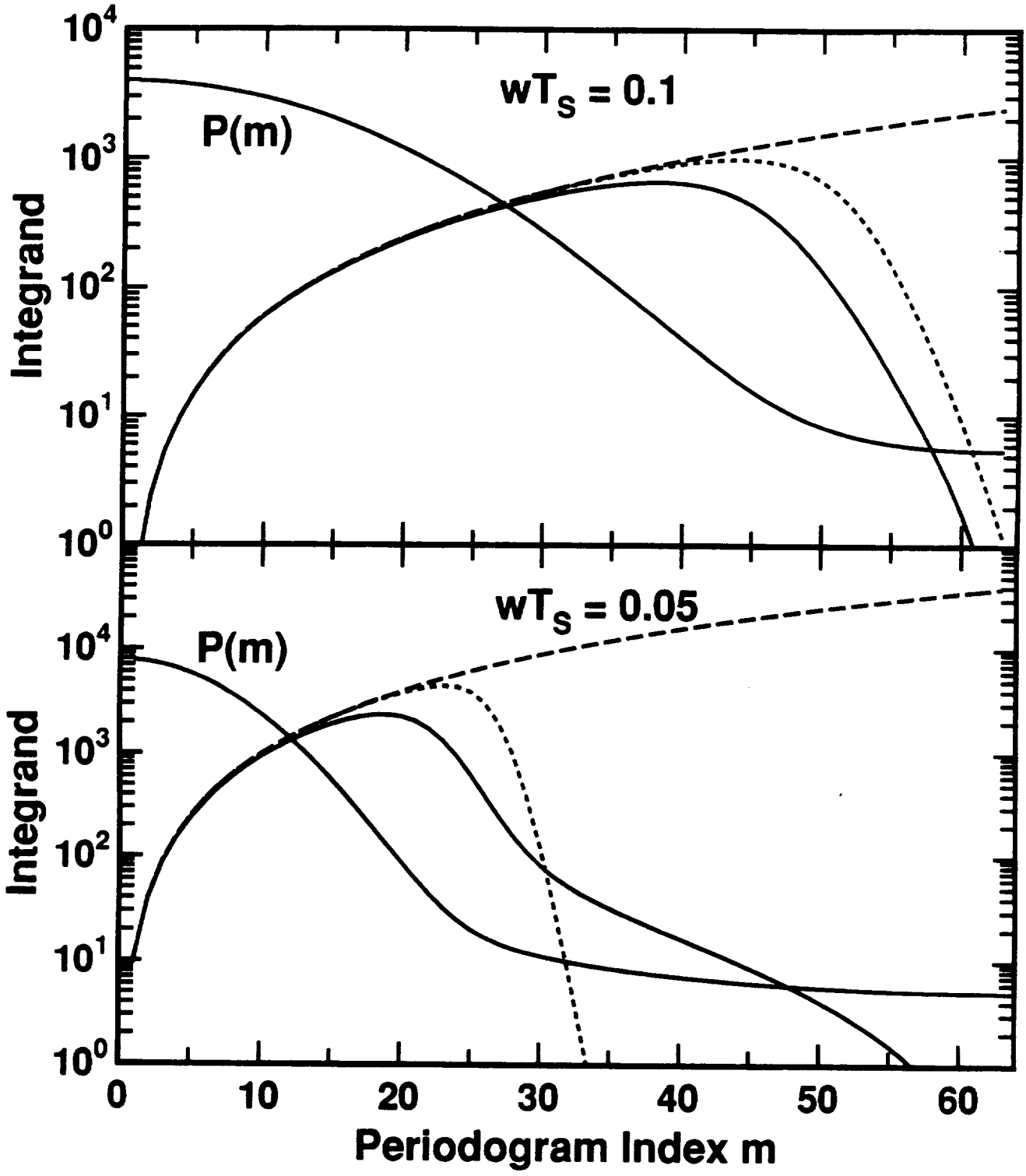

Figure 5 MS 92-154 Frehlich

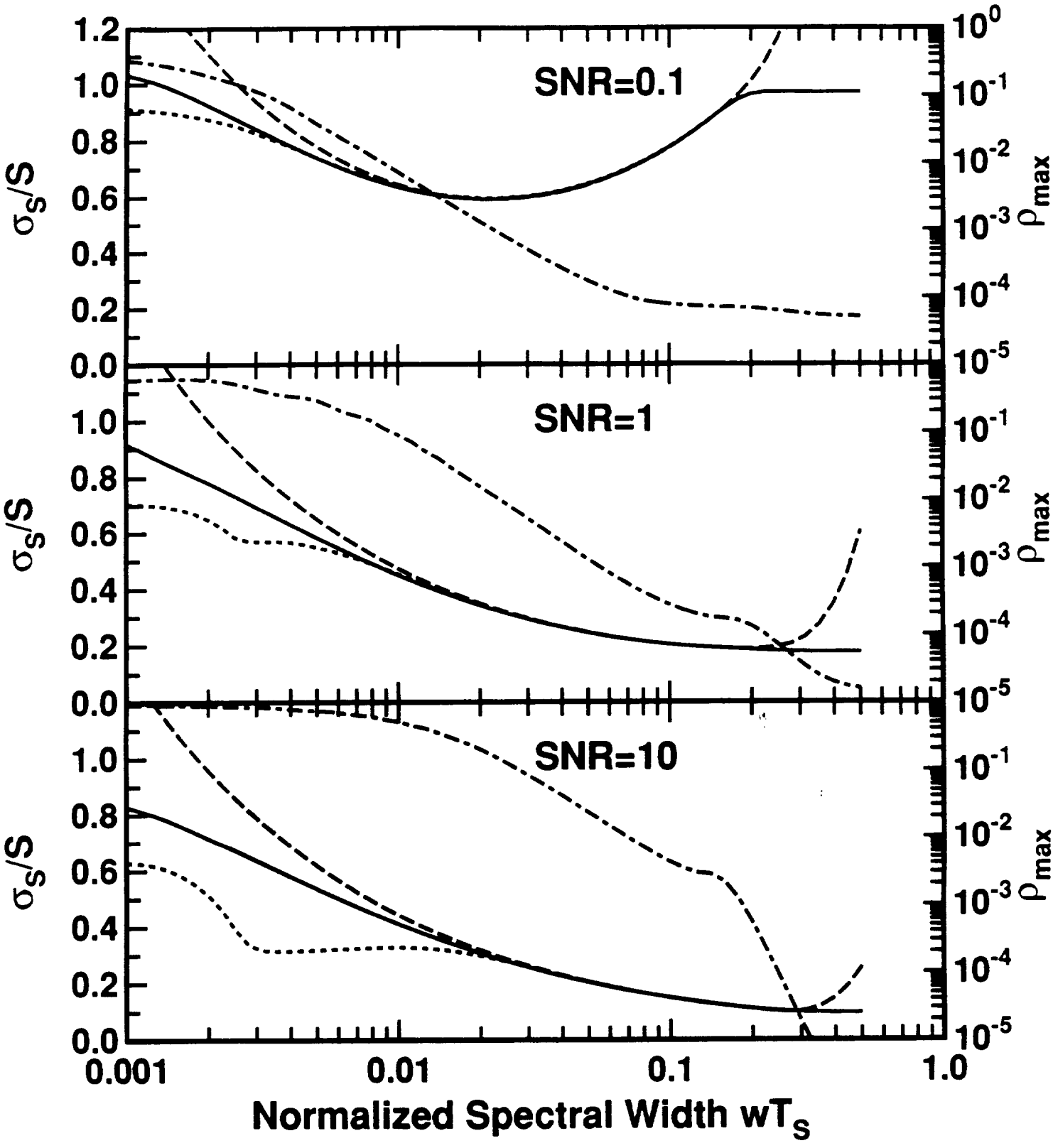

Figure 6 MS 92-154 Frehlich

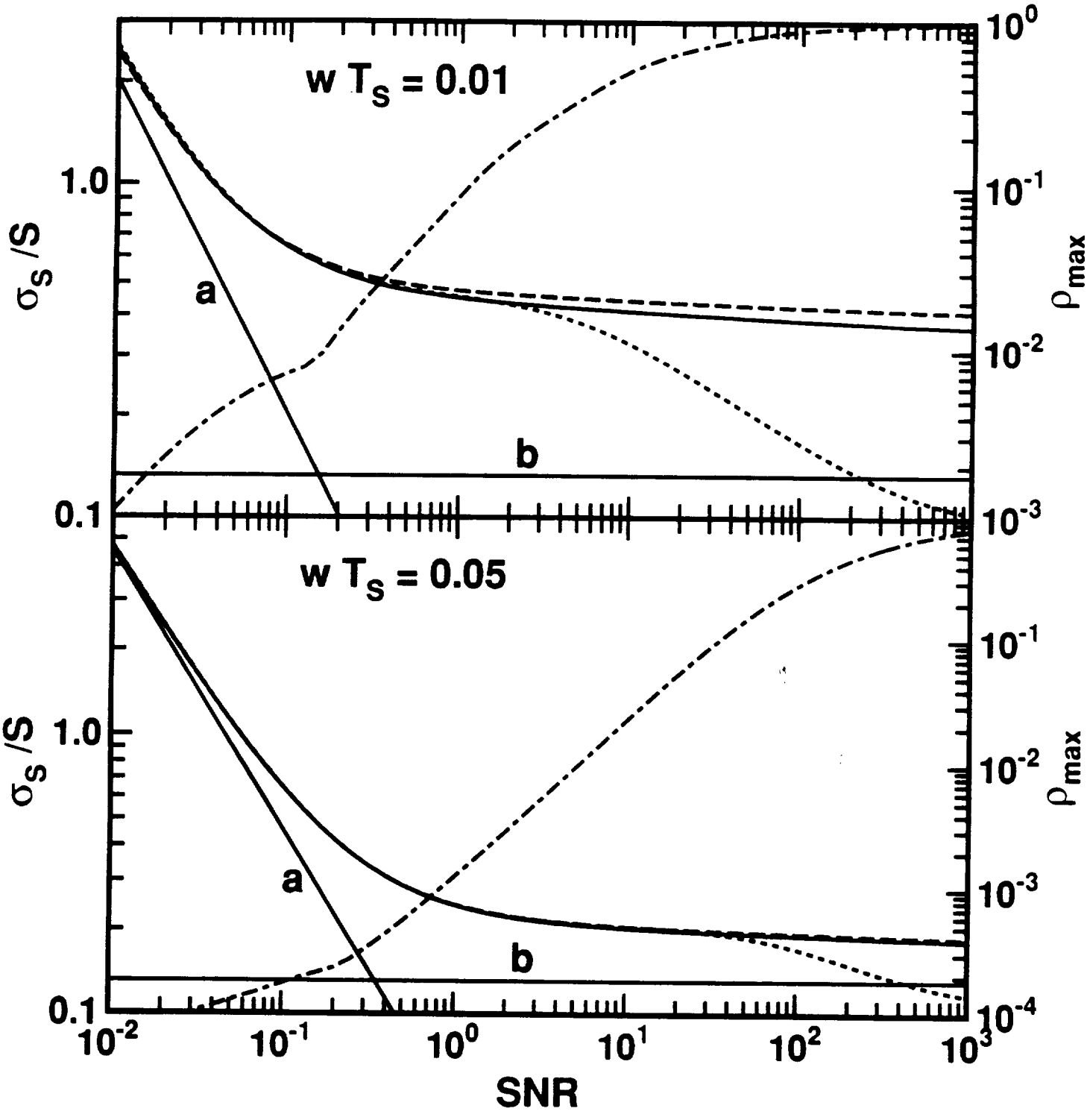

Figure 7 MS 92-154 Frehlich

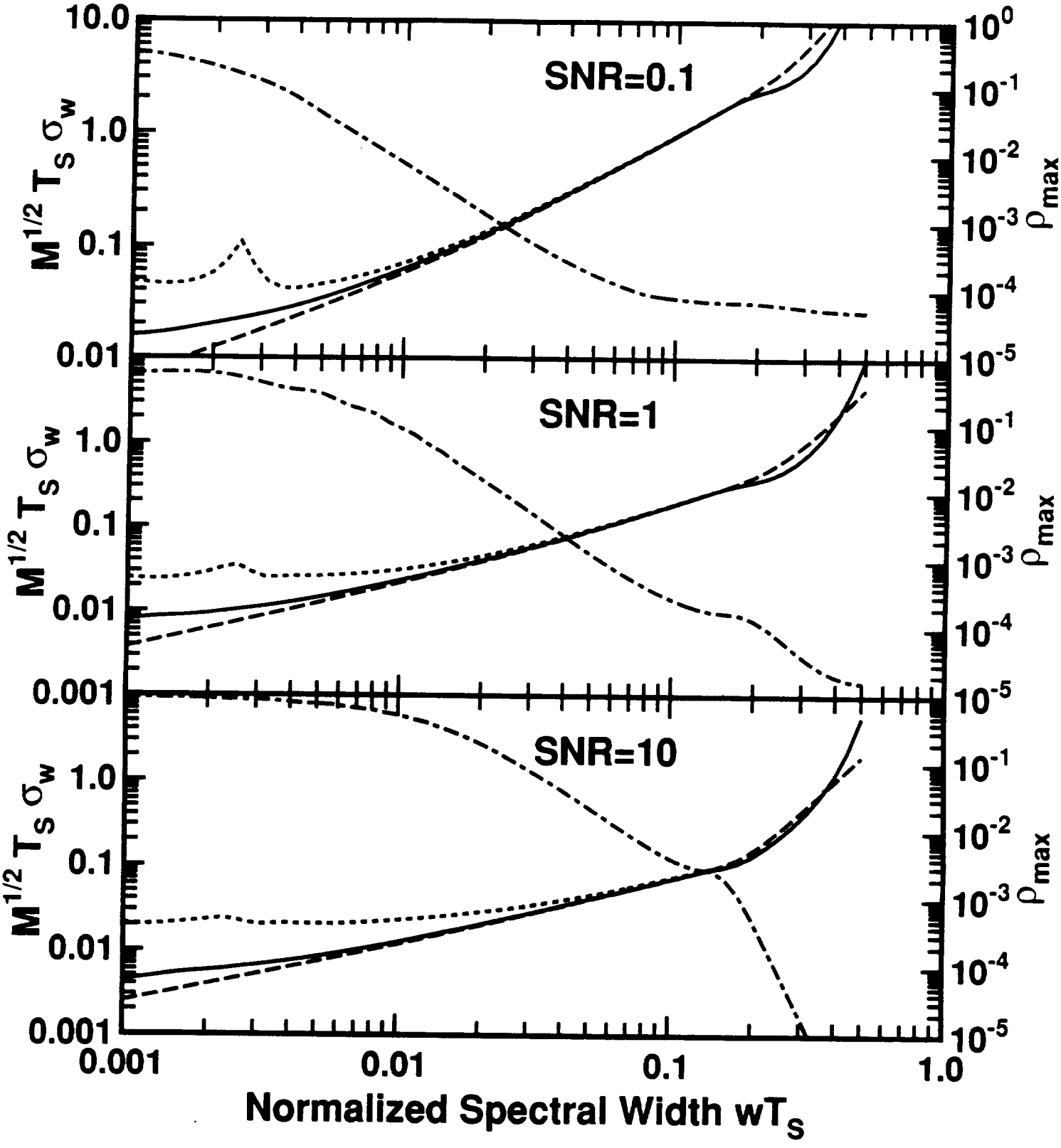

Figure 8 MS 92-154 Frehlich

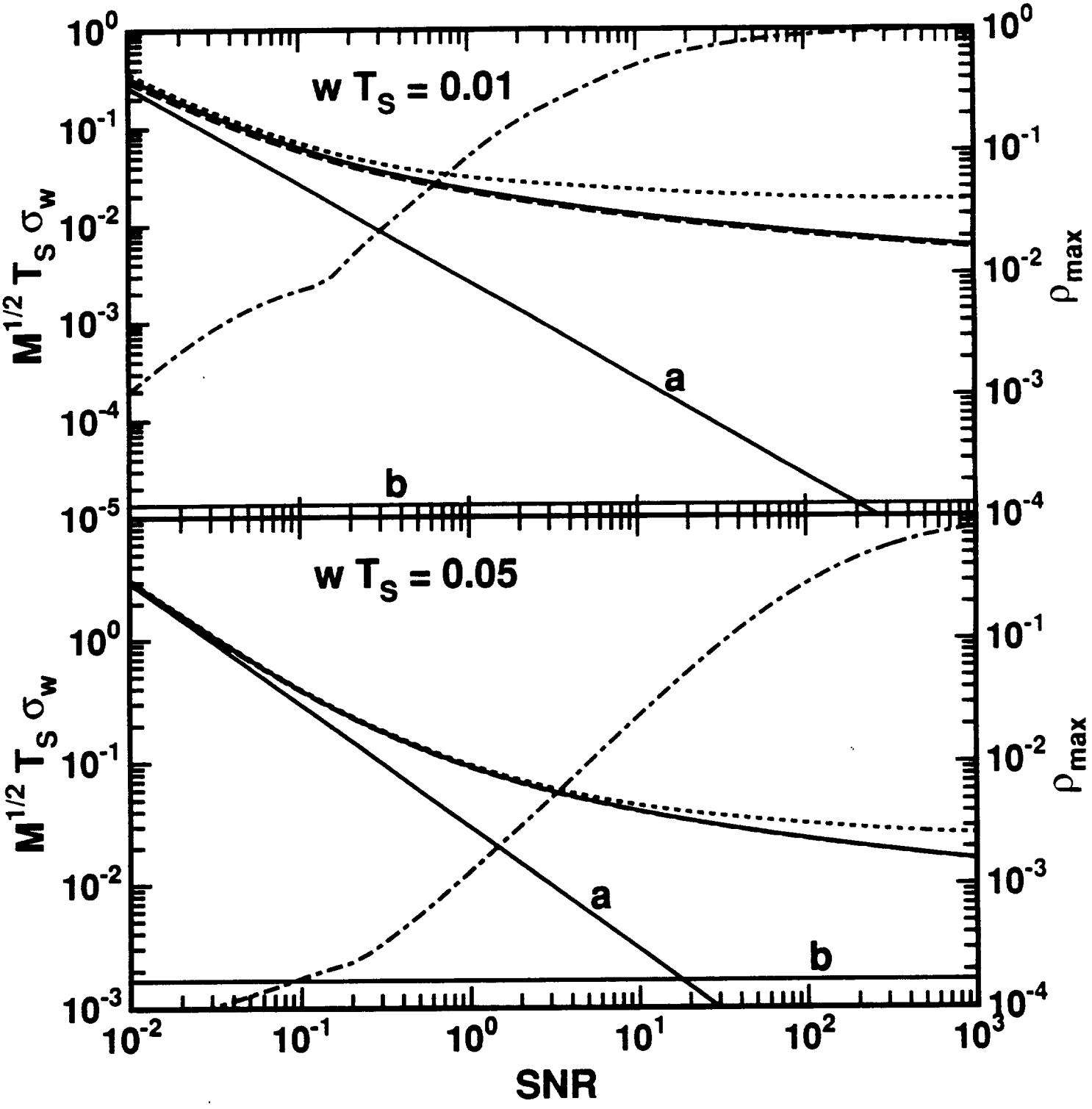

Heterodyne Efficiency for a Coherent Laser Radar with Diffuse or Aerosol Targets

R. G. Frehlich

Cooperative Institute for Research in the Environmental Sciences (CIRES)
University of Colorado, Boulder, CO 80309

Abstract

The performance of a Coherent Laser Radar is determined by the statistics of the coherent Doppler signal. The heterodyne efficiency is a excellent indication of performance because it is an absolute measure of beam alignment and is independent of the transmitter power, the target backscatter coefficient, the atmospheric attenuation, and the detector quantum efficiency and gain. The theoretical calculation of heterodyne efficiency for an optimal monostatic lidar with a circular aperture and Gaussian transmit laser is presented including beam misalignment in the far-field and near-field regimes. The statistical behavior of estimates of the heterodyne efficiency using a calibration hard target are considered. For space based applications, a biased estimate of heterodyne efficiency is proposed that removes the variability due to the random surface return but retains the sensitivity to misalignment. Physical insight is provided by simulation of the fields on the detector surface. The required detector calibration is also discussed.

Key words: Lidar, Laser Radar, Remote Sensing.

1. Introduction

An important measure of the performance of coherent laser radar (CLR) is the Signal-to-Noise Ratio (SNR) defined by [1]

$$SNR(t) = \frac{\langle i_S^2(t) \rangle}{\langle i_N^2 \rangle} \tag{1}$$

where $\langle\rangle$ denotes ensemble average, $\langle i_S^2(t) \rangle [A^2]$ is the average coherent power at time $t[s]$, and $\langle i_N^2(t) \rangle [A^2]$ is the average noise power. For an infinite diffuse target at range $R[m]$ with uniform backscatter coefficient ρ, detector noise dominated by Local Oscillator (LO) shot noise, a detector with uniform quantum efficiency η_Q that collects all the energy of the LO beam, the CLR SNR is given by [1, 2]

$$SNR(R) = \frac{\eta_Q P_L \rho K^2}{h\nu B} C(R) \tag{2}$$

where $P_L[W]$ is the transmitted laser power, $h[Js]$ is Plancks constant, $\nu[s^{-1}]$ is the frequency of the laser, $B[s^{-1}]$ is the signal bandwidth of the detector, K is the one-way atmospheric

attenuation, and $C(R)$ is the coherent responsivity. For an aerosol target, similar expressions are obtained [Ref. [1], Eqs. (89), (92)]. When the effects of atmospheric refractive turbulence are negligible

$$C(R) = A_R T_T \eta_H(R)/R^2 \tag{3}$$

where $A_R[m^2]$ is the area of the telescope aperture, T_T is the fraction of the laser power transmitted through the telescope aperture, and $\eta_H(R)$ is the heterodyne efficiency. Heterodyne efficiency is unity when the backscattered field is proportional to the LO field on the detector surface. Heterodyne efficiency is a useful measure of performance for a CLR because it is independent of the transmitter power, the backscatter coefficient, the detector quantum efficiency, and the atmospheric attenuation. The heterodyne efficiency can also be estimated from the detector signal [1], i.e.,

$$\eta_H(t) = \frac{\langle i_S^2(t)\rangle}{2\langle I_{DC}\rangle\langle I_S(t)\rangle} \tag{4}$$

where $I_{DC}[A]$ is the direct current (DC) due to the LO, $i_S(t)[A]$ is the intermediate frequency (IF) signal current or coherent signal, and $I_S(t)[A]$ is the direct detection signal current due to the backscattered field [Note the typo in Ref. [1], Eq. (15)]. For diffuse and aerosol targets, the backscattered field at the receiver is spatially random and described by "speckle" statistics, i.e., the complex field has a zero-mean joint Gaussian probability density function (PDF). The statistical behavior of estimates for the heterodyne efficiency will be investigated with theoretical calculations and numerical simulations.

2. Theory

The analysis of heterodyne efficiency is presented using the normalized direct detection power

$$d = I_S/\langle I_S\rangle \tag{5}$$

and the normalized coherent detection power

$$c = \frac{i_S^2}{2\langle I_{DC}\rangle\langle I_S\rangle} \tag{6}$$

Then $\langle d\rangle = 1$ and $\langle c\rangle = \eta_H$.

The heterodyne efficiency depends on the CLR design, which can be represented by [1] the transmitter aperture function $W_T(\vec{u})$, the normalized transmitter laser field incident on the transmitter aperture $e_L(\vec{u},0)[m^{-1}]$, the receiver aperture function $W_R(\vec{v})$, and the normalized Local Oscillator (LO) field at the receiver aperture $e_{LO}(\vec{v},0)[m^{-1}]$. Here, $\vec{u}[m]$ and $\vec{v}[m]$ denote the two-dimensional transverse vector for the transmitter aperture and receiver aperture, respectively.

We will consider a monostatic CLR $[W_T(\vec{u}) = W_R(\vec{u}) = W(\vec{u})]$ with a circular telescope aperture of radius $a[m]$, i.e.,

$$W(\vec{u}) = 1 \qquad |u| \leq a$$
$$= 0 \qquad |u| > a \tag{7}$$

and

$$A_R = \int_{-\infty}^{\infty} |W(\vec{v})|^2 d\vec{v} = \pi a^2 = \pi D^2/4 \tag{8}$$

where $D[m]$ is the diameter of the aperture.

The heterodyne efficiency can be written as [1]

$$\eta_H(R) = \frac{R^2\lambda^2}{A_R T_T} \int_{-\infty}^{\infty} j_T(\vec{p}, R) j_{BPLO}(\vec{p}, R) d\vec{p} \tag{9}$$

where

$$j_T(\vec{p}, R) = |e_T(\vec{p}, R)|^2 \tag{10}$$

$$j_{BPLO}(\vec{p}, R) = |e_{BPLO}(\vec{p}, R)|^2 \tag{11}$$

are the irradiance $[m^{-2}]$ of the normalized transmitter and Back Propagated Local Oscillator (BPLO) field, respectively. Here,

$$e_T(\vec{p}, R) = \int_{-\infty}^{\infty} e_T(\vec{u}, 0) G(\vec{p}; \vec{u}, R) d\vec{u} \tag{12}$$

is the normalized transmitter field at the target coordinate $(\vec{p}, R)$ $[m]$,

$$e_T(\vec{u}, 0) = e_L(\vec{u}, 0) W(\vec{u}) \tag{13}$$

is the normalized transmitter field at the telescope aperture,

$$e_{BPLO}(\vec{p}, R) = \int_{-\infty}^{\infty} e_{BPLO}(\vec{v}, 0) G(\vec{p}; \vec{v}, R) d\vec{v} \tag{14}$$

is the normalized BPLO field at the target,

$$e_{BPLO}(\vec{v}, 0) = e_L^*(\vec{v}, 0) W(\vec{v}) \tag{15}$$

is the normalized BPLO field at the receiver aperture,

$$G(\vec{p}; \vec{u}, R) = \frac{k}{2\pi i R} \exp\left[\frac{ik}{2R}(\vec{p} - \vec{u})^2\right] \tag{16}$$

is the free space Green's function $[m^{-2}]$ for propagating the scalar fields from the transmitter-receiver plane to the target plane under the Fresnel approximation where $k[m^{-1}] = 2\pi/\lambda$ is the wavenumber of the transmitter field, and $\lambda[m]$ is the wavelength of the field.

The integrated normalized irradiance

$$\int_{-\infty}^{\infty} j_T(\vec{p}, R) d\vec{p} = T_T \tag{17}$$

is equal to the power transmittance T_T of the laser through the transmitter-receiver aperture. Similarly,

$$\int_{-\infty}^{\infty} j_{BPLO}(\vec{\mathbf{p}}, R) d\vec{\mathbf{p}} = T_R \tag{18}$$

is equal to the power transmittance T_R of the BPLO field through the transmitter-receiver aperture.

A Gaussian spatial distribution is the most common laser transmitter field, i.e.,

$$e_L(\vec{\mathbf{u}}, 0) = (2\pi\sigma_L^2)^{-1/2} \exp\left(-\frac{u^2}{2\sigma_L^2} - \frac{iku^2}{2F_L^2}\right) \tag{19}$$

where σ_L [m] is the 1/e intensity radius of the beam at the transmitter aperture, and $F_L[m]$ is the radius of curvature of the phase front. The irradiance at the target is given by [substitute Eqs. (13) and (19) into (12), convert to polar coordinates and integrate over angle]

$$j_T(\vec{\mathbf{p}}, R) = \frac{\delta_{RF}^2}{\pi\sigma_L^2} |Y(\Omega_T^2, kpa/R)|^2 \tag{20}$$

where

$$\Omega_T^2 = \delta_T^2 - i\delta_{RF}^2(1 - R/F_L) \tag{21}$$

$$\delta_T = a/\sigma_L \ , \ \delta_{RF} = a/R_F \ , \ R_F = (R/k)^{1/2} \tag{22}$$

$$Y(\Omega, q) = \int_0^1 \exp(-x^2\Omega^2/2) J_0(qx) x dx \tag{23}$$

An efficient series expansion for $Y(\Omega, q)$ is [3]

$$\begin{aligned} Y(\Omega, q) &= \Omega^{-2}\left[\exp\left(-\frac{q^2}{2\Omega^2}\right) - \exp\left(-\frac{\Omega^2}{2}\right)\sum_{n=0}^{\infty}\left(\frac{-q}{\Omega^2}\right)^n J_n(q)\right] \quad q < |\Omega^2| \\ &= \Omega^{-2}\exp(-\Omega^2/2)\sum_{n=1}^{\infty}\left(\frac{\Omega^2}{q}\right)^n J_n(q) \qquad\qquad q > |\Omega^2| \end{aligned} \tag{24}$$

The far-field result is produced when $\Omega_T^2 = \delta_T^2$, which occurs when $R = F_L$ (focused condition). For a collimated beam ($F_L = \infty$), the far-field condition is $\delta_T >> \delta_{RF}$ or $R_F >> \sigma_L$.

A Gaussian field focused on the detector is a common choice for the LO field. The receiver-plane representation of the LO field is

$$e_{LO}(\vec{\mathbf{v}}, 0) = (2\pi\sigma_{LO}^2)^{-1/2} \exp\left(-\frac{v^2}{2\sigma_{LO}^2} + \frac{ikv^2}{2F_{LO}^2}\right) \tag{25}$$

and

$$j_{BPLO}(\vec{\mathbf{p}}, R) = \frac{\delta_{RF}^2}{\pi\sigma_{LO}^2} |Y(\Omega_R^2, kpa/R)|^2 \tag{26}$$

where

$$\Omega_R^2 = \delta_R^2 - i\delta_{RF}^2(1 - R/F_{LO}) \ , \quad \delta_R = a/\sigma_{LO} \tag{27}$$

In practice, it is difficult to perfectly align the LO field with the backscattered field. The misalignment angle $\Delta\theta[rad]$ produces an offset $\Delta p = R\Delta\theta[m]$ between the two irradiance distributions in the target plane. (The effects of refractive turbulence on beam misalignment for Gaussian beams and a Gaussian aperture were investigated by Frehlich [4]). For this CLR, the heterodyne efficiency including misalignment is given by

$$\eta_H(R) = \frac{4\delta_T^2\delta_R^2}{\pi T_T} Q(\Omega_T, \Omega_R, \Delta q) \tag{28}$$

where

$$Q(\Omega_T, \Omega_R, \Delta q) = \int_{-\infty}^{\infty} |Y(\Omega_T, \vec{\mathbf{q}})|^2 |Y(\Omega_R, \vec{\mathbf{q}} - \Delta\vec{\mathbf{q}})|^2 d\vec{\mathbf{q}} \tag{29}$$

is the overlap integral of the normalized transmitter irradiance $|Y(\Omega_T, \vec{\mathbf{q}})|^2$ and BPLO irradiance $|Y(\Omega_R, \vec{\mathbf{q}} - \Delta\vec{\mathbf{q}})|^2$ and

$$\Delta q = \pi D\Delta\theta/\lambda \tag{30}$$

is the normalized angle-misalignment.

Wang [5] calculated the optimal parameters for a Gaussian transmit beam and a Gaussian LO beam focused on the detector for the far-field condition [$\delta_T = \delta_R = 1.7633$, $\eta_H = 0.41992$, $T_T = T_R = 1 - \exp(-\delta_T^2) = 0.95536$]. Rye [6] proposed an optimal design where the BPLO beam does not have any truncation by the telescope aperture, i.e., $T_R = 1$. For this design

$$\eta_H(R) = \frac{4\delta_T^2\delta_R^2}{\pi T_T[1 - \exp(-\delta_R^2)]} Q(\Omega_T, \Omega_R, \Delta q) \tag{31}$$

and for a Gaussian LO beam, the optimal parameters are $\delta_T = 1.7367$, $T_T = 1 - \exp(-\delta_T^2) = 0.95101$, $\delta_R = 1.1931$, $\eta_H = 0.460958$. The difference between these two designs is discussed by Rye and Frehlich [7].

For a collimated lidar, the near field behavior of heterodyne efficiency can be approximated by

$$\eta_{HNF}(R) = \frac{R^2\lambda^2}{A_R T_T} \int_{-\infty}^{\infty} j_T(\vec{\mathbf{p}}, 0) j_{BPLO}(\vec{\mathbf{p}}, 0) d\vec{\mathbf{p}} \tag{32}$$

For the collimated Gaussian lidar with the Rye design [see Eqs. (11), (13), (15), (16), (19), (25), (32) and normalize the BPLO field to produce $T_R = 1$]

$$\eta_{HNF}(R) = \frac{4\delta_T^2\delta_R^2[1 - \exp(-\delta_T^2 - \delta_R^2)]}{\delta_{RF}^4(\delta_T^2 + \delta_R^2)[1 - \exp(-\delta_T^2)][1 - \exp(-\delta_R^2)]} \tag{33}$$

The optimal LO field for a Gaussian transmitter field and a circular aperture was determined by Frehlich [8] and produces essentially the same performance as the design proposed by Rye. The behavior of heterodyne efficiency for a CLR with the Rye design will be considered here.

3. Simulation of Performance

One important aspect of CLR performance for diffuse and aerosol targets is the random nature of the backscattered field. The superposition of many random backscattered fields with random amplitude and phase produces a complex Gaussian distribution or "speckle field" for the total backscattered field [9]. The detection of such random signals in random noise has been considered by Shapiro et al. [10]. We will investigate the estimation of the heterodyne efficiency by generating computer simulations of the normalized heterodyne power c and the normalized direct detection power d. Realization of the fields on the detector will also be calculated to provide insight.

The backscattered field at the target can be represented as

$$e_S(\vec{\mathbf{p}}, R) = U(\vec{\mathbf{p}}) e_T(\vec{\mathbf{p}}, R) \tag{34}$$

where $U(\vec{\mathbf{p}})$ is a random complex amplitude with the property

$$\langle U(\vec{\mathbf{p}}_1) U^*(\vec{\mathbf{p}}_2) \rangle = \lambda^2 \delta(\vec{\mathbf{p}}_1 - \vec{\mathbf{p}}_2) \tag{35}$$

where $\delta(\vec{\mathbf{p}})[m^{-2}]$ is the two-dimensional delta function. The backscattered field at the receiver plane $e_S(\vec{\mathbf{v}}, 0)$ is given by

$$e_S(\vec{\mathbf{v}}, 0) = \int_{-\infty}^{\infty} e_S(\vec{\mathbf{p}}, R) G(\vec{\mathbf{p}}; \vec{\mathbf{v}}, R) d\vec{\mathbf{p}} \tag{36}$$

The normalized direct detection power is then

$$d = \frac{R^2}{A_R T_T} \int_{-\infty}^{\infty} |W(\vec{\mathbf{v}})|^2 |e_S(\vec{\mathbf{v}}, 0)|^2 d\vec{\mathbf{v}} \tag{37}$$

and the normalized coherent detection power is

$$c = \frac{R^2}{A_R T_T} \left| \int_{-\infty}^{\infty} e_S(\vec{\mathbf{v}}, 0) e^*_{BPLO}(\vec{\mathbf{v}}, 0) d\vec{\mathbf{v}} \right|^2 \tag{38}$$

The effects of angle misalignment $\Delta\theta$ are calculated by multiplying the BPLO field with no misalignment by the phase term [4] $\exp(ik\Delta\theta v_x)$ where $v_x[m]$ is the x-coordinate of the vector $\vec{\mathbf{v}}$. The random fields are calculated using the Fast Fourier Transform (FFT) algorithm to propagate the fields. The random amplitudes $U(\vec{\mathbf{p}})$ are generated using the Box-Muller algorithm.

A typical receiver employs optical elements that pass all the backscattered field. Then, for ideal optical elements, the field on the detector surface is

$$e_S(\vec{\mathbf{w}}, F) = \frac{k}{2\pi i F} \int_{-\infty}^{\infty} W(\vec{\mathbf{v}}) e_S(\vec{\mathbf{v}}, 0) \exp(-\frac{ik}{F} \vec{\mathbf{v}} \cdot \vec{\mathbf{w}}) d\vec{\mathbf{v}} \tag{39}$$

where $F[m]$ is the effective focal distance of the optical system. The fields on the detector surface are particulary intuitive since the heterodyne efficiency is unity when the backscattered field is proportional to the LO field. This is also true for the receiver-plane representation.

4. Results

The simulation results for the far-field optimal design of Rye and the corresponding collimated near-field case with $\delta_{RF} = 4$ will be presented. The statistical variability of the coherent detection power and the direct detection power from a simulation of 10,000 shots for the perfectly aligned CLR for the far-field case is shown in Fig. 1 and for the near-field case in Fig. 2. If the heterodyne efficiency had been unity, all the points would lie on a straight line with a slope of unity. The far-field case has more scatter than the near field case. This is due to the increased spatial averaging of the backscattered irradiance by the telescope aperture in the near-field case.

Typical realizations of the backscattered field on the detector surface for a perfectly aligned CLR is shown in Fig. 3 for the far-field and near-field cases. The dimensions of the central lobe is approximately the diffraction limit $\lambda F/a$ of the circular aperture. The poor match between the backscattered field and LO field for the typical far-field case is the reason the heterodyne efficiency is 0.46096 for the perfectly aligned far-field case. More than half the coherent power is lost due to the random mismatch between the backscattered and LO fields. The near-field case is characterized by a larger distribution of the field over the detector surface with fluctuations on the order of the diffraction limited scale but with reduced amplitude which results in a heterodyne efficiency of 0.021832. The ratio of the heterodyne efficiency to the approximate near-field heterodyne efficiency Eq. (33) is 1.05554. The large number of "speckles" or regions of coherent field produces smaller variability of the direct detection signal (see Fig. 2). Also, for typical CLR designs, the detector would be smaller than the spatial extent of the field and the direct detection power would be reduced. Measurements of heterodyne efficiency in the near-field regime may contain a bias due to the finite extent of the detector. A rare case of high heterodyne efficiency and very low heterodyne efficiency is shown in Fig. 4 for the far-field case.

The sensitivity of heterodyne efficiency to the misalignment angle $\Delta\theta$ of the transmitter and BPLO axis [1, 6] is shown in Fig. 5 for the far-field and near-field cases. The theoretical heterodyne efficiency depends on the single parameter $\Delta q = ka\Delta\theta = \pi D\Delta\theta/\lambda$. The simulation results are in excellent agreement with the theory for both the near-field and far-field case. (The estimation error for each simulation data point is 1%, consistent with exponential statistics for the coherent power.) The heterodyne efficiency was estimated by the ratio of the average of c to the average of d using the 10,000 shots of simulated data in Figs. 1 and 2 and various angle misalignment. In the laboratory one would measure the heterodyne efficiency in this way using a calibration target with a uniform backscatter coefficient ρ. The statistical accuracy of the estimate for heterodyne efficiency is determined by the number of shots averaged and the statistical distribution of the two estimates for $< c >= \eta_H$ and $< d >= 1$. The Probability Density Function (PDF) of the direct detection power d and the Gamma Distribution function $g(d;\alpha,\beta)$ proposed by Goodman [9] are shown in Fig. 6. The Gamma distribution function is given by

$$g(d;\alpha,\beta) = \frac{\alpha^\beta}{\Gamma(\beta)} d^{\beta-1}\exp(-\beta d) \tag{40}$$

and the parameters of the Gamma Distribution are $\alpha = \beta = 1/\sigma_d^2$ where σ_d^2 is the variance of d. For the far-field case $\sigma_d = 0.531$. The same comparison for the near-field case is shown in

Fig. 7. Here, $\sigma_d = 0.1526$. In both cases the simulation results are in reasonable agreement with the Gamma distribution.

The PDF of the normalized coherent detection power for the far-field case is shown in Fig. 8 for perfect alignment along with the theoretical exponential distribution. Because the backscattered field is the superposition of many, randomly phased components, the coherent power should have an Exponential PDF. This was verified by the simulations for all cases.

The estimate of heterodyne efficiency $\hat{\eta}_H$ with a fixed calibration target using the average of J shots is given by

$$\hat{\eta}_H = \frac{\sum_{k=1}^{J} c_k}{\sum_{k=1}^{J} d_k} = \frac{N}{M} \tag{41}$$

where c_k and d_k are the coherent power and direct detection power for shot k. The numerator N has a Gamma Distribution $g(N; 1/\langle c \rangle, J)$ and the denominator M also has a Gamma Distribution $g(M; 1/\sigma_d^2, J/\sigma_d^2)$. For large J, the statistical accuracy of the estimate $\hat{\eta}_H$ is approximately

$$\frac{\Delta\hat{\eta}_H}{\hat{\eta}_H} = \frac{\Delta N}{N} + \frac{\Delta M}{M} = \frac{1 + \sigma_d}{\sqrt{J}} \tag{42}$$

The estimation of heterodyne efficiency for satellite based lidars is a promising technique to verify and maintain beam alignment, but is more difficult since there is no calibration target. The surface return is the most promising signal since it may be large enough to have a detectable direct detection signal but there is added variability from shot to shot due to the random backscatter coefficient of the earths surface and the random atmospheric attenuation. This added variability produces larger scatter in the estimate of the coherent and direct-detection signal power. However, for estimation of heterodyne efficiency, this variability can be removed by defining a biased estimate of heterodyne efficiency for each shot as

$$b = c/d \tag{43}$$

provided the direct detection signal can be estimated accurately for every shot. The average of this biased estimate and it's standard deviation as a function of misalignment angle $\Delta\theta$ is shown in Fig. 9 along with the true heterodyne efficiency (see Fig. 5). The bias of the average of b is small and therefore provides a useful absolute measure of beam alignment. The statistical reliability of this biased estimate depends on the PDF of b, which is shown in Fig. 10 for perfect alignment. Also shown is the PDF of the average of 10 estimates of b and a Gaussian PDF with the correct mean value and variance given by the variance of b divided by the number of shots averaged. The same results for a misalignment of $\Delta q = ka\Delta\theta = \pi D\Delta\theta/\lambda = 2$ which corresponds to 2.08 dB loss in SNR are shown in Fig. 11. The Gaussian approximation for the PDF of the average of 10 estimates of b is a good approximation. However, an accurate estimate of the biased heterodyne efficiency requires an average of many shots. The PDF of a 40 shot average of b is shown in Fig. 12 for perfect alignment and misalignment of $\pi D\Delta\theta/\lambda = 2$ (2.08 dB loss in SNR) and $\pi D\Delta\theta/\lambda = 3$ (4.76 dB loss in SNR), using the Gaussian approximation for the PDF's. The CLR misalignment can be reliably determined with 40 surface returns.

5. Detector Calibration

A real doppler lidar system does not measure the signal currents directly. Therefore, detector calibration is required to extract the required signal currents from the detector signal. The heterodyne efficiency can be estimated using both Continuous Wave (CW) or pulsed mode of operation. For CW operation, two signal currents $I_S(t)$ and I_{DC} are DC signals which are given in terms of the detector voltage V by

$$I(V) = G_D h(V) \tag{44}$$

where $I(V)$ is the photodetector response function $G_D[A/V]$ is the constant for a linear response, and $h(V)[V]$ is the nonlinearity function or deviation from linearity. We assume that the photodetector is ideal in the limit of small voltage, i.e., $h(V) = V$. For pulsed operation, the frequency response of the detector may be required to estimate the direct detection signal $I_S(t)$.

If the magnitude of the IF signal current $i_S(t)$ is small enough and if the magnitude of the IF voltage signal $v_S(t)[V]$ does not change with the IF frequency $\nu[Hz]$ then

$$i_S(t) = G_D f(V) v_S(t) \tag{45}$$

where

$$f(V) = \frac{1}{G_D}\frac{dI(V)}{dV} = \frac{dh(V)}{dV} \tag{46}$$

is proportional to the derivative of the photodetector response function and $f(0) = 1$. A measurement of heterodyne efficiency requires a measurement of $h(V)$ and $f(V)$, which can be performed by the method proposed by Frehlich [11]. (Note that Ref. [11] considered the calibration of integrated irradiance over the detector surface which is proportional to the detector current). The operating point (I_0, V_0) determines the relationship between detector voltages and the ideal signal currents. The direct detection currents are given by

$$I_{DC} = G_D h(V_0) \tag{47}$$

and

$$I_S(t) = G_D f(V_0) V_S(t) \tag{48}$$

where $V_S(t)[V]$ is the increase in the DC detector voltage due to the backscattered field collected by the detector.

The effects of the detector electronics and detector quantum efficiency as a function of IF frequency are described by the normalized frequency response function

$$H(\nu) = \frac{v_S(\nu)}{v_S(\nu \to 0)}. \tag{49}$$

Then

$$i_S(t) = G_D f(V_0) v_S(t)/H(\nu) \tag{50}$$

and the heterodyne efficiency is given by [see Eq. (4)]

$$\eta_H(t) = \frac{f(V_0)\langle v_S^2(t)\rangle}{2h(V_0)\langle V_S\rangle H^2(\nu)} \tag{51}$$

which is expressed in terms of the calibration functions $f(V_0)$, $h(V_0)$, $H(\nu)$, and the detector voltages $v_S(t)$ and $V_S(t)$. Note that the ideal detector gain G_D is not required. The sensitivity of the calibration functions to the detector operating point (I_0, V_0) should be investigated.

6. Summary

The estimation of heterodyne efficiency is an excellent measure of CLR performance since it is proportional to SNR but independent of the transmitter power, the target backscatter coefficient, the atmospheric attenuation, and the detector quantum efficiency and gain. The heterodyne efficiency is an absolute measure of the alignment of the backscattered and LO field on the detector surface. The estimation of heterodyne efficiency is a statistical problem because the detector signals are random. An estimation of the heterodyne efficiency requires an accurate average of the coherent detection power, the direct detection power, and the LO current. When using a calibration target, an unbiased estimate of the heterodyne efficiency can be obtained by an ensemble average of the coherent and direct detection power. For a lidar in space, the ratio of the coherent detection power to the direct detection power for each ground return is a convenient biased estimate of heterodyne efficiency. The average of this biased estimate produces a sensitive measure of CLR alignment and removes the statistical variability of the random fluctuations of the signals due to the random backscatter coefficient of the earth surface and the random atmospheric attenuation. Using 40 shots produces an effective measure of system performance and beam alignment [see Fig. 12]. All the results presented here assume a large detector that collects all the LO power and all the backscattered power.

The calibration of real detectors requires two measurements: the low frequency response function $h(V)$ (which is obtained [11] from a measurement of $f(V)$, the derivative of $h(V)$) and the frequency response $H(\nu)$.

Acknowledgments

The author acknowledges useful discussions with M. J. Kavaya, B. J. Rye, and G. Spiers. This work was supported by the National Science Foundation and the National Aeronautics and Space Administration Marshall Space Flight Center under Research Grant NAG8-253 (Michael J. Kavaya, Technical Officer).

References

1. R. G. Frehlich and M. J. Kavaya, "Coherent laser radar performance for general atmospheric refractive turbulence," Appl. Opt. **30,** 5325-5352 (1991).
2. Y. Zhao, M. J. Post, and R. M. Hardesty, "Receiving efficiency of monostatic pulsed coherent lidars. 1: Theory," Appl. Opt. **29,** 4111-4119 (1990).
3. G. O. Olaofe, "Diffraction by gaussian apertures," J. Opt. Soc. Am. **60,** 1654-1657 (1970).
4. R. G. Frehlich, "Effects of refractive turbulence on coherent laser radar," Appl. Opt. **32,** 2122-2139, (1993)
5. J. Y. Wang, "Optimum truncation of a lidar transmitted beam," Appl. Opt. **27,** 4470-4474 (1988).
6. B. J. Rye, "Primary aberration contribution to incoherent backscatter heterodyne lidar returns," Appl. Opt. **21,** 839-844 (1982).
7. B. J. Rye and R. G. Frehlich, "Optimal truncation of Gaussian beams for coherent lidar using incoherent backscatter," Appl. Opt. **31,** 2891-2899 (1992).
8. R. G. Frehlich, "Optimal design of monostatic coherent laser radar with a circular aperture", Appl. Opt. **32,** 4569-4577 (1993).
9. J. W. Goodman, "Some effects of target-induced scintillation on optical radar performance," Proc. IEEE, **53,** 1688-1700 (1965)
10. Shapiro, J.H., B.A. Capron, and R.C. Harney, "Imaging and target detection with a heterodyne-reception optical radar" Appl. Opt. **20,** 3292-3313 (1981).
11. R. G. Frehlich, "Estimation of the non-linearity of a photodetector," Appl. Opt. **31,** 5926-5929, (1992).

Figure 1

Fig. 1. Normalized coherent detection power c versus the normalized direct detection power d for a perfectly aligned CLR and 10,000 shots with the target in the far field.

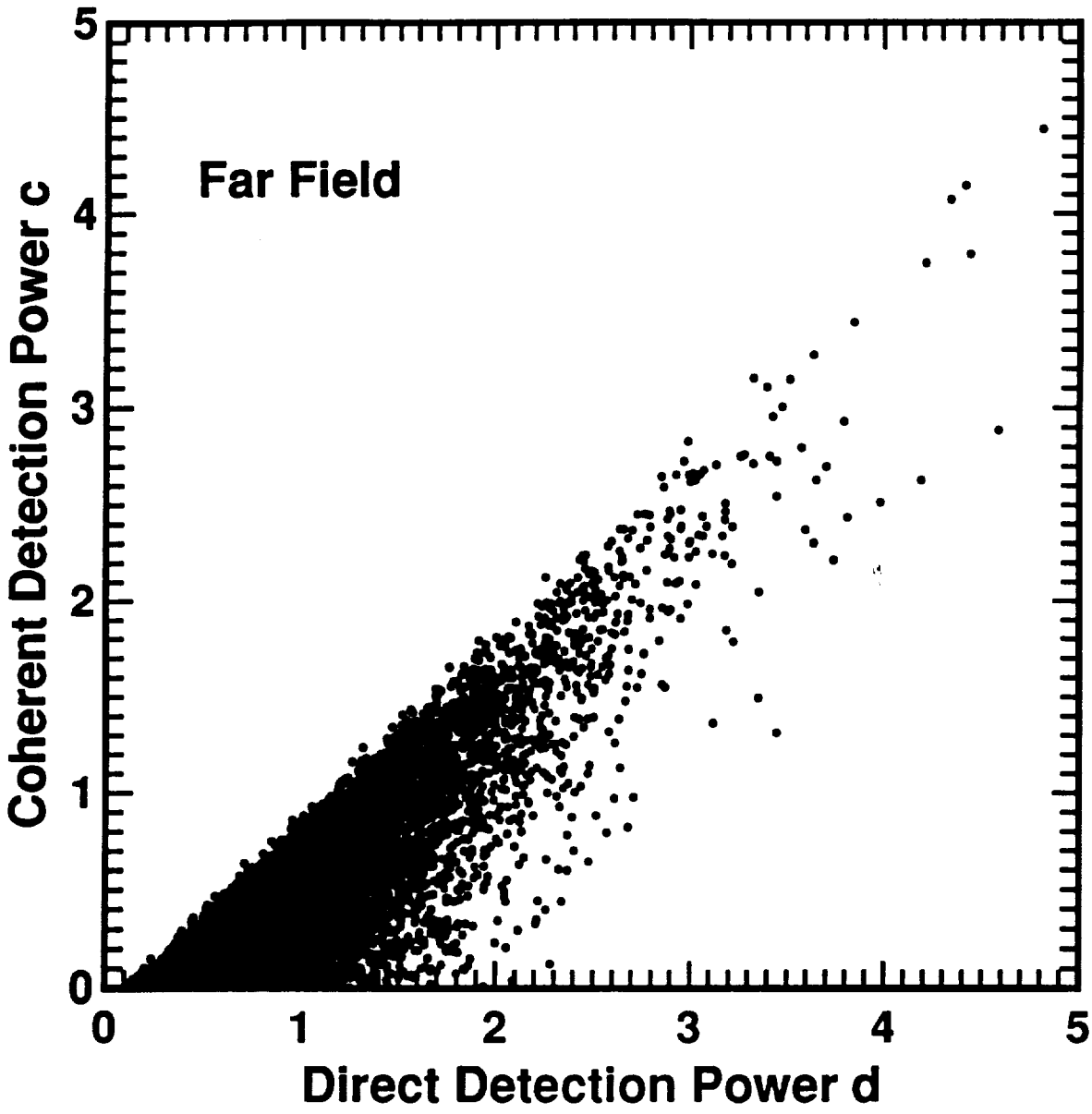

Figure 2

Fig. 2. Normalized coherent detection power c versus the normalized direct detection power d for a perfectly aligned CLR and 10,000 shots with the target in the near field ($\delta_{RF} = a/R_F = 4$).

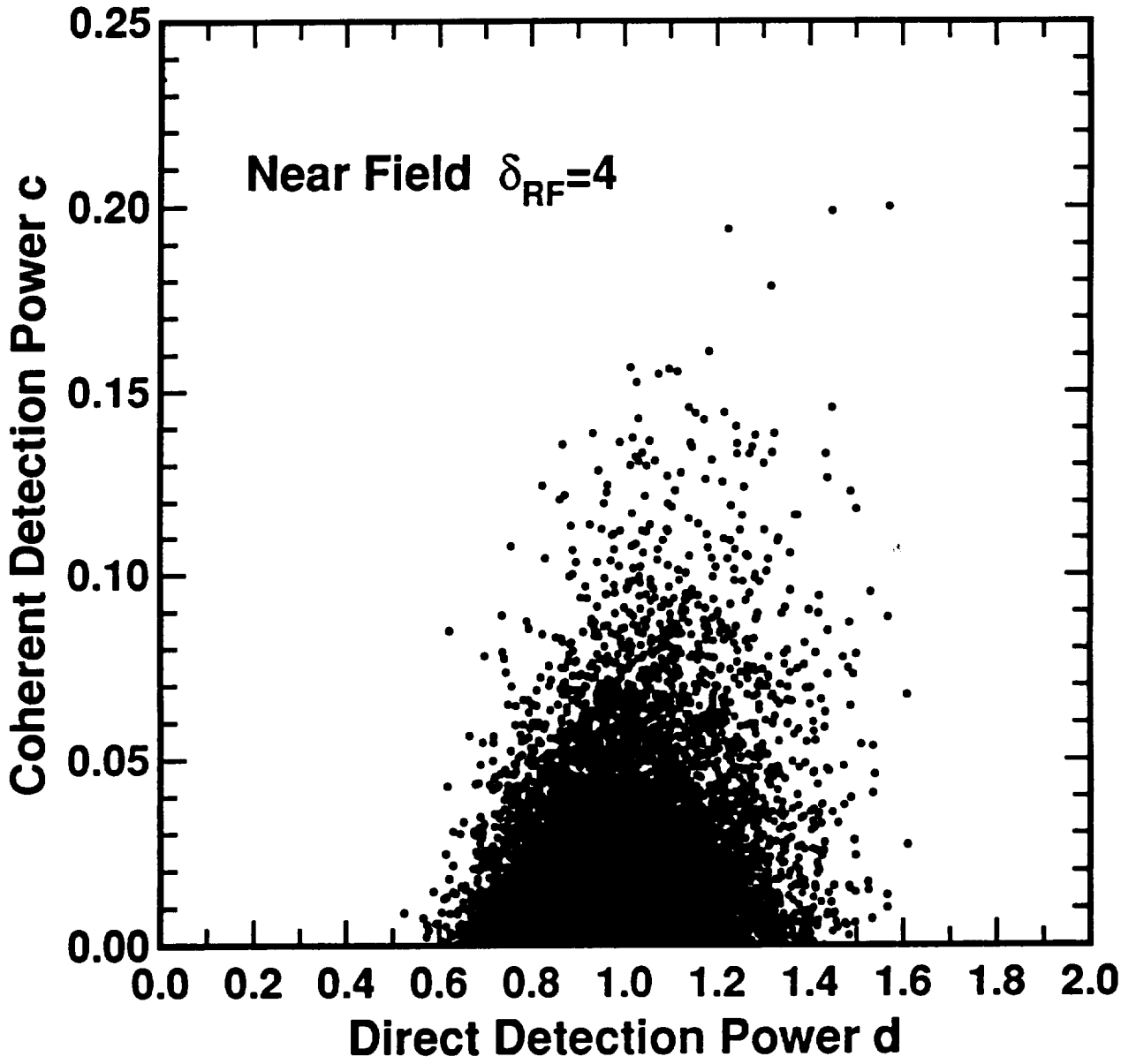

Fig. 3. Simulation of the backscattered field on the detector surface in the x direction $e_S(w_x, F)$ and the y direction $e_S(w_y, F)$ for typical far field ($\eta_H = 0.460$, $d = 1.015$, $c = 0.467$) and near field with $\delta_{RF} = a/R_F = 4$ ($\eta_H = 0.0785$, $d = 0.969$, $c = 0.0760$) cases. The real part of the complex field is (—) and the imaginary part is ($\cdots$). The optimal LO field $e_{LO}(w, F)$ is also shown.

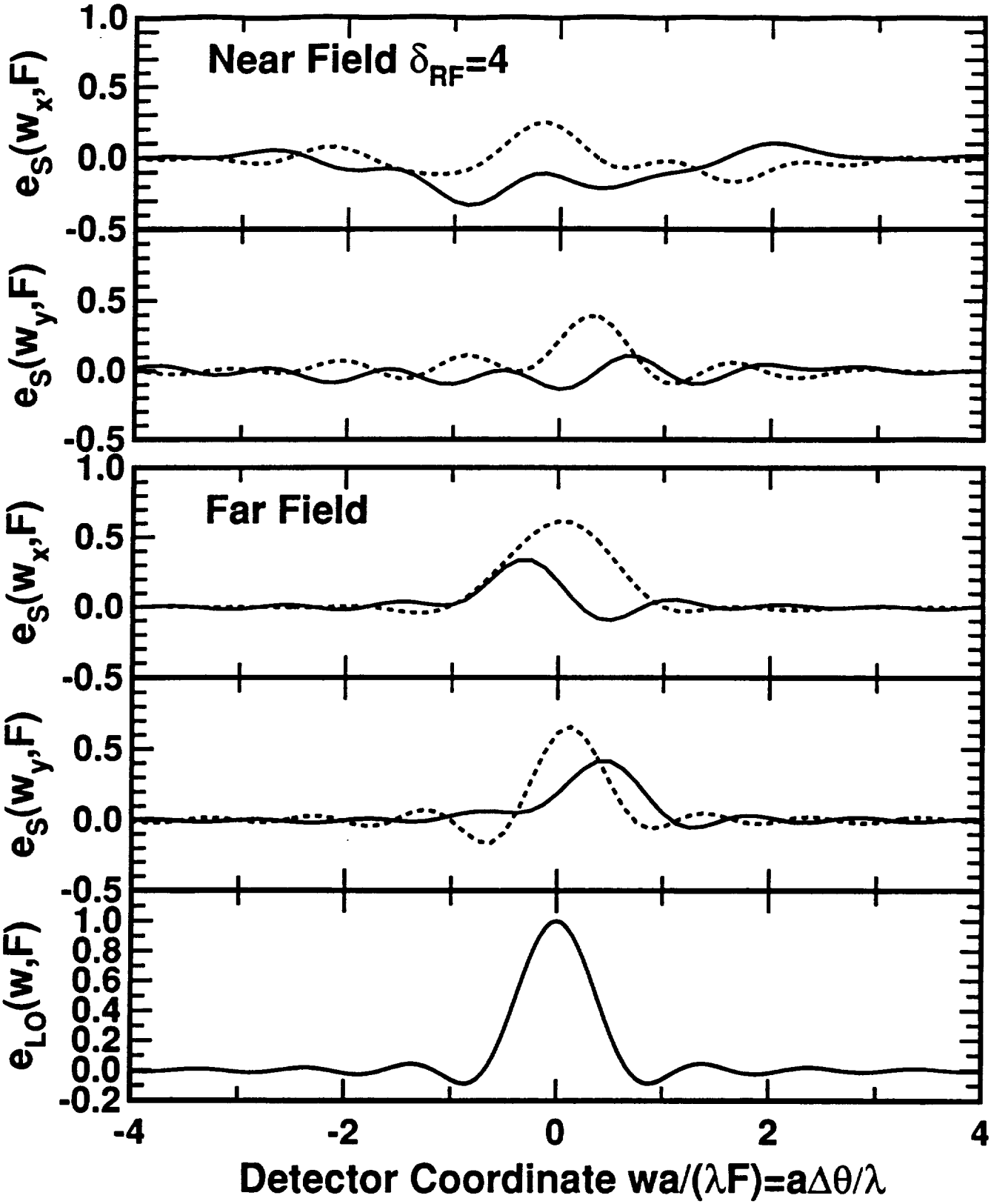

Fig. 4. Simulation of the backscattered field on the detector surface in the x direction $e_S(w_x, F)$ and the y direction $e_S(w_y, F)$ for far field and rare cases of excellent heterodyne efficiency (η_H = 0.9465, d = 3.325, c = 3.147) and poor heterodyne efficiency (η_H = 0.000344, d = 0.830, c = 0.000286). The real part of the complex field is (—) and the imaginary part is ($\cdots$). The optimal LO-field $e_{LO}(w, F)$ is also shown.

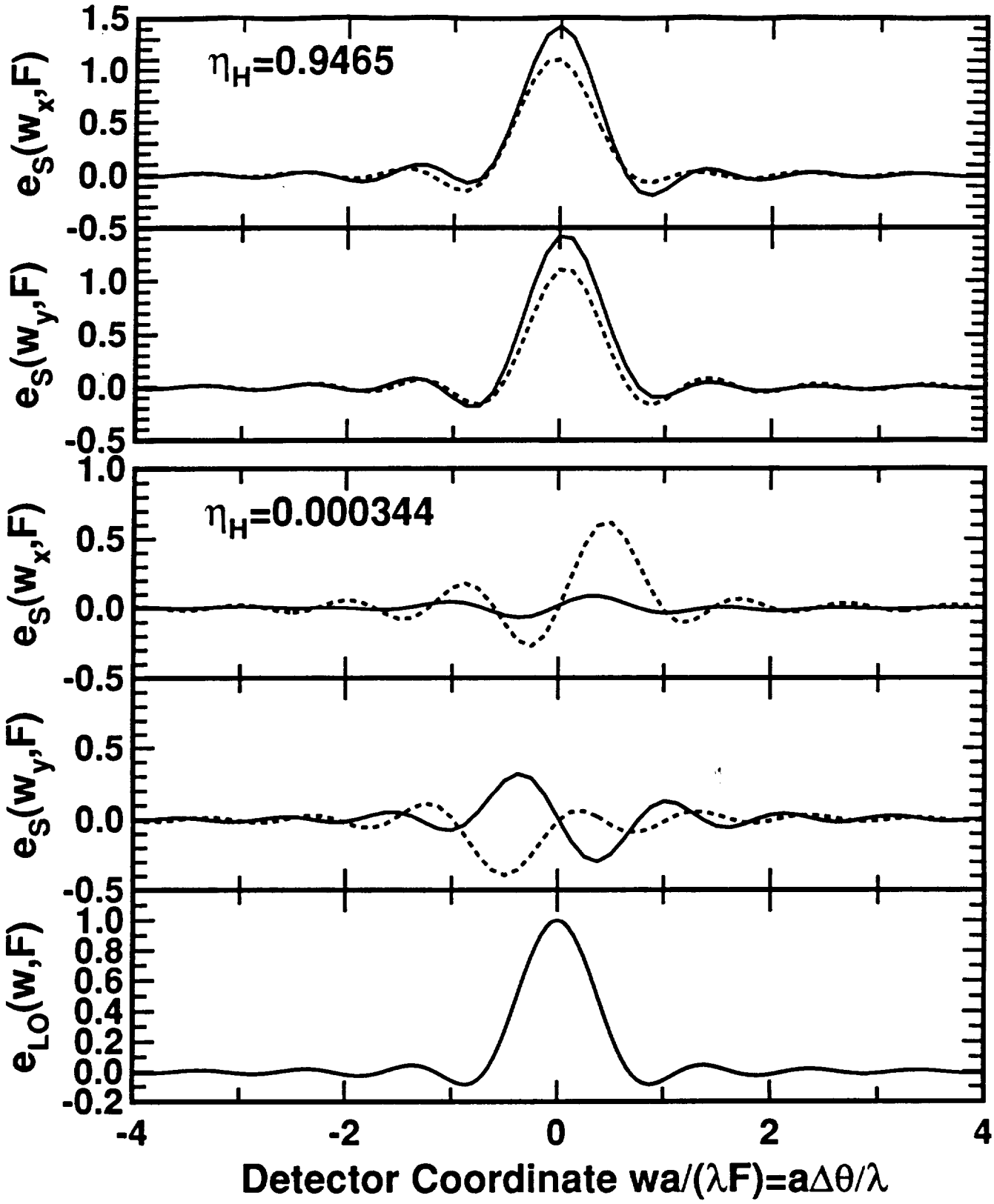

Figure 5

Fig. 5. Heterodyne efficiency η_H as a function of misalignment $\pi D\Delta\theta/\lambda$ with the results of the 10,000 shot simulation of Fig. 1 for the far-field (•) and near-field (o) cases with $\delta_{RF} = a/R_F = 4$. The theoretical calculations Eq. (31) are (—). The best-fit Gaussian function $0.46096\exp[-(\pi D\Delta\theta/2.8363\lambda)^2]$ is $(\cdots)$ and the best fit power-law model $0.9157(\pi D\Delta\theta/\lambda)^{-3.0415}$ is (- - -).

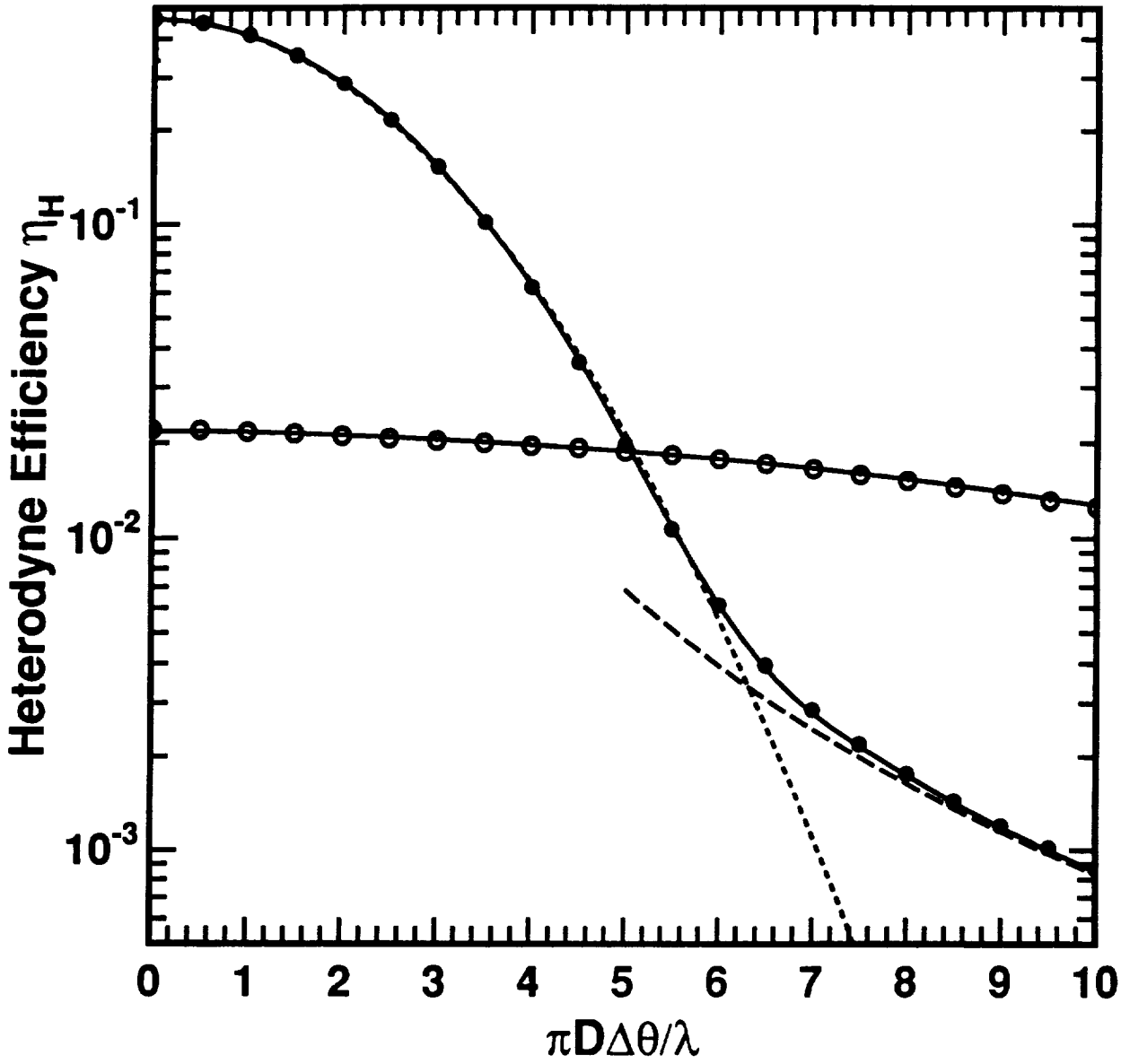

Figure 6

Fig. 6. PDF of direct detection power d from simulation of Fig. 1 and the theoretical Gamma distribution (—) for a perfectly aligned CLR in the far-field.

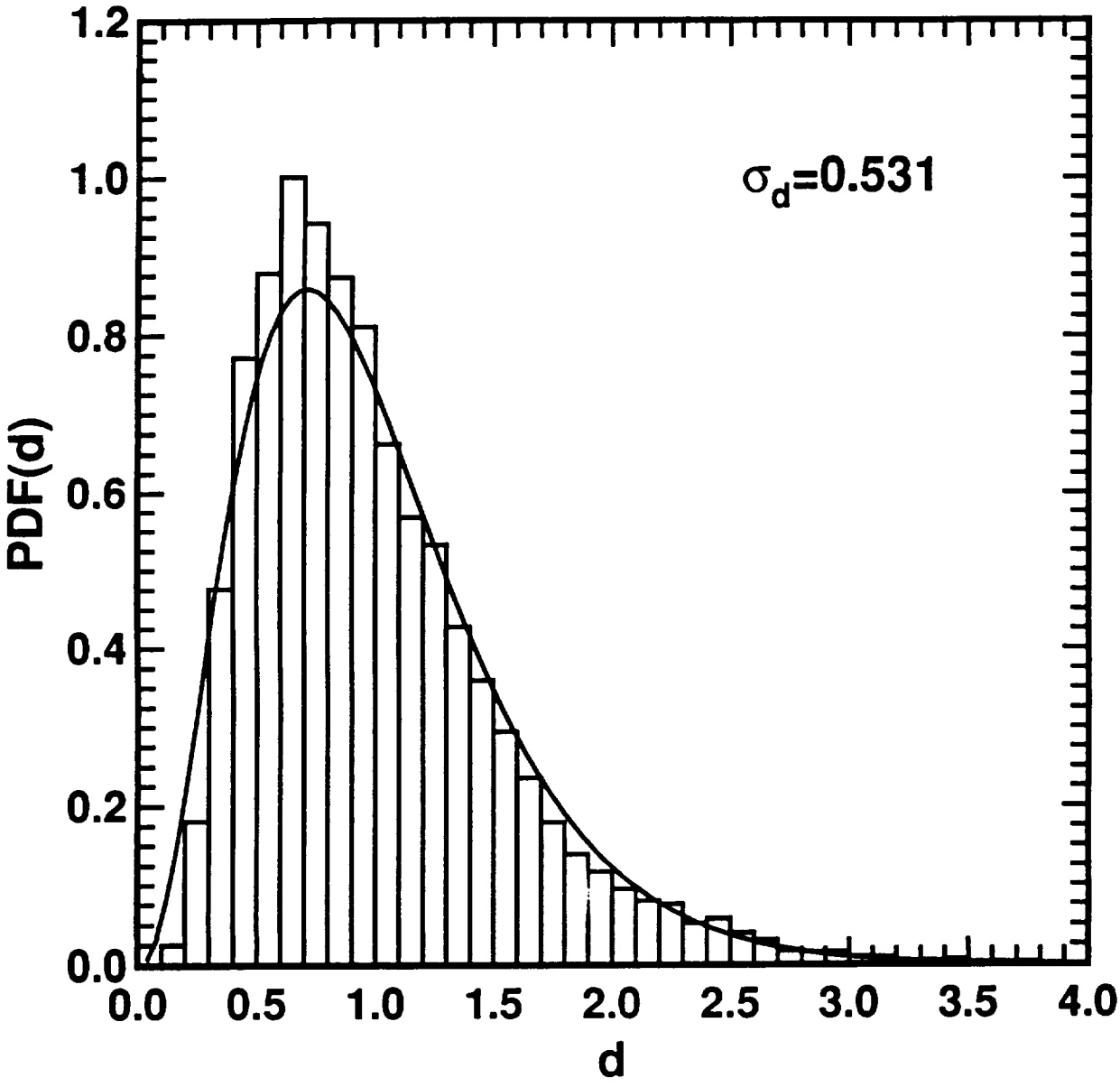

Figure 7

Fig. 7. PDF of direct detection power d using the average of 10 shots from the simulation of Fig. 1 and the theoretical Gamma distribution (—) for a perfectly aligned CLR in the far-field.

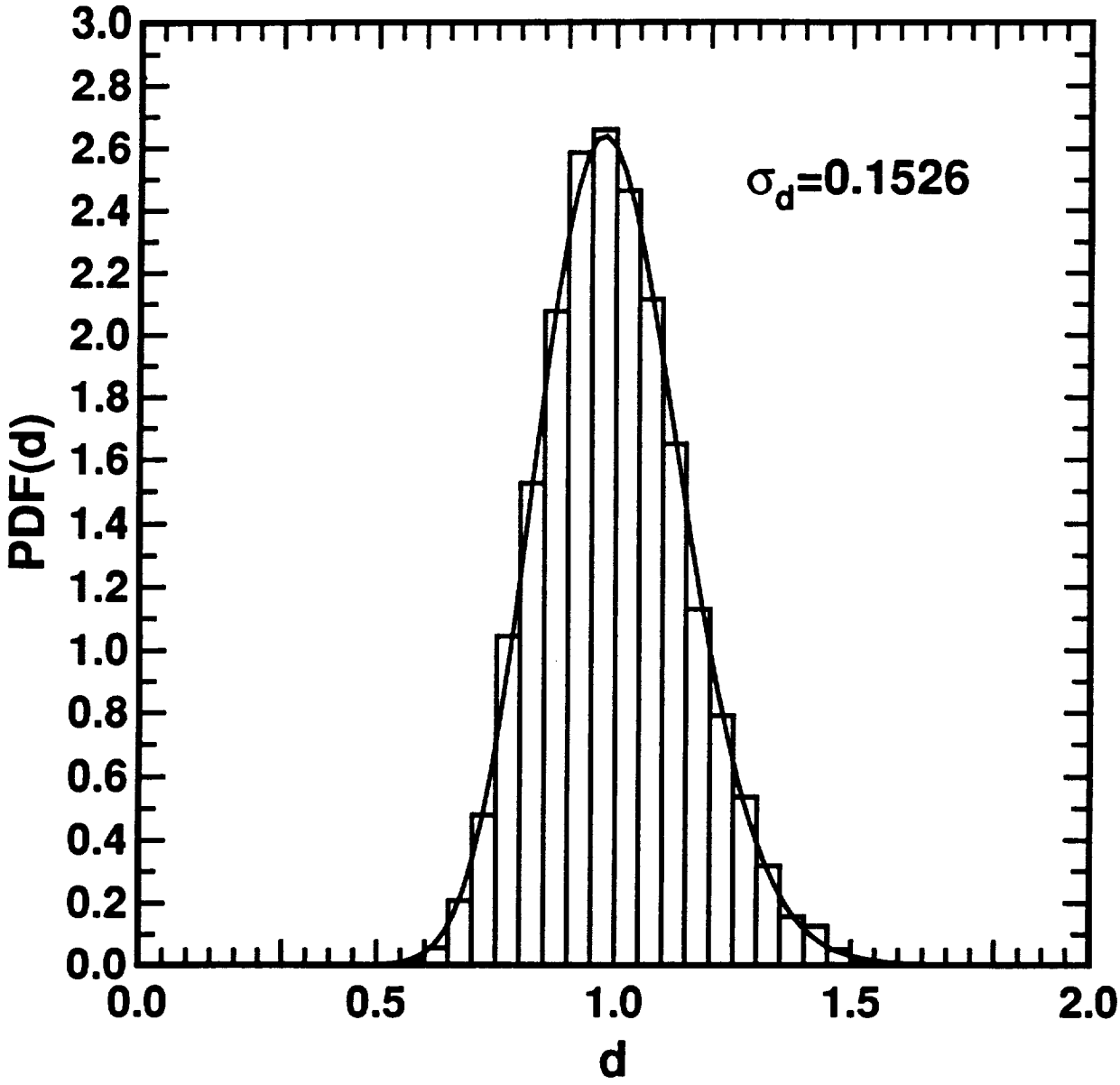

Figure 8

Fig. 8. PDF of coherent detection power c from simulation of Fig. 1 and the theoretical Exponential distribution (—) for a perfectly aligned CLR in the far-field.

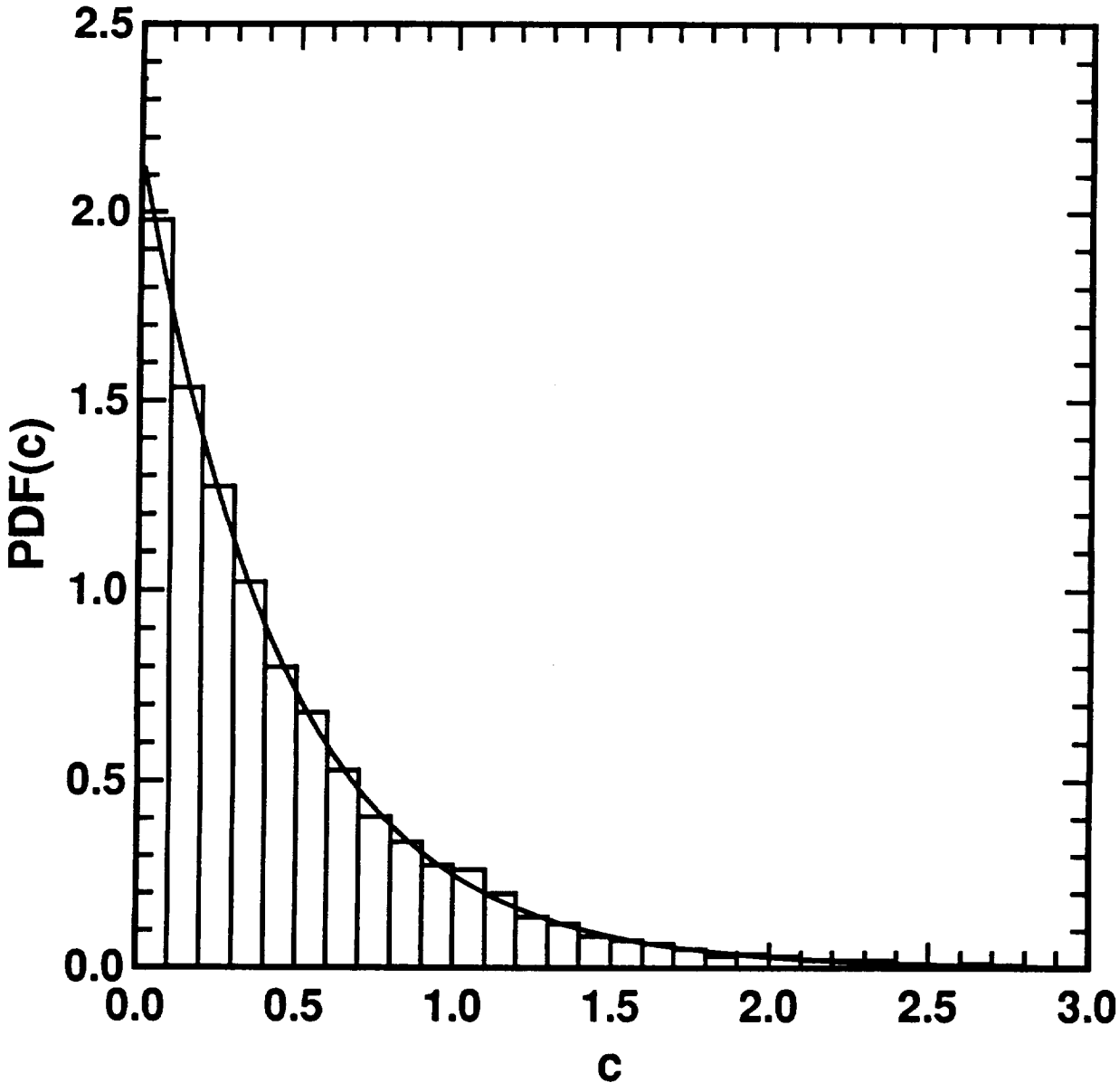

Figure 9

Fig. 9. Biased estimates of heterodyne efficiency $b = c/d$ as a function of misalignment $\pi D\Delta\theta/\lambda$. The average of 10,000 simulations for the far-field • and near-field ○ cases of Fig. 1. The standard deviation for the far-field ◇ and near-field □ are also shown as well as the theoretical calculations for unbiased heterodyne efficiency Eq. (31) (—).

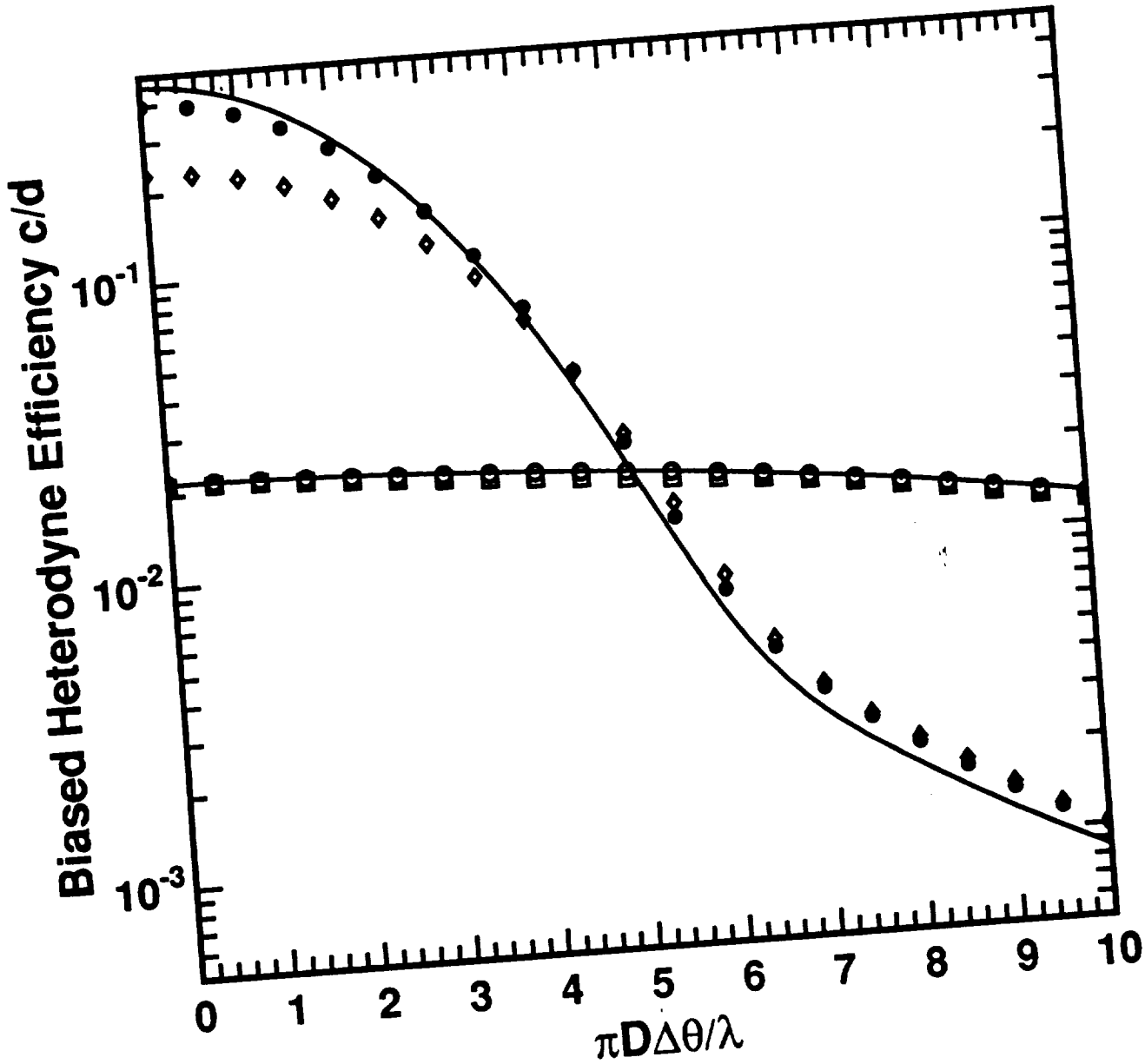

Figure 10

Fig. 10. PDF of the biased estimate of heterodyne efficiency $b = c/d$ for perfect alignment in the far-field for 1 shot and the average of 10 shots. The Gaussian PDF (—) with the estimated mean $< b >$ and standard deviation σ_b.

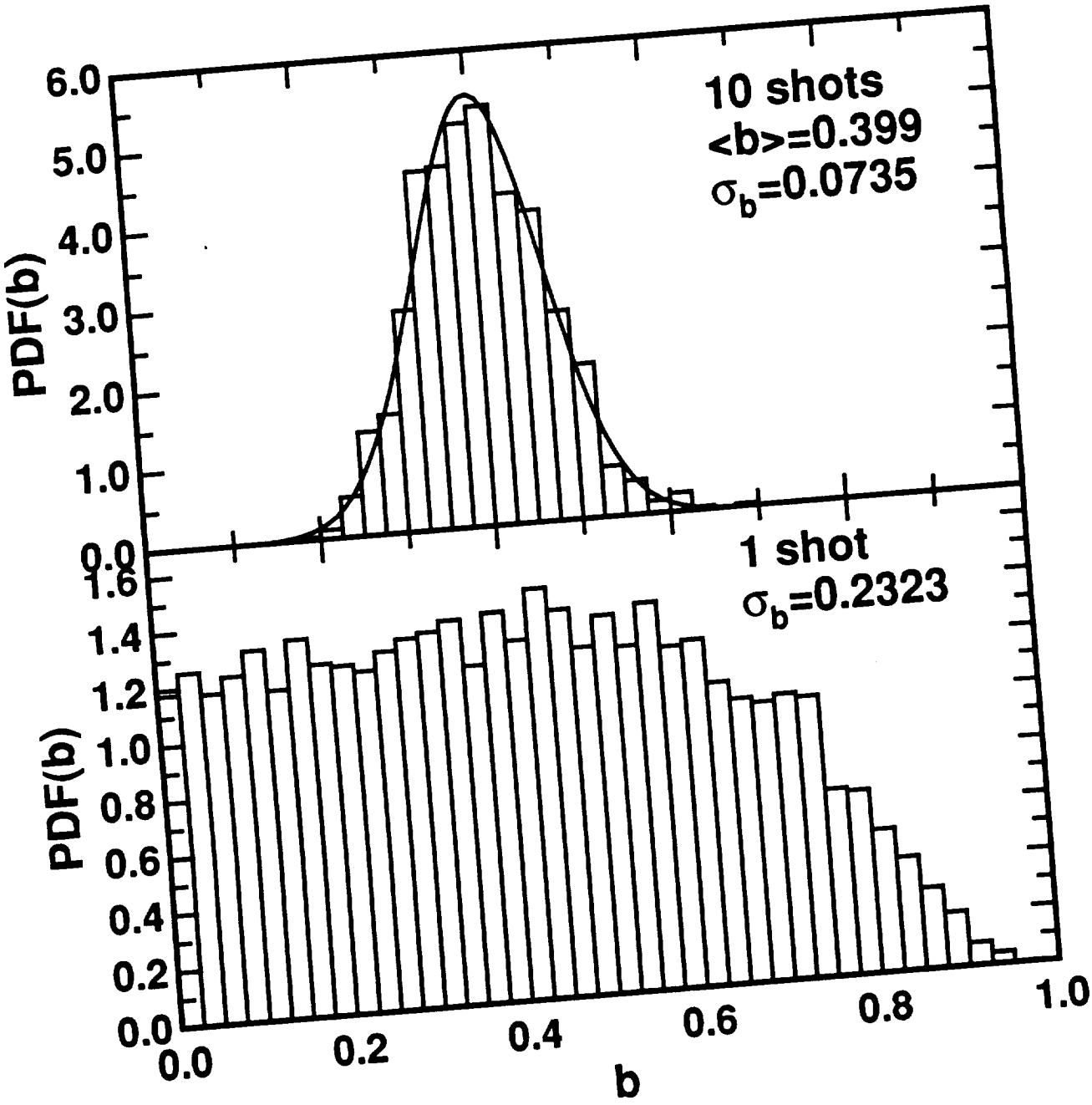

Figure 11

Fig. 11. PDF of the biased estimate of heterodyne efficiency $b = c/d$ for a misalignment of $\pi D\Delta\theta/\lambda = 2$ in the far-field for 1 shot and the average of 10 shots. The Gaussian PDF (—) with the estimated mean $< b >$ and standard deviation σ_b.

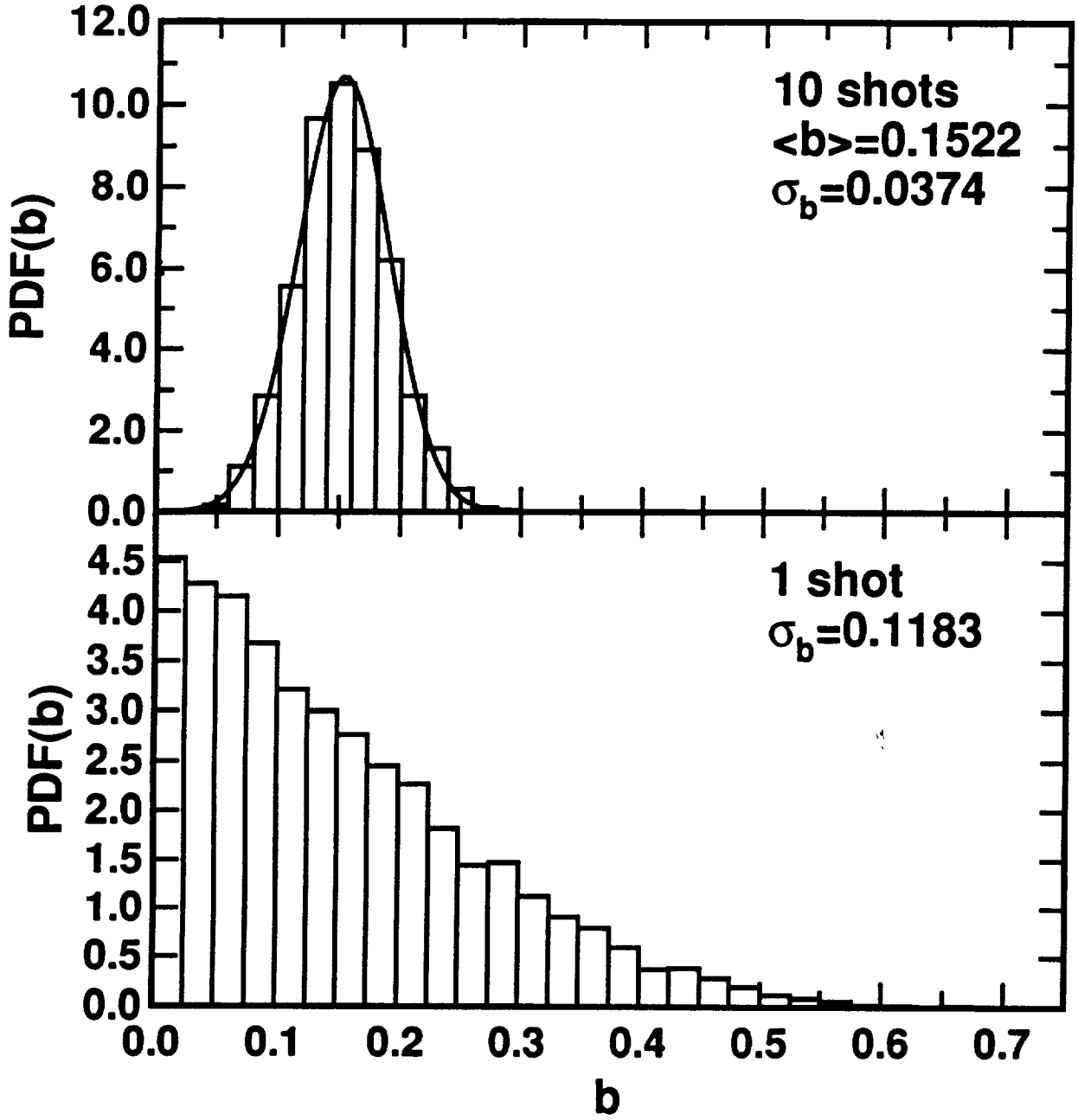

Figure 12

Fig. 12. PDF of the average of 40 estimates of b for a misalignment of $\pi D\Delta\theta/\lambda = 0$ (—), 2 ($\cdots$), and 3 ($- - -$) assuming a Gaussian PDF.

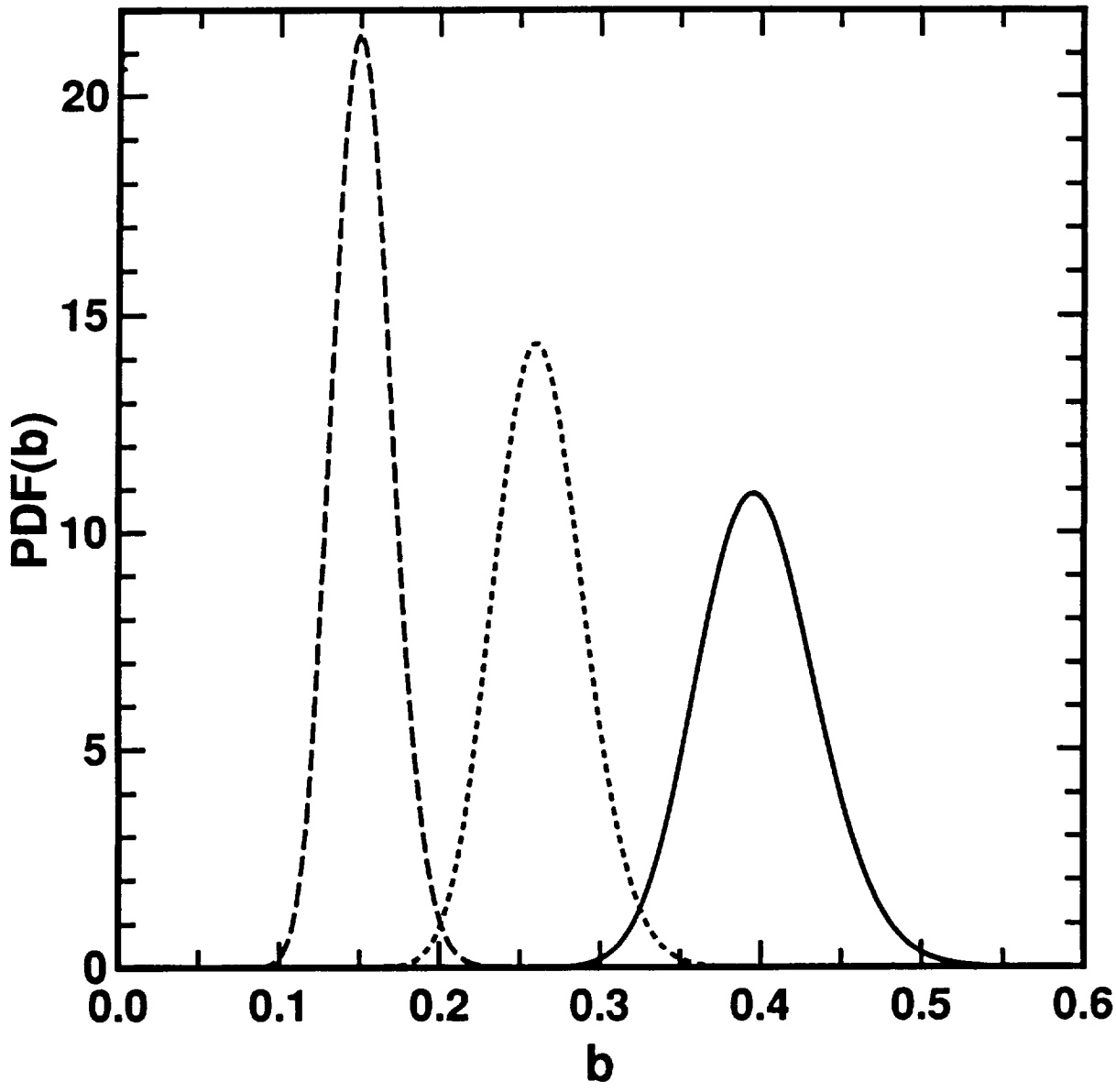

Coherent Doppler Lidar Signal Covariance including Wind Shear and Wind Turbulence

R. G. Frehlich
Cooperative Institute for Research in the Environmental Sciences (CIRES)
University of Colorado, Boulder, CO 80309

Abstract

The performance of coherent Doppler lidar is determined by the statistics of the coherent Doppler signal. The derivation and calculation of the covariance of the Doppler lidar signal is presented for random atmospheric wind fields and wind shear. The signal parameters are defined for a general coherent Doppler lidar system in terms of the atmospheric parameters. There are two distinct physical regimes: one where the transmitted pulse determines the signal statistics and the other where the wind field and atmospheric parameters dominate the signal statistics. When the wind fields dominate the signal statistics, Doppler lidar data is non-stationary and the signal correlation time is proportional to the operating wavelength of the lidar. The signal covariance is derived for single shot and multiple shot conditions. For a single shot, the parameters of the signal covariance depend on the random, instantaneous, atmospheric parameters. For multiple shots, various levels of ensemble averaging over the temporal scales of the atmospheric processes are required. The wind turbulence is described by a Kolmogorov spectrum with an outer-scale of turbulence. The effects of the wind turbulence is demonstrated with calculations for a horizontal propagation path in the atmospheric surface layer.

Key words: Lidar, Remote Sensing.

1. Introduction

Coherent Doppler lidar has become a promising new instrument for observations of the atmosphere. The first systems were based on the CO_2 laser[1–4]. More recently, solid state lasers have been successful integrated in Doppler lidar designs[5–7]. The targets for Dopper lidar are small atmospheric aerosol particles. Doppler lidar data can be the return from a single pulse or a collection of many pulses along the same line of sight. The advantages of multiple pulse has been discussed by Rye and Hardesty[8], and Frehlich and Yadlowski[9]. Coherent Doppler lidar data is used to estimate the radial velocity of the targets using various mean-frequency estimators[8–16].

The actual measurement quantity is related to the statistics of the random wind field over the sensing volume of the pulse. The effects of the pulse volume averaging for Doppler radar has been investigated by Doviak and Zrnic[16]. The estimated Doppler frequency is defined in terms of the spectrum of the signal. Doppler radar data is generated by transmitting many pulses and sampling the returns at fixed sampling interval $T_S[sec]$, which corresponds

to sampling the same spatial volume defined by the pulse at equally spaced time intervals. For this case, the statistics of the data are determined by the time evolution of the sensing volume of the pulse, and the spectrum is a well defined quantity. For coherent Doppler lidar, the data is generated from a single pulse as it travels through the atmosphere. The sensing volume of the Doppler lidar data is determined by the distance the pulse travels in the finite observation time of each estimate $T = MT_S[sec]$, where M is the total number of data points per estimate. The spectrum is not well defined and the Doppler frequency is related to the statistics of the wind field over the sensing volume of the single pulse. The signal parameters are then related to the wind fields and lidar system parameters in a different fashion than for the Doppler radar. This connection will be derived to clarify the meaning of coherent Doppler lidar measurements and pave the way for more reliable estimators of the signal parameters.

The statistical description of coherent Doppler lidar data from aerosol targets has been shown to be well represented as a zero mean Gaussian random process. It is a common practice to follow the tradition of Doppler radar and convert the real signal to the complex analytical signal using a quadrature receiver[16–18] or digital signal processing[19,20]. This generates complex data with desirable statistical properties that simplify the calculation of the Cramer-Rao Bound[15,16,21] (the ideal performance of estimators of the signal parameters) and the development of efficient estimators of the signal parameters. Since the data is a Gaussian random process, the signal covariance provides a complete statistical description of the data. The signal covariance is derived for a general coherent Doppler lidar including random wind fields and wind shear. The derivation follows the analyses of Frehlich and Kavaya[22] for the performance of coherent laser radar for general atmospheric refractive turbulence.

2. Coherent Doppler Lidar Signal

A coherent Doppler lidar can be represented by the transmitter aperture function $W_T(\vec{u})$, the transmitter laser field incident on the transmitter aperture $E_L(\vec{u},0,t)[(Wm^{-2})^{1/2}]$, the receiver aperture function $W_R(\vec{v})$, and the Local Oscillator (LO) field incident on the receiver aperture $E_{LO}(\vec{v},0)[(Wm^{-2})^{1/2}]$. Here, $t[sec]$ denotes time and $\vec{u}[m]$ and $\vec{v}[m]$ denote the transverse two-dimensional vectors of the transmitter and receiver plane, respectively. The field of the transmitter laser pulse with frequency $f_L[Hz]$ is written as

$$E_L(\vec{u},0,t) = U_L A_L(t) e_L(\vec{u},0) \exp(2\pi i f_L t) \tag{1}$$

where $U_L[J]$ is the laser pulse energy, $e_L(\vec{u},0)[m^{-1}]$ is the normalized spatial field which is assumed independent of time t (the spatial mode of the laser pulse is independent of time) and

$$A_L(t) = J_L^{1/2}(t) \exp\left[2\pi i \int_0^t f_C(t')dt'\right] \tag{2}$$

is the normalized complex amplitude of the pulse where $f_C(t')[Hz]$ is the frequency chirp of the transmitted pulse and

$$\int_{-\infty}^{\infty} |A_L(t)|^2 dt = 1 \tag{3}$$

The LO field in the receiver plane with frequency $f_{LO}[Hz]$ is given by

$$E_{LO}(\vec{\mathbf{v}},0) \;=\; P_{LO}^{1/2} e_{LO}(\vec{\mathbf{v}},0)\exp(2\pi i f_{LO} t) \tag{4}$$

where $P_{LO}[W]$ is the LO power,$e_{LO}(\vec{\mathbf{v}},0)[m^{-1}]$ is the normalized spatial field which is assumed independent of time t, and

$$\int_{-\infty}^{\infty} |e_{L,LO}(\vec{\mathbf{u}},0)| d\vec{\mathbf{u}} = 1 \tag{5}$$

The coherent Doppler lidar typically operates under the ideal condition of quantum limited detection, i.e., the signal noise is dominated by the shot noise of the LO field. The effects of extra additive system noise is a simple extension. We will assume that the detector quantum efficiency $\eta_Q[electrons/photon]$ is uniform over the surface of the detector and that all the LO power is collected by the detector.

For Doppler lidar measurements of the atmosphere, the backscattered field is a zero-mean Gaussian random process because it is the superposition of the backscattered fields from many random aerosol particles. The doppler lidar signal is also a zero-mean Gaussian random process because it is a linear function of the backscattered field. It is convenient to normalize the signal by the standard deviation of the noise signal and employ the complex representation (Appendix A)

$$Z(t) = S(t) + N(t) = Re[z(t)] \tag{6}$$

where $S(t)$ is the normalized Doppler lidar IF current signal from the backscattered field and $N(t)$ is the normalized additive detector noise. The statistical description of a real or complex zero-mean Gaussian random process $\xi(t)$ is given by the covariance function

$$B_\xi(t_1,t_2) = \langle \xi(t_1)\xi(t_2)\rangle \tag{7}$$

For complex random processes $z(t)$, further simplification results if

$$\langle z(t_1)z(t_2)\rangle = 0 \tag{8}$$

Then, the covariance of the real random process $Z(t)$ is related to the covariance of the complex random process $z(t)$ by

$$B_Z(t_1,t_2) = \frac{1}{2} Re[B_z(t_1,t_2)] = Re[R_z(t_1,t_2)] \tag{9}$$

where $Re[z]$ denotes the real part of the complex variable z. The function $R_z(t_1,t_2) = B_z(t_1,t_2)/2$ is commonly used[9,11,15–18,21] for analysis of Gaussian random processes because of mathematical convenience.

For Doppler lidar, the signal $S(t)$ is statistically independent of the noise $N(t)$ and

$$B_Z(t_1,t_2) = B_S(t_1,t_2) + B_N(t_1,t_2) \tag{10}$$

The noise $N(t)$ is usually well described as a white-noise process over the receiver bandwidth $B[Hz]$. For the normalized Doppler lidar signal (Appendix A),

$$B_S(t,t) = \frac{1}{2}B_s(t,t) = R_s(t,t) = SNR(t) \tag{11}$$

where SNR is the coherent lidar signal-to-noise ratio with respect to the appropriate ensemble average. The Doppler lidar signal is typically uncorrelated from shot to shot because the aerosol targets move more than a wavelength between shots, which results in random phases for the backscattered signal from shot to shot. The ensemble average over the random phases of the backscattered fields from the aerosol particles produces (Appendix A)

$$R_s(t_1,t_2) = \frac{\eta_Q U_L}{h\nu B}\int_0^\infty\int_{-\infty}^\infty A_L(t_1 - 2\frac{z}{c})A_L^*(t_2 - 2\frac{z}{c})K^2(\vec{\mathbf{p}},z)\beta(\vec{\mathbf{p}},z)|Q(\vec{\mathbf{p}},z)|^2 \exp\{2\pi i(t_1-t_2)[\Delta f - 2v_r(\vec{\mathbf{p}},z)/\lambda]\}d\vec{\mathbf{p}}dz \tag{12}$$

where $h = 6.626\text{x}10^{-34}[Js]$ is Planck's constant, $\nu[Hz]$ is the optical frequency, $c[m/sec]$ is the speed of light in a homogenous atmosphere, $K(\vec{\mathbf{p}},z)$ is the one-way irradiance extinction, $\beta(\vec{\mathbf{p}},z)[m^{-1}sr^{-1}$ is the aerosol backscatter coefficient, $v_r(\vec{\mathbf{p}},z)$ is the radial component of the velocity of the aerosol particles at coordinate $(\vec{\mathbf{p}},z)$, $\Delta f = f_L - f_{LO}$ is the frequency difference between the transmitted field and the LO field, and the lidar system function $Q(\vec{\mathbf{p}},z)[m^{-1}]$ is given by

$$Q(\vec{\mathbf{p}},z) = \lambda\int_{-\infty}^\infty\int_{-\infty}^\infty W_T(\vec{\mathbf{u}})W_R(\vec{\mathbf{v}})e_L(\vec{\mathbf{u}},0)e_{LO}^*(\vec{\mathbf{v}},0)G(\vec{\mathbf{p}};\vec{\mathbf{u}},z)G(\vec{\mathbf{p}};\vec{\mathbf{v}},z)d\vec{\mathbf{u}}d\vec{\mathbf{v}} \tag{13}$$

where $G(\vec{\mathbf{p}};\vec{\mathbf{u}},z)[m^{-2}]$ is the Green's function for propagating the field from the transmitter coordinate $(\vec{\mathbf{u}},0)$ to the aerosol coordinate $(\vec{\mathbf{p}},z)$. For Doppler lidar, the complex signal $z(t)$ also satisfies Eq. (8) (see Appendix A) which facilitates data analysis and the development of estimation algorithms. The functions $R_z(t_1,t_2)$ and $B_z(t_1,t_2)$ are hermitian function, i.e.,

$$R_z(t_1,t_2) = R_z^*(t_2,t_1) \tag{14}$$

With a high pulse rate Doppler lidar, many shots can be transmitted while the the random Green's function $G(\vec{\mathbf{p}};\vec{\mathbf{u}},z)$ (which is usually determined by the atmospheric refractive turbulence) and the random radial velocity fluctuations $v_r(\vec{\mathbf{p}},z)$ are essentially constant. For example, a surface layer lidar can transmit 10,000 shot per second before the signals from adjacent pulses interfere. Doppler lidar has the potential to investigate the statistics of wind fluctuations and refractive turbulence.

The ensemble average over refractive turbulence produce

$$R_s(t_1,t_2) = \frac{\eta_Q U_L}{h\nu B}\int_0^\infty\int_{-\infty}^\infty A_L(t_1 - 2z/c)A_L^*(t_2 - 2z/c)O(\vec{\mathbf{p}},z) \exp\{2\pi i(t_1-t_2)[\Delta f - 2v_r(\vec{\mathbf{p}},z)/\lambda]\}\,d\vec{\mathbf{p}}dz \tag{15}$$

where $O(\vec{\mathbf{p}},z)[m^{-3}]$ is the gain density

$$O(\vec{\mathbf{p}},z) = K^2(\vec{\mathbf{p}},z)\beta(\vec{\mathbf{p}},z)c(\vec{\mathbf{p}},z)\,, \tag{16}$$

and $c(\vec{\mathbf{p}},z)[m^{-2}]$ is the coherent responsivity density[22] of the coherent Doppler lidar, i.e.,

$$c(\vec{\mathbf{p}},z) = |Q(\vec{\mathbf{p}},z)|^2\,. \tag{17}$$

For many applications, the effects of refractive turbulence are negligible and

$$G(\vec{\mathbf{p}};\vec{\mathbf{u}},z) \;=\; G^f(\vec{\mathbf{p}};\vec{\mathbf{u}},z) = \frac{ik}{2\pi z}\exp\left[-\frac{ik}{2z}(\vec{\mathbf{p}}-\vec{\mathbf{u}})^2\right] \tag{18}$$

where $G^f(\vec{\mathbf{p}};\vec{\mathbf{u}},z)$ is the free space Green's function and $k = 2\pi/\lambda[m^{-1}]$ is the wavenumber of the laser field. The fluctuations of the radial component of the wind field $v_r(\vec{\mathbf{p}},z)$, the atmospheric extinction $K(\vec{\mathbf{p}},z)$, and the backscatter coefficient $\beta(\vec{\mathbf{p}},z)$, are the remaining random quantities.

Churnside and Yura[23] considered the signal covariance as an ensemble average over $v_r(\vec{\mathbf{p}},z)$ by assuming $v_r(\vec{\mathbf{p}},z)$ was a Gaussian random variable with mean value $\overline{v}_z$ and variance σ_z^2. Then, Eq. (15) becomes

$$\begin{aligned} R_s(t_1,t_2) = \frac{\eta_Q U_L}{h\nu B}\int_0^\infty\int_{-\infty}^\infty & A_L(t_1-2z/c)A_L^*(t_2-2z/c)O(\vec{\mathbf{p}},z) \\ & \exp\left[2\pi i(t_1-t_2)(\Delta f - 2\overline{v}_z/\lambda) - 8\pi^2\sigma_z^2/\lambda^2\right]d\vec{\mathbf{p}}dz \end{aligned} \tag{19}$$

For typical lidar experiments, the analysis of Doppler lidar data is restricted to time intervals much smaller than the temporal scale of $v_r(\vec{\mathbf{p}},z)$. In many cases, parameter estimation is performed using data from a single shot and an ensemble average over the random wind $v_r(\vec{\mathbf{p}},z)$ is not appropriate. However, if the sensing volume of the pulse is much larger than the spatial scale of the fluctuations of $v_r(\vec{\mathbf{p}},z)$, the signal covariance has the form of Eq. (19). [See Fig. 6].

A typical Doppler lidar has a narrow beam compared to the dimensions of the sensing volume in the transmit direction z. Then, the function $O(\vec{\mathbf{p}},z)$ behaves like a delta function in Eq. (15) and

$$\begin{aligned} R_s(t_1,t_2) = \frac{\eta_Q U_L}{h\nu B}\int_0^\infty & H(z)A_L(t_1-2z/c)A_L^*(t_2-2z/c) \\ & \exp\left\{2\pi i(t_1-t_2)[\Delta f - 2v_r(0,z)/\lambda]\right\}dz \end{aligned} \tag{20}$$

where the system gain $H(z)[m^{-1}]$ is

$$H(z) = K^2(0,z)\beta(0,z)C(z) \tag{21}$$

and

$$C(z) = \int_{-\infty}^\infty c(\vec{\mathbf{p}},z)d\vec{\mathbf{p}} \tag{22}$$

is the coherent responsivity[22] of the coherent Doppler lidar.

The center of a range gate for Doppler lidar measurements is defined by

$$z_0 = ct_0/2 \tag{23}$$

and the total observation interval corresponding to this range gate is $(t_0 - T/2, t_0 + T/2)$. If $\beta(p,z)$, $K(\vec{\mathbf{p}},z)$, $v_r(\vec{\mathbf{p}},z)$, and $c(\vec{\mathbf{p}},z)$ are constant over the sensing volume of this range gate, we have for all (t_1,t_2) in the observation interval

$$R_s(t_1,t_2) = R_s(\tau) = SNR(z_0)\exp(2\pi i\tau f_m)\int_{-\infty}^{\infty} A_L(t)A_L^*(t-\tau)dt \tag{24}$$

where

$$SNR(z_0) = \frac{\eta_Q c U_L}{2h\nu B} H(z_0) \tag{25}$$

is the SNR for a pulse centered at range z_0, the mean frequency $f_m[Hz]$ of the Doppler lidar signal is defined as

$$f_m = \Delta f - 2v_r(0,z_0)/\lambda \tag{26}$$

$\tau = t_1 - t_2[sec]$, and the limits of integration have been extended to infinity. The signals $z(t)$ and $Z(t)$ are stationary Gaussian processes over the observation interval $(t_0 - T/2, t_0 + T/2)$, i.e., the joint probability density function is only a function of the time difference τ. The signal spectrum for a stationary real signal $Z(t)$ is defined as

$$\Phi_Z(f) = \int_{-\infty}^{\infty} B_Z(\tau)\exp(-2\pi i\tau f)d\tau \tag{27}$$

or

$$\Phi_Z(f) = SNR(z_0)\Omega(f - f_m) \tag{28}$$

where

$$\Omega(f) = |\int_{-\infty}^{\infty} A_L(t)\exp(-2\pi i f t)dt|^2 \tag{29}$$

is the spectrum of the transmitted pulse. For a stationary complex signal $z(t)$, the spectrum is defined the same way as for a real signal with $B_Z(\tau)$ replaced with $R_z(\tau)$ [see Eq. (9)]. The signal spectrum for aerosol targets is also the same as the signal spectrum from a rigid or diffuse hard target.

For a Gaussian pulse with 1/e intensity radius $\sigma[sec]$ and linear frequency chirp $\phi[sec^{-2}]$

$$A_L(t) = \frac{1}{\pi^{1/4}\sigma^{1/2}} \exp\left(-\frac{t^2}{2\sigma^2} + \pi i\phi t^2\right) \tag{30}$$

and

$$R_s(\tau) = SNR(z_0)\exp(2\pi i f_m - \tau^2/{\tau_P}^2) \tag{31}$$

where the correlation time of the lidar signal $\tau_P[sec]$ is given by

$$\frac{1}{{\tau_P}^2} = \frac{1}{{\tau_A}^2} + \frac{1}{{\tau_C}^2} \tag{32}$$

where $\tau_A[sec]$ is the correlation time due to the amplitude profile of the pulse, i.e.,

$$\tau_A = 2\sigma \tag{33}$$

and $\tau_C[sec]$ is the correlation time due to the frequency chirp, i.e.,

$$\tau_C = \frac{1}{\pi\phi\sigma} \tag{34}$$

3. Effects of Wind Shear

Doppler lidar data permits estimation of the radial component of the wind field $v_r(\vec{\rho}, z)$ with a single shot. For short pulse duration, the random fluctuations of $v_r(\vec{\rho}, z)$ can be approximated by the first two terms of it's Taylor series expansion in z about the center of the range gate z_0, i.e.,

$$v_r(\vec{\rho}, z) = v_r(\vec{\rho}, z_0) + g(\vec{\rho}, z_0)(z - z_0) \tag{35}$$

where $g(\vec{\rho}, z_0)[sec^{-1}]$ is the wind shear of the radial component of the velocity at $(\vec{\rho}, z_0)$, i.e.,

$$g(\vec{\rho}, z) = \frac{\partial v_r(\vec{\rho}, z)}{\partial z} \tag{36}$$

The range dependent system gain $O(\vec{\rho}, z)$ is approximated by the first two terms of it's Taylor series expansion in z, i.e.,

$$O(\vec{\rho}, z) = O(\vec{\rho}, z_0)[1 + b(\vec{\rho}, z_0)(z - z_0)] \tag{37}$$

where $b(\vec{\rho}, z)[m^{-1}]$ is the normalized gradient of the system gain, i.e.,

$$b(\vec{\rho}, z) = \frac{1}{O(\vec{\rho}, z)} \frac{\partial O(\vec{\rho}, z)}{\partial z} \tag{38}$$

When these approximations are valid and for a Gaussian pulse defined by Eq. (30)

$$R_s(\mu, \tau) = \frac{\eta_Q c U_L}{2h\nu B} \int_{-\infty}^{\infty} O(\vec{\rho}, z_0)[1 + r_P b(\vec{\rho}, z_0)(\frac{\mu - t_0}{\sigma} - i\frac{\tau}{\tau_1})]$$
$$\exp\left[2\pi i \Delta f \tau - \frac{4\pi i}{\lambda} v_r(\vec{\rho}, z_0)\tau - 2i\frac{(\mu - t_0)}{\sigma}\frac{\tau}{\tau_{WS}} - \frac{\tau^2}{{\tau_T}^2}\right] d\vec{\rho} \tag{39}$$

where $\mu[sec]$ is the centroid of t_1 and t_2,

$$\mu = (t_1 + t_2)/2, \tag{40}$$

$$\tau_{WS} = \frac{\lambda}{2\pi r_P g(\vec{\rho}, z_0)} \tag{41}$$

is the correlation time due to wind shear,

$$r_P = c\sigma/2 \tag{42}$$

is a measure of the range resolution of the pulse,

$$\frac{1}{{\tau_T}^2} = \frac{1}{{\tau_1}^2} + \frac{1}{{\tau_A}^2} \tag{43}$$

$$\frac{1}{\tau_1} = \frac{1}{\tau_C} + \frac{1}{\tau_{WS}} \tag{44}$$

Note that the signal covariance depends on the centroid variable μ and is therefore non-stationary. For a Doppler lidar with a narrow beam compared to the dimensions of the range gate [see Eq. (20)]

$$R_s(\mu,\tau) = SNR(z_0)[1+\gamma(\frac{\mu-t_0}{\sigma} - i\frac{\tau}{\tau_1})]\exp\left[2\pi i f_m\tau - 2i\frac{(\mu-t_0)}{\sigma}\frac{\tau}{\tau_{WS}} - \frac{\tau^2}{{\tau_T}^2}\right] \tag{45}$$

where

$$\gamma = b(0,z_0)r_P = [O(0,z_0+r_P) - O(0,z_0)]/O(0,z_0) \tag{46}$$

is the fractional change of the gain $O(0,z)$ over the range resolution r_P at z_0, if the linear approximation of Eqs. (35) and (37) are valid.

The effects of wind shear become important when the correlation time due to wind shear τ_{WS} is less than the correlation time due to the pulse amplitude profile τ_A, i.e.,

$$\tau_A/\tau_{WS} = 2\pi c\sigma^2 g(0,z_0)/\lambda > 1 \tag{47}$$

$\tau_A/\tau_{WS} = 0.188$ for a wind shear of 0.001 sec^{-1} (10 m/sec per Km), $\lambda = 10\mu m$, and $\sigma = 1\mu sec$.

The effects of wind shear with constant SNR [constant $H(z)$] over the observation interval are shown in Fig. 1. The wind shear produces a rapid decorrelation of the lidar signal, which appears as a damped oscillating signal as the centroid of the observation points μ deviate from the center of the observation interval t_0. This reflects the change in the Doppler shift of the signal from aerosol particles with a different velocity than the instantaneous velocity $v_r(0,z_0)$ at the center of the range gate. The effects of a gradient in the SNR $[H(z)]$ is shown in Fig. 2. The gradient produces an amplitude change in addition to the effects of wind shear.

4. Effects of Wind Turbulence

Atmospheric wind fields are characterized by random fluctuations in space and time. For many cases, the statistics of the wind fields are well characterized by universal functions of basic parameters. For Doppler radar the effects of the random fluctuations of the wind field over the sensing volume has been discussed by Doviak and Zrnic[16]. For Doppler lidar, the situation is complicated because estimates of the velocity are computed for a single shot or a few shots. During the total observation period, the velocity changes little compared to the temporal scale of velocity flucutations. Ensemble averages of the Doppler lidar signal over the atmospehric velocity fluctuations were considered by Churnside and Yura[23]. The effects of spatial variations of the backscatter coefficient over the sensing volume of the pulse were investigated by Rye[24] using simulations.

The covariance of the Doppler lidar signal for a single shot is given by Eq. (15), which can be written as

$$R_s(t_1,t_2) = \frac{\eta_Q U_L}{h\nu B}\int_0^\infty\int_{-\infty}^\infty A_L(t_1-2z/c)A_L^*(t_2-2z/c)O(\vec{\mathrm{p}},z) \exp\left[2\pi i f_m\tau - \frac{4\pi i}{\lambda}\Delta v_r(\vec{\mathrm{p}},z)\tau\right] d\vec{\mathrm{p}}dz \tag{48}$$

where

$$\Delta v_r(\vec{\mathbf{p}}, z, z_0) \;=\; v_r(\vec{\mathbf{p}}, z) - v_r(0, z_0) \tag{49}$$

is the difference of the radial component of the velocity compared to $v_r(0, z_0)$.

The mean frequency f_m is a random variable because the wind field is random. The estimation error for estimates of the mean frequency f_m using data from a single shot is difficult to predict because the signal statistics depend on the random functions $\Delta v_r(\vec{\mathbf{p}}, z, z_0)$ and $O(\vec{\mathbf{p}}, z)$. It may be possible to estimate the random functions $\Delta v_r(\vec{\mathbf{p}}, z, z_0)$ and $O(\vec{\mathbf{p}}, z)$ as well as the other signal parameters if many shots of data can be collected during the temporal scale of these fluctuations. If this approach is not possible, then an ensemble average over the random functions $\Delta v_r(\vec{\mathbf{p}}, z, z_0)$ and $O(\vec{\mathbf{p}}, z)$ is required to develop and analyze estimation algorithms for the signal parameters[17].

For well behaved atmospheric conditions, the velocity difference $\Delta v_r(\vec{\mathbf{p}}, z, z_0)$ is approximately a zero mean Gaussian random variable. Performing the ensemble average over this random variable [$< \exp(i\xi) = \exp(- < \xi^2 > /2)$ for a zero-mean Gaussian random variable ξ] produces

$$R_s(t_1, t_2) = \frac{\eta_Q U_L}{h\nu B} \int_0^\infty \int_{-\infty}^\infty A_L(t_1 - 2z/c) A_L^*(t_2 - 2z/c) O(\vec{\mathbf{p}}, z) \exp\left[2\pi i \tau f_m - \frac{8\pi^2\tau^2}{\lambda^2} D_r(\vec{\mathbf{p}}, z, z_0)\right] d\vec{\mathbf{p}} dz \tag{50}$$

where

$$D_r(\vec{\mathbf{p}}, z, z_0) \;=\; \langle \Delta v_r(\vec{\mathbf{p}}, z, z_0)^2 \rangle \tag{51}$$

is the structure function of the fluctuations of the radial component of the velocity field. Note that the signal covariance depends on the centroid variable μ and is therefore non-stationary.

For a narrow beam such that the function $O(\vec{\mathbf{p}}, z)$ dominates the $\vec{\mathbf{p}}$ integration

$$R_s(t_1, t_2) = \frac{\eta_Q U_L}{h\nu B} \int_0^\infty A_L(t_1 - 2z/c) A_L^*(t_2 - 2z/c) H(z) \exp\left[2\pi i \tau f_m - \frac{8\pi^2\tau^2}{\lambda^2} D_r(0, z, z_0)\right] dz \tag{52}$$

For a narrow beam and a short pulse such that $H(z)$ is constant over the sensing range of the pulse,

$$R_s(t_1, t_2) = SNR(z_0) \int_0^\infty A_L(t_1 - 2z/c) A_L^*(t_2 - 2z/c) \exp\left[2\pi i \tau f_m - \frac{8\pi^2\tau^2}{\lambda^2} D_r(0, z, z_0)\right] dz \tag{53}$$

When the statistics of the velocity fields over the sensing volume of the pulse are locally stationary and isotropic[25]

$$D_r(\vec{\mathbf{p}}, z, z_0) \;=\; C_v \epsilon^{2/3}(z_0) r^{2/3} [(z - z_0)^2 + 4p^2/3]/r^2 \tag{54}$$

where $C_v \approx 2$ is the Kolmogorov constant, $\epsilon[m^2 s^{-3}]$ is the energy dissipation rate, and $r^2 = (z - z_0)^2 + p^2$. For a Gaussian transmitted pulse with linear frequency chirp [Eq. (30)]

$$R_s(\mu,\tau) = \frac{\eta_Q U_L c {r_P}^2}{2\pi^{1/2} h\nu B} \exp(2\pi i \tau f_m - \tau^2/{\tau_A}^2) \int_{-\infty}^{\infty}\int_{-\infty}^{\infty} O(r_P\vec{\mathbf{q}}, r_P\zeta + z_0)$$
$$\exp\left\{-[(\mu - t_0)/\sigma - \zeta]^2 + 2\pi i\phi\sigma[(\mu - t_0)/\sigma - \zeta]\tau - \kappa^{-4/3}(\zeta^2 + 4q^2/3)\tau^2/{\tau_E}^2\right\} d\vec{\mathbf{q}} d\zeta \qquad (55)$$

where $\kappa^2 = \zeta^2 + q^2$, $r_P\zeta = z - z_0$, $r_P\vec{\mathbf{q}} = \vec{\mathbf{p}}$, and the correlation time due to turbulence $\tau_E[sec]$ is given by

$$\frac{1}{{\tau_E}^2} = 8\pi^2 C_v(\epsilon r_P)^{2/3}/\lambda^2 = 8\pi^2 D_r(0, z_0 + r_P, z_0)/\lambda^2 \qquad (56)$$

For a coherent Doppler lidar with a Gaussian transmitted spatial profile[22]

$$O(r_P\vec{\mathbf{q}}, z) = \frac{C(z)}{\pi\sigma_B^2(z)} \exp[-{r_P}^2 q^2/\sigma_B^2(z)] \qquad (57)$$

where $\sigma_B(z)$ is the 1/e intensity radius of the transmitted beam at range z.

For a narrow beam, the integration over $\vec{\mathbf{q}}$ can be performed and

$$R_s(\mu,\tau) = \frac{\eta_Q U_L c {r_P}^2}{2\pi^{1/2} h\nu B} \exp\left(2\pi i \tau f_m - \frac{\tau^2}{{\tau_A}^2}\right)$$
$$\int_{-\infty}^{\infty} C(r_P\zeta + z_0) \exp\left\{-[(\mu - t_0)/\sigma - \zeta]^2 + 2\pi i\phi\sigma[(\mu - t_0)/\sigma - \zeta]\tau - \zeta^{2/3}\tau^2/{\tau_E}^2\right\} d\zeta \qquad (58)$$

For a short pulse such that $C(r_P\zeta + z_0)$ is constant over the ζ integration,

$$R_s(\mu,\tau) = \frac{SNR(z_0)}{\pi^{1/2}} \exp\left(2\pi i \tau f_m - \frac{\tau^2}{{\tau_A}^2}\right)$$
$$\int_{-\infty}^{\infty} \exp\left\{-[(\mu - t_0)/\sigma - \zeta]^2 + 2\pi i\phi\sigma[(\mu - t_0)/\sigma - \zeta]\tau - \zeta^{2/3}\tau^2/{\tau_E}^2\right\} d\zeta \qquad (59)$$

The effects of wind turbulence become important when the correlation time due to turbulence τ_E becomes less than the correlation time due to the pulse amplitude profile τ_A, i.e., when

$$\tau_A/\tau_E = 4\pi C_v^{1/2}\sigma(\epsilon r_P)^{1/3}/\lambda > 1 \qquad (60)$$

For typical stable boundary layer turbulence, $\epsilon = 0.01 m^2/sec^3$. Then $\tau_A/\tau_E = 2.88$ for $\lambda = 10\mu m$, and $\sigma = 1\mu sec$.

The effects of wind turbulence and the finite transverse dimensions of the beam are shown in Fig. 3. The decrease in the correlation scale due to turbulence is more pronounced for a wide beam ($\sigma_B > r_P$) because of the increase in the Doppler shifts from the random fluctuations of the wind in the transverse dimensions.

The effects of wind turbulence for the common case of a narrow transmitted beam compared to the range resolution ($\sigma_B < r_P$) is shown if Fig. 4. When $\tau_E < \tau_A$, the signal covariance is reduced due to the wind turbulence.

For typical surface layer measurements, the statistical description of the velocity fluctuations must include the spatial scale of the turbulent wind field (sometimes called the outer-scale of turbulence) that is proportional to $z_H[m]$, the height above the surface. The spectra of velocity fluctuations satisfy universal scaling functions. For a horizontal propagation direction along the mean velocity, the universal spectrum of velocity flucutations in the direction of the mean velocity results in a universal, locally stationary, structure function of velocity fluctuations. For neutral stability[26]

$$D_r(0, z_0 + r, z_0) = 2\sigma_r^2 \Lambda(r/z_H) \tag{61}$$

where $\sigma_r[m/sec]$ is the standard deviation of the radial component of the velocity flucutations and the universal function

$$\Lambda(x) = (\alpha x)^{2/3}[1 + (\alpha x)^{\rho}]^{-2/(3\rho)} \tag{62}$$

where $\alpha = 0.26278$ and $\rho = 1.1948$. The function $\Lambda(x)$ is shown in Fig. 5. For small r, Eq. (61) is equal to Eq. (54) with $\vec{\rho} = 0$ and

$$\epsilon = (2\sigma_r^2/C_v)^{3/2}\alpha/z_H \tag{63}$$

Substituting Eqs. (30) and (61) into Eq. (53) produces

$$R_s(\mu, \tau) = \frac{SNR(z_0)}{\pi^{1/2}} \exp\left(2\pi i \tau f_m - \frac{\tau^2}{{\tau_A}^2}\right)$$
$$\int_{-\infty}^{\infty} \exp\left\{-[(\mu - t_0)/\sigma - \zeta]^2 + 2\pi i \phi\sigma[(\mu - t_0)/\sigma - \zeta]\tau - \Lambda(r_P\zeta/z_H)\tau^2/{\tau_H}^2\right\} d\zeta \tag{64}$$

where

$$\frac{1}{{\tau_H}^2} = 16\pi^2\sigma_r^2/\lambda^2 \tag{65}$$

There are two limiting cases of Eq. (64). When the sensing volume of the pulse r_P is less than the outer scale of turbulence ($L_0 \approx z_H$) the integration in Eq. (64) is dominated by the power law region of $\Lambda(x)$ and Eq. (64) is equal to Eq. (59). When r_P is much larger than z_H, then $\Lambda(r_P\zeta/z_H) \approx 1$ and a result similar to Eq. (19) is produced. If the mean frequency f_m is defined using the average radial velocity $\overline{v}_z$ instead of the instantaneous radial velocity $v_r(\mathbf{0}, z_0)$, then Eq. (19) is produced when $r_P >> z_H$ because $D_r(\vec{\rho}, z, z_0) \rightarrow \sigma_r^2$ instead of $2\sigma_r^2$ [see Eq. (61)].

The signal covariance Eq. (64) is shown in Fig. 6 for a typical nightime condition with a horizontal path at height $z_H = 2m$, a velocity fluctuation $\sigma_r = 0.5m/sec$ and operating wavelengths of $2\mu m$ and $10\mu m$. This corresponds to an energy dissipation rate of $\epsilon = 0.0164m^2/s^3$. For these parameters, the correlation scale for turbulence τ_H assuming $r_P >> z_H$ is $1.59\mu sec$ for the $10\mu m$ lidar and $0.318\mu sec$ for the $2\mu m$ lidar. For this regime, the signal covariance is determined by the transmitted pulse when $\tau_A < \tau_H$.

5. Summary

The signal covariance for coherent Doppler lidar data is derived for general conditions for both real and complex data. The covariance is defined with respect to a given ensemble average. The most general case is the ensemble average over the random phases of the backscattered fields from the aerosol particles [Eq. (12)]. The covariance parameters are a function of the instantaneous wind field and atmospheric conditions. In this case, the covariance can be estimated with multiple shots over a time interval that is less than the temporal scale of the fluctuations in the atmosphere. The next level of ensemble average is over the atmospheric refractive turbulence [see Eq. (15)]. In many cases, the effects of refractive turbulence are negligible and Eq. (18) is valid. Under the ideal limit of uniform velocity, atmospheric parameters, and system parameters over the sensing volume of the pulse, the Doppler lidar signal is stationary and determined by the transmitted pulse Eqs. (24), (28), and (29). When there is a linear wind shear and linear system gain over the sensing volume of the pulse, the signal covariance is non-stationary (depends on μ) and given by Eq. (39) and for a narrow lidar beam by Eq. (45). The signal parameters are expressed in terms of the instantaneous atmospheric variables and lidar system parameters. The mean frequency f_m is defined in terms of the instantaneous radial velocity in the center of the range gate of interest for a single shot. This permits analysis and development of more efficient estimation algorithms which are valid when the pulse sensing volume is small compared to the variations of the instantaneous atmospheric variables. The coherent lidar signal is not stationary over the observation interval and spectral domain estimators will be less efficient for this case because they assume stationary data. When the atmospheric parameters are unable to be modeled over the observation interval (e.g., velocity fluctuations are not a linear function of space over the sensing volume of the pulse), the analysis and development of estimation algorithms requires the ensemble average over the unknown parameters[18]. The signal covariance for this case with general statistics for the velocity fluctuations is given by Eqs. (50), (52), and (53). For isotropic and homogeneous wind fluctuations described by the Kolmogorov turbulence spectrum over the sensing volume of the pulse, the signal covariance is given by Eqs. (50), (52), and (53) with Eq. (54). and for a Gaussian pulse defined by Eq. (30), the correlation scale is given by τ_E Eq. (56). When the sensing volume of the pulse is much larger than L_0, then Eqs. (50), (52), and (53) are valid with $D_r(\vec{\rho}, z, z_0) = 2\sigma_r^2$ is valid and the correlation time is given by τ_H Eq. (65). For intermediate regimes, the universal description of the velocity structure function is required [see Eq. (61)] For the case of horizontal propagation in the atmospheric surface layer and typical nightime conditions, the correlation time due to the effects of turbulence are less than $2\mu sec$ for a $10\mu m$ lidar and less than $0.2\mu sec$ for a 2 micron lidar. The correlation time will be reduced even more for typical daytime unstable convective conditions. For wind shear and wind turbulence, the correlation time is proportional to the operating wavelength λ [see Eqs. (41), (56), (65)] and the critical pulse length where the effects of the wind fluctuations dominate over the contribution of the pulse is also proportional to λ.

ACKNOWLEDGMENTS

The author acknowledges useful discussions with M. J. Kavaya and B. J. Rye. This work was supported by the National Science Foundation and the National Aeronautics and Space Administration Marshall Space Flight Center under Research Grant NAG8-253 (Michael J. Kavaya, Technical Officer).

Appendix A: Coherent Doppler Lidar Signals

The total coherent or heterodyne Doppler lidar signal $i_T(t)[A]$ is the sum of the Doppler IF signal current $i_S(t)[A]$ and the detector noise current $i_N(t)[A]$ which is conveniently written in complex notation as $i_T(t) = Re[y(t)]$, $i_N(t) = Re[u(t)]$, where

$$y(t) = u(t) + \frac{2G_D e}{h\nu}\int_D \eta_Q(\vec{\mathbf{w}})E_S(\vec{\mathbf{w}}, L, t)E^*_{LO}(\vec{\mathbf{w}}, L)\exp(2\pi i\Delta f t + i\theta_S)d\vec{\mathbf{w}} \tag{A1}$$

G_D is the dimensionless amplifier gain, $e = 1.602 \text{ x } 10^{-19}[C/electron]$ is the electronic charge, $\eta_Q(\vec{\mathbf{w}})[electrons/photon]$ is the detector quantum efficiency function on the detector surface, $E_S(\vec{\mathbf{w}}, L, t)$ is the backscattered field on the detector surface, $E_{LO}(\vec{\mathbf{w}}, L)$ is the LO field on the detector surface, $\theta_S[rad]$ is the random phase of the backscattered field compared to the LO field, $\Delta f[Hz]$, is the frequency difference between the transmitted and LO field, $\vec{\mathbf{w}}[m]$ is the transverse coordinate on the detector surface and $d\vec{\mathbf{w}}$ denotes two-dimensional integration over the detector surface. For ideal optical systems and for a infinite uniform detector, the fields on the detector can be represented in terms of the fields in the plane of the receiver optics, i.e.,

$$y(t) = u(t) + \int_{-\infty}^{\infty} E_S(\vec{\mathbf{v}}, 0, t)E^*_{LO}(\vec{\mathbf{v}}, 0)W_R(\vec{\mathbf{v}})\exp(2\pi i\Delta f t + i\theta_S)d\vec{\mathbf{v}} \tag{A2}$$

where $E_S(\vec{\mathbf{v}}, 0, t)$ and $E_{LO}(\vec{\mathbf{v}}, 0)$ are the backscattered field and LO field in the receiver plane.

If the signal noise is dominated by the shot noise generated by the local oscillator field (quantum limited detection), the average noise power is

$$i_N^2(t) = \frac{1}{2}u(t)u^*(t) = 2G_D{}^2e^2B\eta_Q P_{LO}/(h\nu) \tag{A3}$$

where $B[Hz]$ is the noise bandwidth. It is convenient to normalize the signals by the rms of the noise current, i.e.,

$$z(t) = y(t)/i_N^2(t)^{1/2} = s(t) + n(t). \tag{A4}$$

The backscattered field from a point scatterer at coordinate $(\vec{\mathbf{p}}, z)$ with scattering cross section σ_S is

$$E_S(\vec{\mathbf{v}}, 0, t) = \lambda\sigma_S^{1/2}K(\vec{\mathbf{p}}, z)\int_{-\infty}^{\infty} E_L(\vec{\mathbf{u}}, 0, t - 2z/c)W_T(\vec{\mathbf{u}})G(\vec{\mathbf{p}}; \vec{\mathbf{u}}, z)$$
$$G(\vec{\mathbf{p}}; \vec{\mathbf{v}}, z)\exp[i\theta(\vec{\mathbf{p}}, z) - 4\pi i t v_r(\vec{\mathbf{p}}, z)/\lambda]d\vec{\mathbf{u}} \tag{A5}$$

where $\theta(\vec{\mathbf{p}}, z)$ is the random phase of the backscattered field. The total backscattered field is the sum of all the backscattered fields from the aerosol particles illuminated by

the transmitted field. Substituting the total backscattered field into Eqs. (A2), (A4), (9), (1), (4), performing the ensemble average over the random phases $\theta(\vec{\rho}, z)$ using the identity $\exp[i(\theta(\vec{\rho}, z_1) + \theta(\vec{\rho}, z_2)] = 0$, and converting the summation over aerosol particles to integration[22] produces Eq. (12). The same procedure produces Eq. (8).

References

1. J. W. Bilbro, C. DiMarzio, D. Fitzjarrald, S. Johnson, and W. Jones, "Airborne Doppler lidar measurements," Appl. Opt. **25,** 2952-2960 (1986).
2. J. C. Petheram, G. Frohbeiter, and A. Rosenberg, "Carbon dioxide doppler lidar wind sensor on a space station polar platform," Appl. Opt. **28,** 834-839 (1989).
3. M. J. Post and R. E. Cupp, "Optimizing a pulsed doppler lidar," Appl. Opt. **29,** 4145-4158 (1990).
4. G. N. Pearson and B. J. Rye, "Frequency fidelity of a compact CO_2 Doppler lidar transmitter," Appl. Opt. **31,** 6475-6484 (1992).
5. M. J. Kavaya, S. W. Henderson, J. R. Magee, C. P. Hale, and R. M. Huffaker, "Remote wind profiling with a solid-state nd:yag coherent lidar system," Opt. Let. **14,** 776-778 (1992).
6. S. W. Henderson, C. P. Hale, J. R. Magee, M. J. Kavaya, and A. V. Huffaker, "Eye-safe coherent laser radar system at 2.1 μm using Tm,Ho:YAG lasers," Opt. Lett. **16,** 773-775 (1991).
7. S. W. Henderson, P. J. M. Suni, C. P. Hale, S. M. Hannon, J. R. Magee, D. L. Bruns, and E. H. Yuen, "Coherent laser radar at 2 μm using solid-state lasers," IEEE Trans. Geo. Remote Sensing **31,** 4-15 (1993).
8. B. J. Rye, and R. M. Hardesty, "Discrete spectral peak estimation in incoherent backscatter heterodyne lidar. I. Spectral accumulation and the Cramer-Rao lower bound," IIEEE Trans. Geo. Sci. Remote Sensing **31,** 16-27 (1993).
9. R. G. Frehlich, and M. J. Yadlowsky, "Performance of mean frequency estimators for Doppler Radar/Lidar," submitted to J. Atm. Ocean. Tech., (1993).
10. R. M. Hardesty, "Performance of a discrete spectral peak frequency estimator for Doppler wind velocity measurements," IEEE Trans. Geosci. Remote Sensing **GE-24,** 777-783 (1986).
11. P. R. Mahapatra and D. S. Zrnic, "Practical algorithms for mean velocity estimation in pulse Doppler weather radars using a small number of samples," IEEE Trans. Geosci. Electronics **GE-21,** 491-501 (1983).
12. P. T. May and R. G. Strauch, "An examination of Wind Profiler signal processing algorithms," Atmos. Oceanic Tech. **6,** 731-735 (1989).
13. P. T. May, T. Sato, M. Yamamoto, S. Kato, T. Tsuda, and S. Fukao, "Errors in the determination of wind speed by Doppler radar," Atmos. Oceanic Tech. **6,** 235-242 (1989).
14. B. J. Rye and R. M. Hardesty, "Discrete spectral peak estimation in incoherent backscatter heterodyne lidar. II. Correlogram accumulation," IEEE Trans. Geo. Sci. Remote Sensing **31,** 28-35 (1993).
15. D. S. Zrnic, "Estimation of spectral moments of weather echoes," IEEE Trans. Geosci. Electronics **GE-17,** (1979).
16. Doviak, R. J., and D. S. Zrnic, 1984: second edition 1993: *Doppler radar and weather observations*, Academic Press
17. Van Trees, H. L., 1968: *Detection, Estimation, and Modulation Theory, Part I*, John Wiley and Sons, Inc.
18. Helstrom, C. W., 1968: *Statistical theory of signal detection*, Pergamon Press.
19. B. Gold, A. V. Oppenheim, and C. M. Rader, "Theory and implementation of the discrete hilbert transformation," Symposium on Computer Processing in Communications,

April 8-10, (1969), Brooklyn, New York.
20. V. Cizek, "Discrete Hilbert Transform," IEEE Trans. Audio. and Electroacoust. **AU-18,** 340-343 (1970).
21. R. G. Frehlich, "Cramer-Rao Bound for Gaussian random processes and applications to radar processing of atmospheric signals," IEEE Trans. Geo. Sci. Remote Sensing (in press), (1993).
22. R. G. Frehlich and M. J. Kavaya, "Coherent laser radar performance for general atmospheric refractive turbulence," Appl. Opt. 30, 5325-5352 (1991).
23. J. H. Churnside and H.T. Yura, "Speckle statistics of atmospherically backscattered laser light," Appl. Opt. **22,** 2559-2565 (1983).
24. Barry J. Rye, "Spectral correlation of atmospheric lidar returns with range-dependent backscatter," J. Opt. Soc. Am. A. **7,** 2199-2207 (1990).
25. Monin, A. S., and A. M. Yaglom, *Statistical Fluid Mechanics: Mechanics of Turbulence,* Volume 2, MIT Press (1975)
26. J. C. Kaimal, J. C. Wyngaard, Y. Izumi, and O. R. Cote, "Spectral characteristics of surface-layer turbulence," Quart. J. R. Met. Soc. **98,** 563-589 (1972).

Figure 1

Fig. 1. Effects of wind shear on the normalized signal covariance [Eqs. (9), (30), (45), $\gamma = f_m = \phi=0$] as a function of τ/τ_A with constant SNR over the observation interval and (___) $\mu = t_0$, no wind shear, (....) $\mu - t_0 = \sigma$ and $\tau_A = \tau_{WS}$; (- - -) $\mu - t_0 = 2\sigma$ and $\tau_A = \tau_{WS}$; (- . - .) $\mu - t_0 = \sigma$ and $\tau_A = 2\tau_{WS}$; and (..- .. -) $\mu - t_0 = 2\sigma$ and $\tau_A = 2\tau_{WS}$.

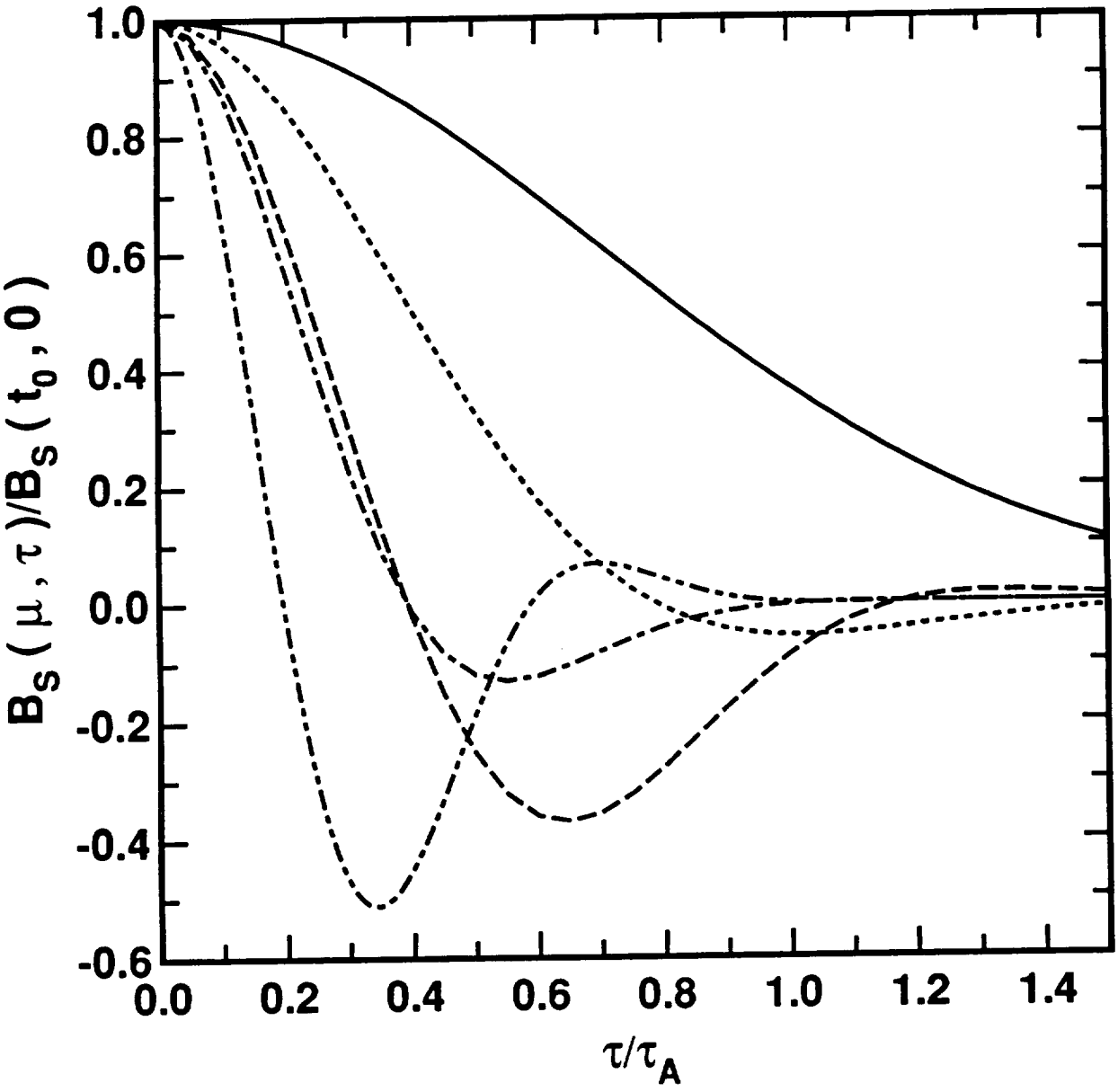

Figure 2

Fig. 2. Effects of wind shear and gradients in SNR over the observation interval on the normalized signal covariance [Eqs. (9), (30), (45), $f_m = \phi$=0] as a function of τ/τ_A compared with constant SNR over the observation interval and no wind shear (___). The curves represent (....) $\mu - t_0 = \sigma$, $\tau_A = \tau_{WS}$, and $\gamma = 0.2$; (- - -) $\mu - t_0 = \sigma$, $\tau_A = \tau_{WS}$, and $\gamma = 0.4$; (- . - .) $\mu - t_0 = 2\sigma$, $\tau_A = 2\tau_{WS}$, and $\gamma = 0$; (.. - .. -) $\mu - t_0 = 2\sigma$, $\tau_A = 2\tau_{WS}$, and $\gamma = 0.2$; and (..- - ..- -) $\mu - t_0 = 2\sigma$, $\tau_A = 2\tau_{WS}$, and $\gamma = 0.4$.

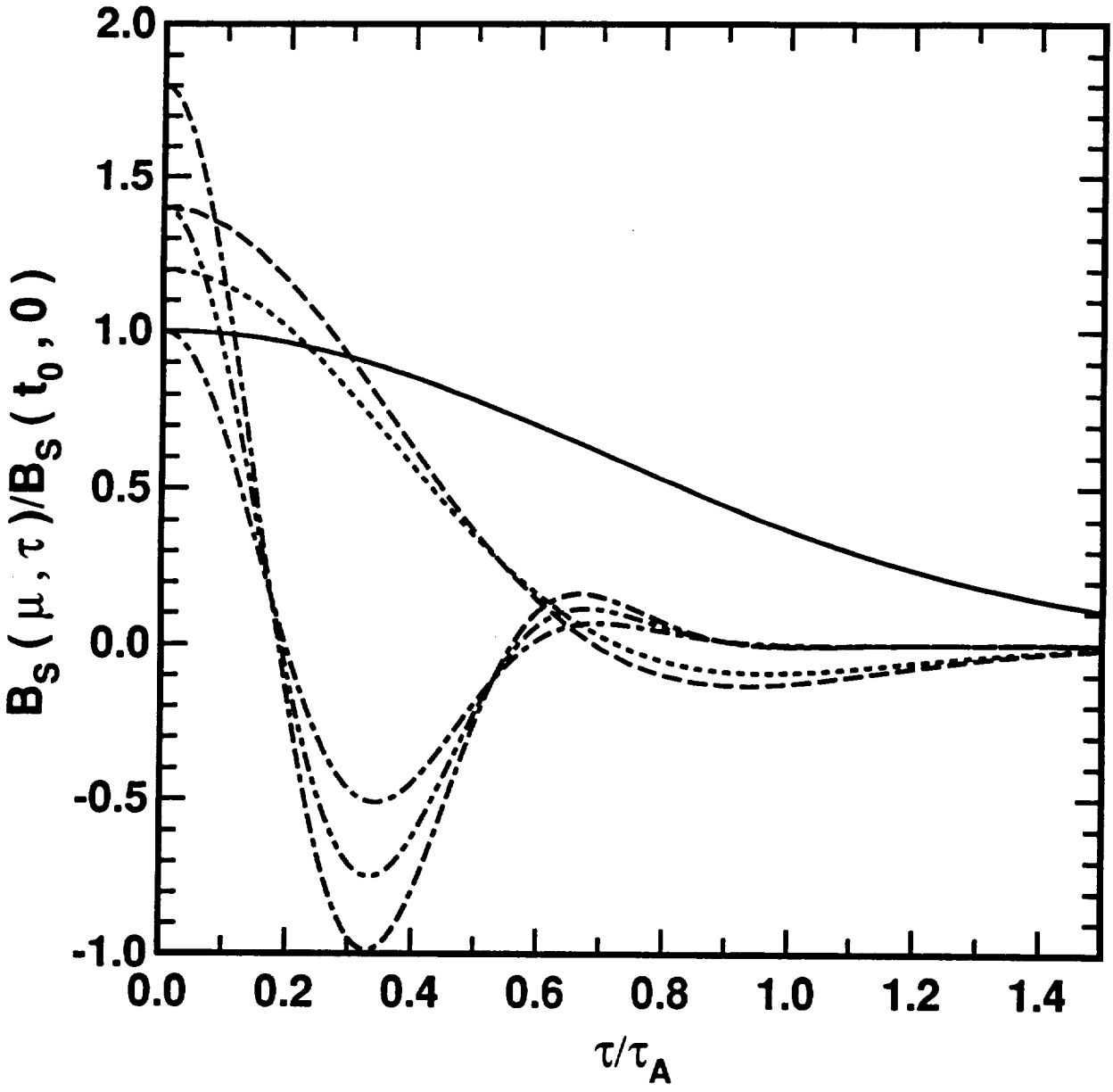

Fig. 3. Effects of the finite transverse dimensions of a lidar beam and wind turbulence on the normalized signal covariance [Eqs. (9), (30), (55), $f_m = \phi = 0$] as a function of τ/τ_A with constant SNR over the observation interval and case a) $\mu = t_0$ with (__) no wind turbulence; (...) $\tau_E = \tau_A/2$, and $\sigma_B << \tau_P$; (- -) $\tau_E = \tau_A/2$, and $\sigma_B = \tau_P/2$; (. - - -) $\tau_E = \tau_A/2$, and $\sigma_B = \tau_P$; (- - . - - -) $\tau_E = \tau_A/2$, and $\sigma_B = 2\tau_P$; and case b) the same as case a) but with $\mu - t_0 = \sigma$.

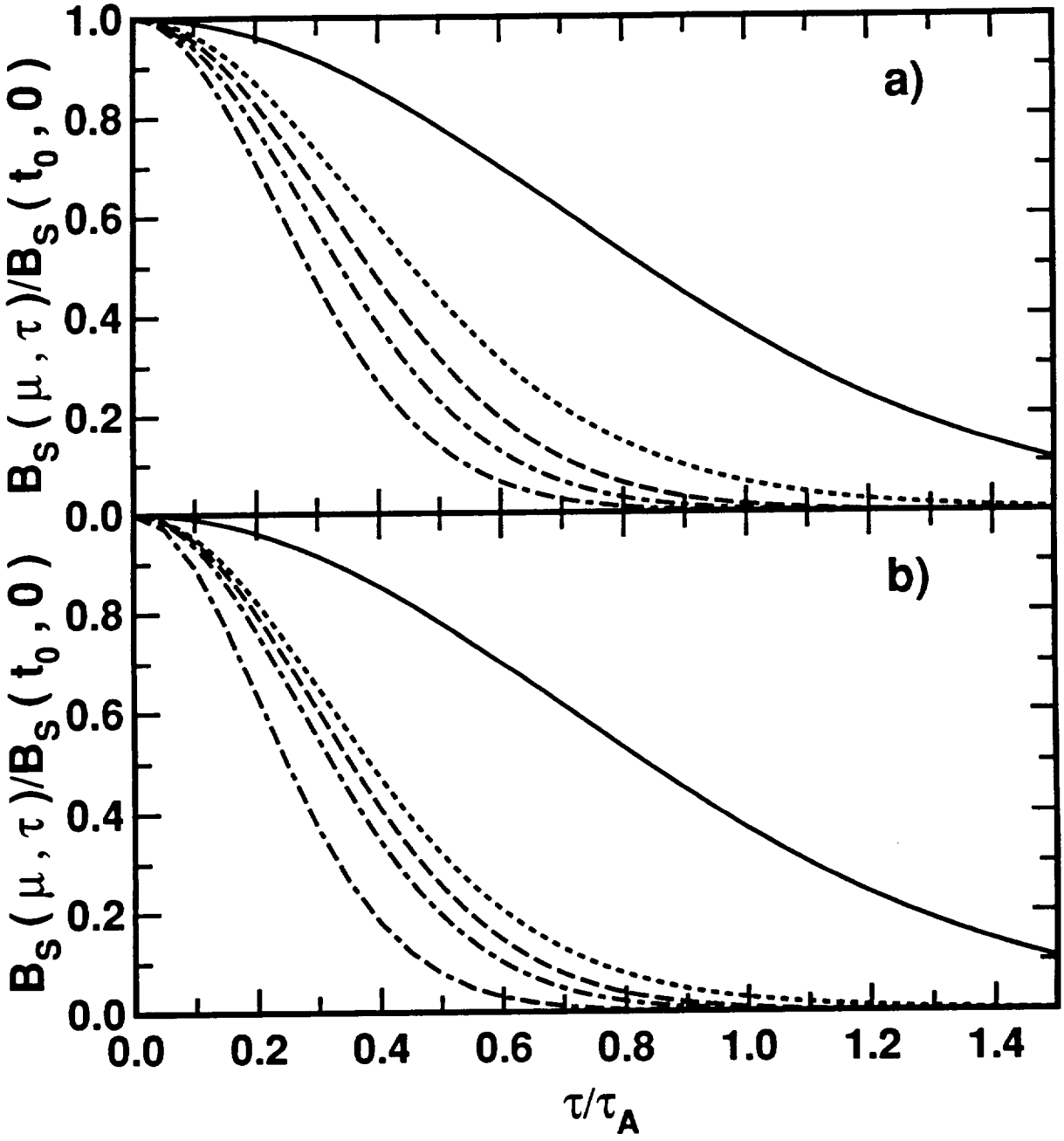

Figure 4

Fig. 4. Effects of wind turbulence on the normalized signal covariance [Eqs. (9), (30), (59),$f_m = \phi$=0] as a function of τ/τ_A with constant SNR over the observation interval and narrow transmitted beam compared to the range resolution ($\sigma_B << \tau_P$) for case a) $\mu = t_0$ with (—) no wind turbulence; (...) $\tau_E = \tau_A/2$; (- -) $\tau_E = \tau_A$; and case b) is the same as case a) but with $\mu - t_0 = \sigma$.

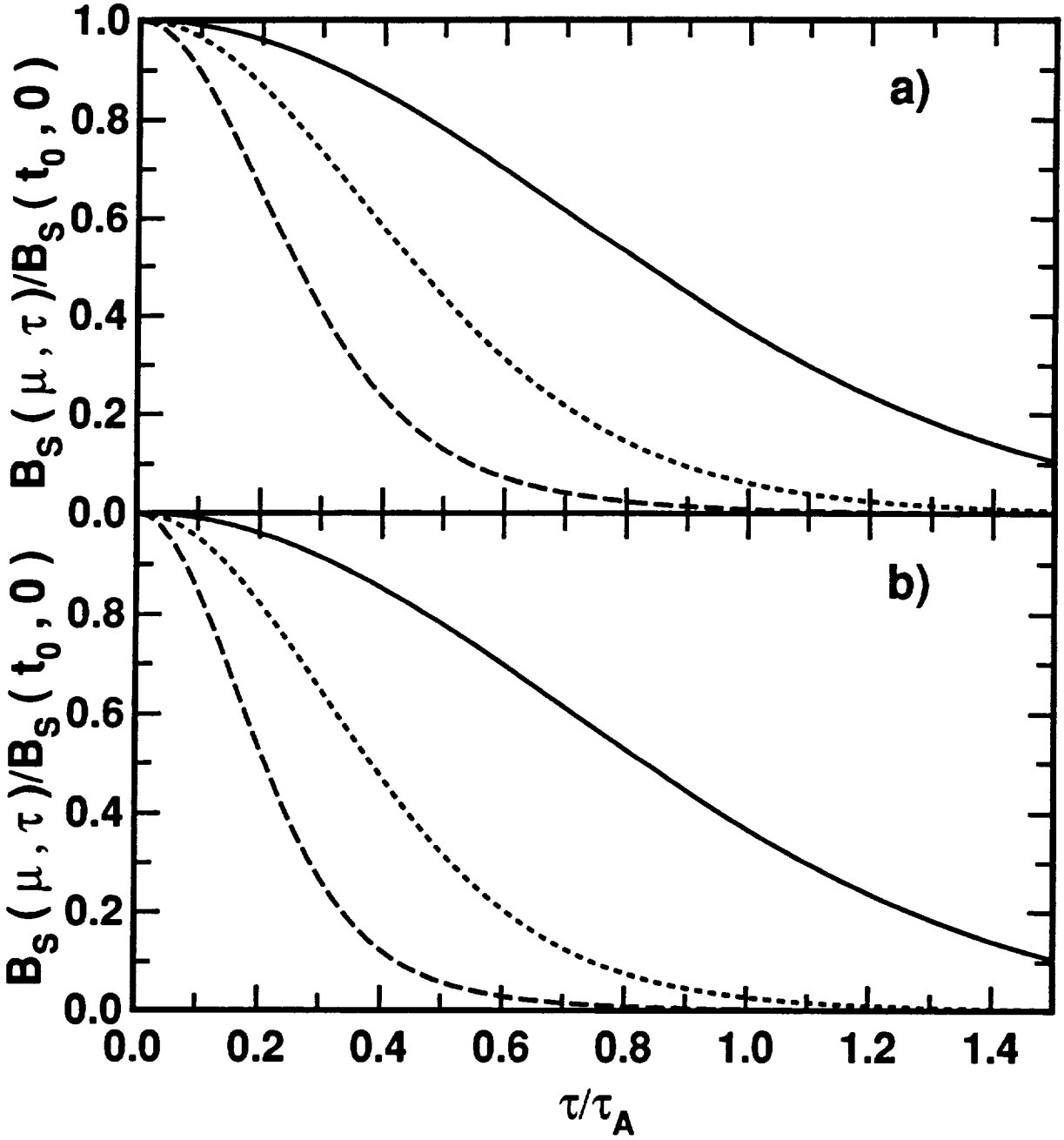

Figure 5

Fig. 5. Normalized structure function of velocity fluctuations in the direction of the mean velocity $\Lambda(x)$ vs x for neutral stability in the atmospheric surface layer.

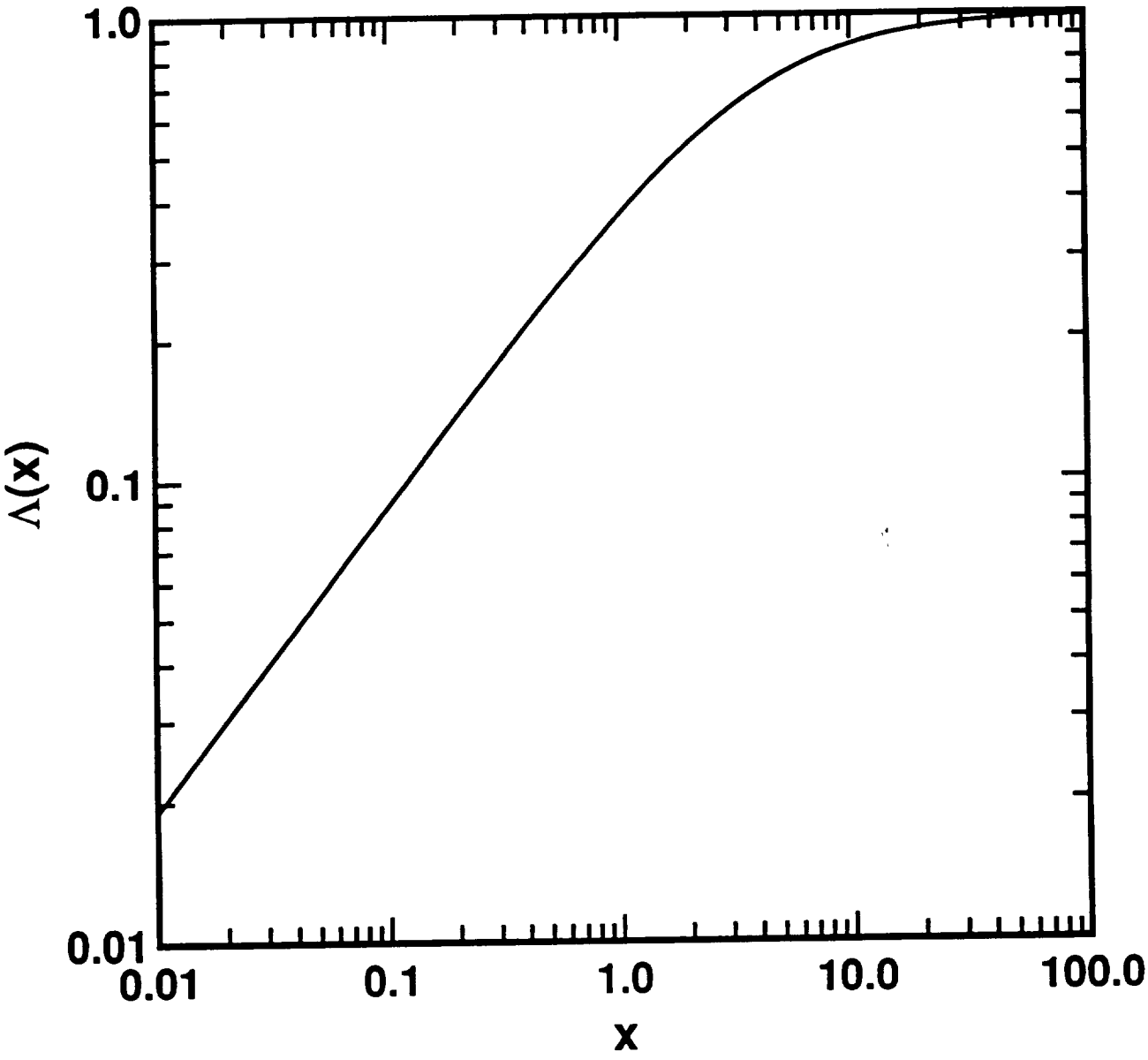

Figure 6

Fig. 6. Normalized signal covariance [Eqs. (9), (30), (64), $f_m = \phi = 0$] as a function of τ for $\mu = t_0$ and a $10\mu m$ and $2\mu m$ lidar for a horizontal propagation path at a height $z_H = 2m$ in the atmospheric surface layer under neutral stability with a standard deviation of the radial component of velocity fluctuations $\sigma_r = 0.5m/sec$. The correlation scale assuming the lidar pulse dominates the signal statistics $\tau_A = 2\sigma$ is (—) $0.2\mu sec$, (...) $0.4\mu sec$, (- -) $1.0\mu sec$, (. - . -) $2.0\mu sec$, (- .. - ..) $4.0\mu sec$, and (- - . - - .) $10.0\mu sec$.